Decentralized and Reconfiguration Control for Large Scale Systems with Application to a Segmented Telescope Test-Bed

by

Principal Investigator: Dr. Petros Ioannou

Ph.D. Students:

Kun Li
Ali Abdullah
Rama Rhagavendra
Barış Fidan

Department of Electrical Engineering–Systems
University of Southern California
Los Angeles, California 90089-2564

Tel:(213)740-4452
ioannou@usc.edu
http://www-rcf.usc.edu/∼ioannou

Final Report to California State University, Los Angeles, for Award No. UAS/USC-220438.

March 2003

Disclaimer

Acknowledgements

We would like to thank Professor H. Boussalis and Professor M. Mirmirani of California State University, Los Angeles (*CSULA*) for their support of this research. In addition we would like to thank Professor K. Rad, Mr. Demetrios Florakis, Mr. Salvador Fallorina, Mr. Mike Lara and the rest of the group from *CSULA* for their help in maintaining the test-bed and assisting with experiments.

Abstract

Large scale systems have posed a great challenge to both modelling and control since the high dimensionality often causes complexities in modelling, control design and implementation. In this report we consider a class of large scale systems motivated from the large segmented telescope test-bed located at the SPACE lab of California State University, Los Angeles.

We develop a wide class of decentralized control schemes to meet the performance requirements as well as decentralized failure detection, isolation and reconfigurable control schemes to deal with possible sensor failures. Different control design techniques that include H_∞, linear quadratic, static output feedback, and direct adaptive control are used as part of the decentralized schemes. The objective is to meet the performance requirements with the least computationally complex control scheme in the presence of possible disturbances and sensor failures.

The algorithms are developed and analyzed for a general class of large scale systems. Their properties are demonstrated in real time using the segmented telescope structure located at the SPACE lab of California State University, Los Angeles.

Contents

List Of Tables

List Of Figures

Chapter 1

Introduction

A system is called "large scale" either because its dimension is so large that conventional techniques of modelling, analysis, control, design and computation fail to give a reasonable solution with reasonable computational efforts or if it can be decoupled or partitioned into a number of interconnected subsystems [28]. There are many examples of large scale systems that present a great challenge to both modelling and control. Among those, large flexible space structure(LFSS) is the one that will be addressed here.

Large flexible space structures are typical large scale systems due to the large size, low rigidity and low damping that often result in their mathematical models of high dimensionality. Segmented telescope is just one among them. The accurate control of the segments of large segmented telescopes to achieve the desired shape could open the way for the construction of much larger telescopes with much better capabilities. The approaches considered for the control of LFSS have generally been directed towards "centralized control". Model reduction [29, 22], modal control [38, 3], output feedback control [4, 30], adaptive control [20, 39], frequency-weighted Linear Quadratic Gaussian(LQG) [19], Independent Modal Space Control(IMSC) [37], positivity combined with multivariable characteristic frequency loci [27, 10], modified linear quadratic regulator(LQR) control [9], H_∞ robust control [41] are some of the techniques used to deal with the centralized control problem of LFSS.

However, the high-order LFSS model often results in a high-order controller. In real-time implementation, the order of the controller is limited by the hardware and computational complexity. In such case a decentralized control approach may be more appropriate. The motivation for obtaining a decentralized controller is simplicity of implementation which makes parallel computation feasible. In order for the decentralized control to achieve as good performance as that of the centralized control, the interconnections between subsystems have to be weak. Unfortunately, the dynamics of the mirror segments of the telescope, defined as local subsystems, are strongly interconnected due to the structure characteristics. This makes the conventional decentralized control fail to generate good results even the computational difficulty could be overcome. Therefore, new technique has to be investigated.

A compromise between the centralized and decentralized approach is provided by an approach developed by Ikeda and Siljak [23], referred to as the overlapping decentralized method. This approach works effectively when the subsystems are interconnected in an "overlapped" way. We have found that the dynamics of the segmented telescope have this overlapping property. Due to the restrictions of the approach of [23], a modified overlapping method based only on the input-output characteristics of the system is developed and analyzed in this study. This modified approach has been successfully applied to the model of the segmented telescope through digital simulation. The performance requirements are met and the control laws are easy to implement in parallel. This method is further verified through the real-time implementation on the shape control of a segmented telescope test-bed.

This report is organized as follows: Chapter 2 introduces the theory and preliminaries about the overlapping decentralized control. Chapter 3 describes the model and performance requirements of the large segmented telescope model, **ASCIE** model. Design results with overlapping decentralized control are briefly presented. Chapter 4 describes a segmented telescope structure and the equipment. Chapter 5 describes the modelling of a segmented telescope test-bed. Chapter 6 describes the real-time implementation of the overlapping decentralized control on the segmented telescope test-bed. Chapter 7 presents the simplified decentralized control design. Chapter 8 presents the design and simulation results for the segmented telescope test-bed model with a secondary mirror. Chapter 9 introduces the overlapping decentralized control for a type of nonlinear systems. Chapter 10 describes the sensor failure detection and isolation with control reconfiguration.

Chapter 2

Theory and Preliminaries

In this section, we first present the fundamental theory for the overlapping decentralized control: inclusion principle. Then we present a modified overlapping decentralized control for the linear model of the segmented telescope.

2.1 Inclusion Principle

When centralized control is addressed, we assume that all the information available about the systems, and the calculations based on the information are centralized, that is, take place at a single location, as shown in Fig 2.1,

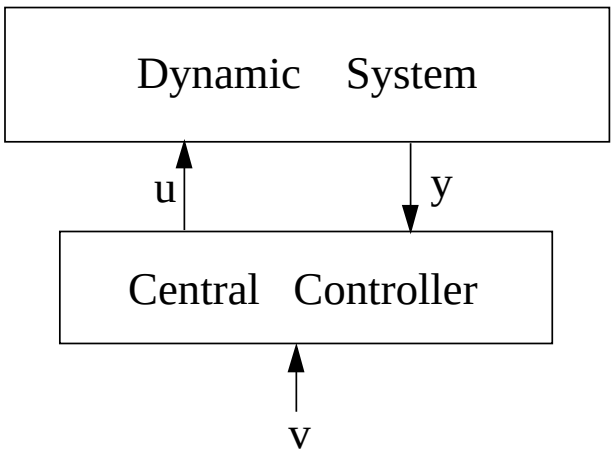

Figure 2.1: Centralized control system

where, u and y are the input and output of the system respectively, v is the external input to the system.

In contrast to the centralized control, the structures of some of the large scale systems are characterized by decentralization. For example, an electric power system has several control

substations, each being responsible for the operation of a portion of the entire network; an automated highway system may have many roadway traffic control stations, each being responsible for a particular section of freeway. Each control station provides inputs to a local subsystem based on the outputs from that local subsystem as shown in Fig 2.2, where, u_i and y_i are the input and output of subsystem i respectively, v_i is the external input to subsystem i, $i = 1, \cdots, N$. Subsystems may or may not be interconnected with each other.

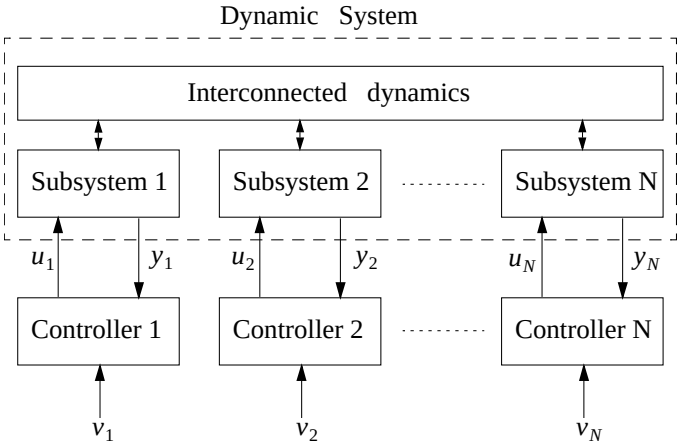

Figure 2.2: Decentralized control system

In the control of large scale systems, decentralized control is often the only feasible method to handle the computational complexity. However, subsystems are usually not completely decoupled as in the case of traffic systems and large space structures. They are mostly interconnected in an overlapped fashion. Ikeda and Siljak came up with an idea that involves expansion of the input, state space and output to make the overlapped subsystems isolated. The control laws are built for the expanded systems and applied to the original system. Overall stability is guaranteed under certain conditions. The idea is shown in Fig 2.3. The fundamental theory behind this idea is the Inclusion Principle [43].

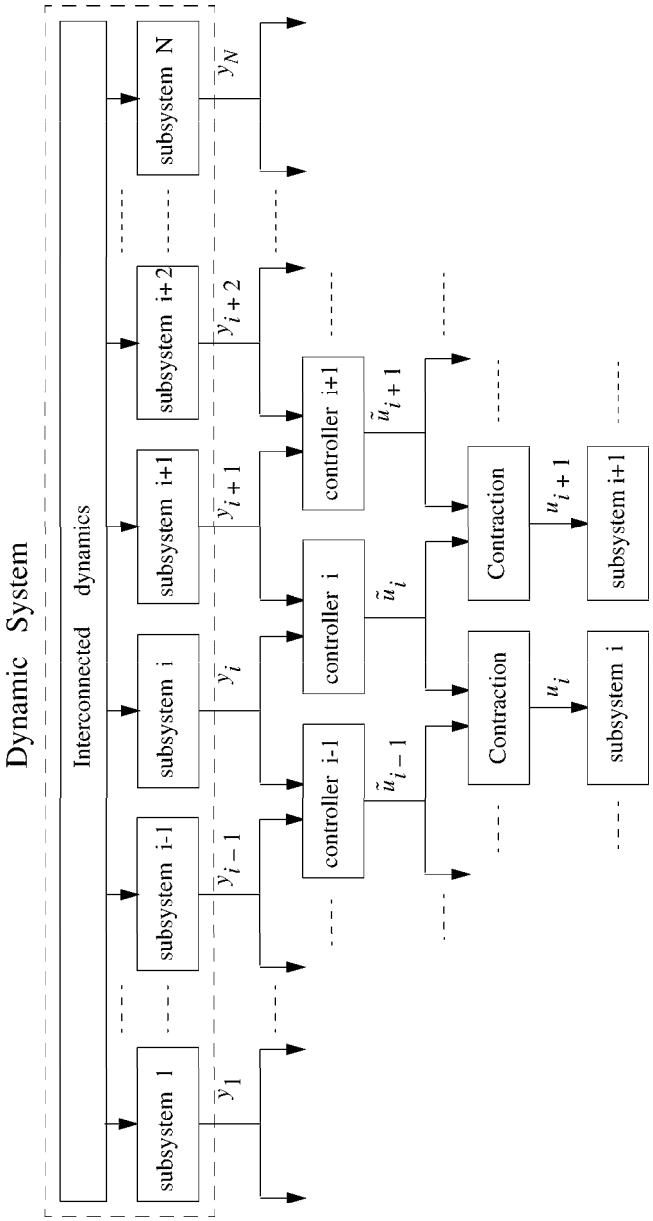

Figure 2.3: Overlapping decentralized control system

Let us consider the following differential vector equations $\mathbb{S}$

$$\dot{x} = f(t, x),$$

and $\tilde{\mathbb{S}}$

$$\dot{\tilde{x}} = \tilde{f}(t, \tilde{x}),$$

where $x(t) \in \mathcal{R}^n$ and $\tilde{x}(t) \in \mathcal{R}^{\tilde{n}}$ are the states of $\mathbb{S}$ and $\tilde{\mathbb{S}}$ at $t \in \mathcal{R}$, and $n \leq \tilde{n}$.

The functions $f : \mathcal{R} \times \mathcal{R}^n \to \mathcal{R}^n$ and $\tilde{f} : \mathcal{R} \times \mathcal{R}^{\tilde{n}} \to \mathcal{R}^{\tilde{n}}$ are assumed to be sufficiently smooth, so that solutions $x(t; t_0, x_0)$ and $\tilde{x}(t; t_0, \tilde{x}_0)$ of $\mathbb{S}$ and $\tilde{\mathbb{S}}$ exist and are unique for all initial conditions $(t_0, x_0) \in \mathcal{R} \times \mathcal{R}^n$ and $(t_0, \tilde{x}_0) \in \mathcal{R} \times \mathcal{R}^{\tilde{n}}$, and all $t \in T_0 = [t_0, +\infty)$.

We consider the linear transformations

$$\tilde{x} = Vx, \qquad x = U\tilde{x}, \tag{2.1}$$

where V is an $\tilde{n} \times n$ constant matrix will full column rank and U is an $n \times \tilde{n}$ constant matrix will full row rank. The inclusion concept is stated as follows:

Definition 2.1 *$\tilde{\mathbb{S}}$ includes $\mathbb{S}$ if there exists an ordered pair of matrices (U, V) such that $UV = I$, and for any $(t_0, x_0) \in \mathcal{R} \times \mathcal{R}^n$, $\tilde{x}_0 = Vx_0$ implies*

$$x(t; t_0, x_0) = U\tilde{x}(t; t_0, \tilde{x}_0), \quad \forall t \in T_0 \tag{2.2}$$

Theorem 2.1 *Suppose $\tilde{\mathbb{S}}$ includes $\mathbb{S}$ and $\tilde{x}_e = Vx_e$. Then, stability of the equilibrium $\tilde{x}_e$ of $\tilde{\mathbb{S}}$ implies stability of the equilibrium x_e of $\mathbb{S}$*

Proof: See [43].

2.2 Stabilization Problem of Decentralized Control

The solution to the stabilization problem of decentralized control is based on the decentralized fixed modes [45]. The following definition of "fixed modes" is a generalization of the centralized idea of uncontrollable modes and unobservable modes of the triple (C, A, B) and is basic to the problem of deciding whether a decentralized system can be stabilized.

Consider a linear time-invariant multivariable system with ν local control stations described by:

$$\dot{x} = Ax + \sum_{i=1}^{\nu} B_i u_i \tag{2.3}$$

$$y_i = C_i x, \qquad i = 1, \cdots, \nu \tag{2.4}$$

where $x \in \mathcal{R}^n$ is the state, $u_i \in \mathcal{R}^{m_i}$ and $y_i \in \mathcal{R}^{p_i}$ are the input and output respectively of

the ith local control station ($i = 1, \cdots, \nu$). The matrices A, B_i and C_i are real, constant, and of appropriate size. The decentralized control problem is to find ν local feedback control laws with dynamic compensation for (2.4) to stabilize the resultant closed loop system. The set of local feedback laws are assumed to be generated by the following feedback controllers:

$$\begin{aligned} \dot{z}_i &= F_i z_i + G_i y_i \\ u_i &= H_i z_i + K_i y_i + v_i \qquad\qquad i = 1, \cdots, \nu \end{aligned} \tag{2.5}$$

where $z_i \in \mathcal{R}^{n_i}$ is the state of ith sub-controller, $v_i \in \mathcal{R}^{m_i}$ is the ith local external input. F_i, G_i, H_i, K_i are real constant matrices of appropriate size.

Definition 2.2 (Wang, Davison [45]) *Consider the triple $(C, A, B) \in \mathcal{R}^{r\times n} \times \mathcal{R}^{n\times n} \times \mathcal{R}^{n\times m}$ and the two sets of integers $m_1, \cdots, m_\nu$ and $p_1, \cdots, p_\nu$ with $m = \sum_{i=1}^{\nu} m_i$ and $p = \sum_{i=1}^{\nu} p_i$, which specify system (2.4). Let $\mathbf{K}$ be the set of block diagonal matrices as follows:*

$$\mathbf{K} \triangleq \{\boldsymbol{K} | \boldsymbol{K} = \mathbf{Block\ Diag}[\boldsymbol{K_1}, \cdots, \boldsymbol{K}_\nu],\ \ \boldsymbol{K_i} \in \mathcal{R}^{\mathbf{m_i}\times\mathbf{p_i}}, \mathbf{i} = \mathbf{1}, \cdots, \nu\}. \tag{2.6}$$

Then the set of fixed modes of (C, A, B) with respect to $\mathbf{K}$ denoted as $\wedge(C, A, B, \mathbf{K})$ is defined as follows:

$$\wedge(C, A, B, \mathbf{K}) \triangleq \{\cap\sigma(\mathbf{A} + \mathbf{B}\boldsymbol{K}\mathbf{C}),\ \ \boldsymbol{K} \in \mathbf{K}\} \tag{2.7}$$

where $\sigma(A + B\boldsymbol{K}C)$ denotes the set of eigenvalues of $(A + B\boldsymbol{K}C)$.

The following theorem gives a solution to the decentralized stabilization problem.

Theorem 2.2 (Wang, Davison [45]) *Consider the system (C, A, B) of (2.4). Let $\mathbf{K}$ be the set of block diagonal matrices defined in (2.6). Then a necessary and sufficient condition for the existence of a set of decentralized controllers such that the closed-loop system is asymptotically stable is that:*

$$\wedge(C, A, B, \mathbf{K}) \subset \mathcal{C}^- \tag{2.8}$$

where $\mathcal{C}^-$ denotes the open left-half complex plane.

Corollary 2.1 *There always exists a set of dynamical controllers given by (2.5) which stabilize the system (2.4) if*

$$\sigma(A) \subset \mathcal{C}^-. \tag{2.9}$$

Proof: The fixed modes of (C, A, B) with respect to $\mathbf{K}$ are defined in (2.7). Since $\mathbf{K}$ contains the null matrix, $\wedge(C, A, B, \mathbf{K}) \subseteq \sigma(A)$. This means the set of fixed modes of (C, A, B)

constitute a subset of the eigenvalue space of A. This proves the corollary.

Remark: Most large flexible structures satisfy condition (2.9) in the above corollary, which indicates that decentralized control is a feasible method for controlling LFSS.

2.3 Sufficient Stability Conditions for Decentralized Control

Let $G(s)$ be a square plant that is to be controlled using a block diagonal controller

$$K(s) = \begin{bmatrix} k_1(s) & 0 & \cdots & 0 \\ 0 & k_2(s) & \cdots & 0 \\ \vdots & \vdots & \vdots & \vdots \\ 0 & 0 & \cdots & k_\nu(s) \end{bmatrix} \tag{2.10}$$

where k_i is the transfer function of the controller for subsystem i. We introduce

$$\tilde{G}(s) \triangleq \begin{bmatrix} g_{11}(s) & 0 & \cdots & 0 \\ 0 & g_{22}(s) & \cdots & 0 \\ \vdots & \vdots & \vdots & \vdots \\ 0 & 0 & \cdots & g_{\nu,\nu}(s) \end{bmatrix} \tag{2.11}$$

Let's define the off-diagonal elements in $G(s)$ by

$$\triangle(s) \triangleq G - \tilde{G}. \tag{2.12}$$

Therefore, $\triangle(s)$ can be treated as the plant uncertainty in the design, as shown in Figure 2.4.

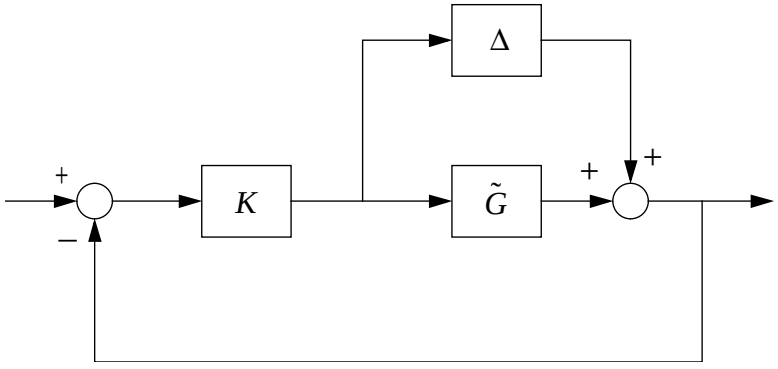

Figure 2.4: Modified control system block diagram with model uncertainty

Let's define the sensitivity and complementary sensitivity for the block diagonal plant

$\tilde{G}(s)$ as follows

$$\begin{aligned} \tilde{S} &\triangleq (I + \tilde{G}K)^{-1} \\ \tilde{T} &\triangleq I - \tilde{S} = \tilde{G}K(I + \tilde{G}K)^{-1}. \end{aligned} \tag{2.13}$$

The following theorem provides a sufficient stability condition based on the singular values of $\tilde{G}(s), \tilde{T}(s)$, and $\triangle(s)$.

Theorem 2.3 (Chiang and Safonov [41]) *Consider the system in Figure 2.4. Suppose that the perturbation $\triangle(s)$ has no unstable poles and that the feedback K stabilizes the nominal plant $\tilde{G}(s)$. If for all frequencies*

$$\frac{\bar{\sigma}(\triangle)}{\underline{\sigma}(\tilde{G})}\bar{\sigma}[\tilde{G}K(I + \tilde{G}K)^{-1}] \leq 1, \tag{2.14}$$

then K stabilizes the plant G.

Proof: See Chiang and Safonov [14].

Corollary 2.2 *Consider the system in Figure 2.4. Suppose that the perturbation $\triangle(s)$ has no unstable poles and that the feedback K stabilizes the nominal plant $\tilde{G}(s)$. If for all frequencies*

$$\frac{\bar{\sigma}(\triangle)}{\min_i \underline{\sigma}(g_{ii})} \max_i \bar{\sigma}(T_i) \leq 1 \tag{2.15}$$

where $T_i = g_{ii}k_i(I + g_{ii}k_i)^{-1}, \;\; i = 1, \cdots, \nu$, then K stabilizes the plant G.

Proof: From the definition of $\tilde{G}$ and $\tilde{T}$, we have

$$\tilde{T} = diag\{T_1, \cdots, T_\nu\}$$

$$\bar{\sigma}(\tilde{T}) = \max_i \bar{\sigma}(T_i)$$

$$\underline{\sigma}(\tilde{G}) = \min_i \underline{\sigma}(g_{ii}).$$

Consequently, the lemma is proved by applying the above theorem.

The significance of the above corollary is that the size of interconnections ($\triangle$) put some limitations on the bandwidth of the subsystems. Accordingly, the decentralization should try to make $\underline{\sigma}(g_{ii})$ as large as possible and $\bar{\sigma}(\triangle)$ as small as possible.

2.4 Overlapping Decentralized Control

In order to expand the state space of the original system based on the *Inclusion Principle*, we need some physical information about the chosen states. In the case of LFSS, input/output

models developed using frequency domain system identification techniques are more accurate than the state space models based on finite element methods. The method of [23] developed for state space models is modified to be applicable to the linear input-output models of the LFSS.

Consider a linear time-invariant multivariable system in (2.4) The overlapping decentralized control problem is to find ν local feedback control laws with dynamic compensation for (2.4) to stabilize the resultant closed loop system. The set of local feedback laws are assumed to be generated by the following feedback controllers:

$$\begin{aligned} \dot{z}_i &= \bar{F}_i z_i + \bar{G}_i \bar{y}_i \\ \bar{u}_i &= \bar{H}_i z_i + \bar{K}_i \bar{y}_i + \bar{v}_i \qquad\qquad i = 1, \cdots, \nu \end{aligned} \tag{2.16}$$

where $z_i \in \mathcal{R}^{n_i}$ is the state of ith sub-controller, $\bar{v}_i \in \mathcal{R}^{m_i + m_{i+1}}$ is the ith local external input. $\bar{F}_i, \bar{G}_i, \bar{H}_i, \bar{K}_i$ are real constant matrices of appropriate size. $\bar{y}_i$ are defined as follows:

$$\bar{y}_i \triangleq \begin{bmatrix} y_i \\ y_{i+1} \end{bmatrix}, \qquad i = 1, \cdots, \nu - 1 \tag{2.17}$$

$$\bar{y}_\nu \triangleq \begin{bmatrix} y_\nu \\ y_1 \end{bmatrix} \tag{2.18}$$

The control input for each subsystem is obtained as follows:

$$\begin{aligned} u_i &= \frac{1}{2} \begin{bmatrix} \mathbf{0_{m_i \times m_{i-1}}} & \mathbf{I_{m_i}} \end{bmatrix} \cdot \bar{u}_{i-1} + \frac{1}{2} \begin{bmatrix} \mathbf{I_{m_i}} & \mathbf{0_{m_i \times m_{i+1}}} \end{bmatrix} \cdot \bar{u}_i, \quad i = 1, \cdots, \nu - 1 \\ u_\nu &= \frac{1}{2} \begin{bmatrix} \mathbf{0_{m_\nu \times m_{\nu-1}}} & \mathbf{I_{m_\nu}} \end{bmatrix} \cdot \bar{u}_{\nu-1} + \frac{1}{2} \begin{bmatrix} \mathbf{I_{m_\nu}} & \mathbf{0_{m_\nu \times m_1}} \end{bmatrix} \cdot \bar{u}_\nu \end{aligned} \tag{2.19}$$

where $\mathbf{0}$ is a matrix of appropriate size with zero elements, and $\mathbf{I}$ is an identity matrix of appropriate size. The solution to the stabilization problem is based on *the overlapping decentralized fixed modes*. The following definition of "overlapping decentralized fixed-modes" is a generalization of the centralized idea of uncontrollable modes and unobservable modes of the triple $(\bar{C}, A, \bar{B})$, and is basic to the problem of deciding whether a decentralized system can be stabilized.

Definition 2.3 *Consider the triple* $(\bar{C}, A, \bar{B})$. *Let* $\bar{\mathbf{K}}$ *be the set of block diagonal matrices defined as follows:*

$$\bar{\mathbf{K}} \triangleq \{\bar{K} | \bar{K} = block\ \ diag[\bar{K}_1, \cdots, \bar{K}_\nu], \bar{K}_i \in \mathcal{R}^{(m_i + m_{i+1}) \times (p_i + p_{i+1})}, i = 1, \cdots, \nu\} \tag{2.20}$$

where $\bar{B}$ and $\bar{C}$ are defined as follows:

$$\begin{aligned}
\bar{B} &\triangleq BS = \left[\begin{array}{ccc} \bar{B}_1 & \cdots & \bar{B}_\nu \end{array} \right] \\
\bar{C} &\triangleq TC = \left[\begin{array}{c} \bar{C}_1 \\ \vdots \\ \bar{C}_\nu \end{array} \right] \\
T &= \left[\begin{array}{ccccc} \mathbf{I} & \mathbf{0} & \mathbf{0} & \cdots & \mathbf{0} \\ \mathbf{0} & \mathbf{I} & \mathbf{0} & \cdots & \mathbf{0} \\ \mathbf{0} & \mathbf{I} & \mathbf{0} & \cdots & \mathbf{0} \\ \mathbf{0} & \mathbf{0} & \mathbf{I} & \cdots & \mathbf{0} \\ \mathbf{0} & \mathbf{0} & \mathbf{I} & \cdots & \mathbf{0} \\ \vdots & \vdots & \vdots & \vdots & \vdots \\ \mathbf{0} & \mathbf{0} & \mathbf{0} & \cdots & \mathbf{I} \\ \mathbf{0} & \mathbf{0} & \mathbf{0} & \cdots & \mathbf{I} \\ \mathbf{I} & \mathbf{0} & \mathbf{0} & \cdots & \mathbf{0} \end{array} \right] \\
S &= (T^T T)^{-1} T^T
\end{aligned} \tag{2.21}$$

Then the set of overlapping decentralized fixed modes of (C, A, B) with respect to $\bar{\mathbf{K}}$ denoted as $\wedge(\bar{C}, A, \bar{B}, \bar{\mathbf{K}})$ is defined as follows:

$$\wedge(\bar{C}, A, \bar{B}, \bar{\mathbf{K}}) \triangleq \{\cap\sigma(A + \bar{B}\bar{K}\bar{C}),\ \ \bar{K} \in \bar{\mathbf{K}}\} \tag{2.22}$$

where $\sigma(A + \bar{B}\bar{K}\bar{C})$ denotes the set of eigenvalues of $(A + \bar{B}\bar{K}\bar{C})$.

The following theorem gives a solution to the stabilization problem.

Theorem 2.4 *Consider the system (C, A, B) of (2.4). Then a necessary and sufficient condition for the existence of a set of overlapping decentralized controllers such as (2.16) so that the closed loop system is asymptotically stable is that:*

$$\wedge(\bar{C}, A, \bar{B}, \bar{\mathbf{K}}) \subset \mathcal{C}^- \tag{2.23}$$

where $\mathcal{C}^-$ denotes the open left-hand complex plane.

Proof: The original system (2.4) can be rewritten with augmented input vector $\bar{u}$ and

output vector $\bar{y}$ as the following:

$$\begin{aligned}
\dot{x} &= Ax + \sum_{i=1}^{\nu} B_i u_i \\
&= Ax + \frac{1}{2}\left[\begin{array}{cc} B_1 & B_2 \end{array}\right]\left[\begin{array}{c} u_1 \\ u_2 \end{array}\right] + \frac{1}{2}\left[\begin{array}{cc} B_2 & B_3 \end{array}\right]\left[\begin{array}{c} u_2 \\ u_3 \end{array}\right] + \cdots + \frac{1}{2}\left[\begin{array}{cc} B_\nu & B_1 \end{array}\right]\left[\begin{array}{c} u_\nu \\ u_1 \end{array}\right] \\
&= Ax + \sum_{i=1}^{\nu} \bar{B}_i \bar{u}_i \qquad (2.24) \\
\bar{y} &= Ty = \left[\begin{array}{c} \bar{y}_1 \\ \vdots \\ \bar{y}_\nu \end{array}\right], \qquad \bar{y}_i = \bar{C}_i x, \qquad\qquad i = 1, \cdots, \nu
\end{aligned}$$

where

$$\begin{aligned}
\bar{u}_i &= \left[\begin{array}{c} u_i \\ u_{i+1} \end{array}\right], \qquad for \quad i = 1, \cdots, \nu - 1 \\
\bar{u_\nu} &= \left[\begin{array}{c} u_\nu \\ u_1 \end{array}\right] \qquad (2.25)
\end{aligned}$$

0 is a matrix with zero elements of appropriate size, and **I** is identity matrix of appropriate size.

This augmentation leads to the proof immediately by applying theorem 4.1.

Lemma 2.1 *If there exists a set of decentralized control laws as in (2.5) that stabilizes the system in (2.4), then there always exists a set of overlapping decentralized control laws as in (2.16) that can stabilize the same system. In other words, if the system does not have unstable fixed modes with respect to* $\boldsymbol{K}$ *as defined in (2.6), the overlapping control will not introduce unstable fixed modes with respect to* $\bar{\boldsymbol{K}}$ *as defined in (2.20).*

Proof: Assume that a block diagonal matrix K as defined in (2.6) has been found that satisfies the following condition:

$$\sigma(A + BKC) \subset \mathcal{C}^-.$$

Construct $\bar{K}$ as defined in (2.20) in the following way:

$$\bar{K}_i = \frac{1}{2}\left[\begin{array}{cc} K_i & 0 \\ 0 & K_{i+1} \end{array}\right], \qquad i = 1, \cdots, \nu.$$

Then

$$\sigma(A + \bar{B}\bar{K}\bar{C}) = \sigma(A + BKC) \subset \mathcal{C}^{-}.$$

The Lemma is proved.

The following numerical example shows that in certain cases when the interconnections are strong, decentralized control may fail to stabilize the system, whereas the overlapping control method can stabilize the system.

Consider the following system:

$$\begin{aligned}
\dot{x} &= \begin{bmatrix} -1 & 0 & 0 & 0 & 0 \\ 0 & 2 & 0 & 0 & 0 \\ 0 & 0 & -1 & 0 & 0 \\ 0 & 0 & 0 & 3 & 0 \\ 0 & 0 & 0 & 0 & -1 \end{bmatrix} x + \begin{bmatrix} 1 & 0 & 0 \\ 0 & 1 & 0 \\ 0 & 1 & 0 \\ 0 & 0 & 1 \\ 0 & 0 & 1 \end{bmatrix} \begin{bmatrix} u_1 \\ u_2 \\ u_3 \end{bmatrix} \\
\begin{bmatrix} y_1 \\ y_2 \\ y_3 \end{bmatrix} &= \begin{bmatrix} 1 & 1 & 0 & 0 & 0 \\ 0 & 0 & 1 & 1 & 0 \\ 0 & 0 & 0 & 0 & 1 \end{bmatrix} x
\end{aligned}$$

with $\mathbf{K} = \{K | K = diag[k_1, k_2, k_3], k_1, k_2, k_3 \in \mathcal{R}\}$. In this case,

$$det[\lambda I - (A + BKC)] = (\lambda - 2)(\lambda - 3)(\lambda + 1 - k_1)(\lambda + 1 - k_2)(\lambda + 1 - k_3).$$

Clearly the system has two unstable fixed modes, $\lambda = 2$ and $\lambda = 3$, according to the definition. Hence the system cannot be stabilized using decentralized control. The block diagram of the system is shown in Figure 2.5.

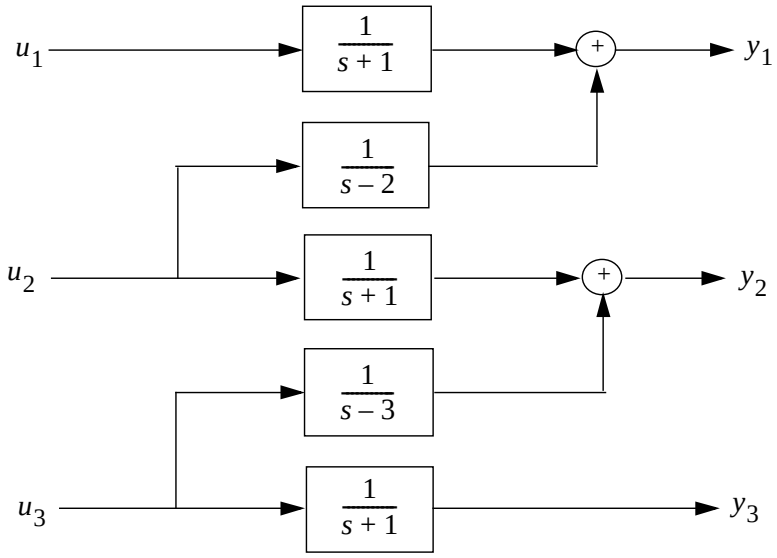

Figure 2.5: Block diagram of the system

However the input-output overlapping decentralized control law

$$\begin{aligned}
\bar{u}_1 &= \begin{bmatrix} u_1 \\ u_2 \end{bmatrix} = \begin{bmatrix} 0 & 0 \\ -12 & 0 \end{bmatrix} \begin{bmatrix} y_1 \\ y_2 \end{bmatrix} \\
\bar{u}_2 &= \begin{bmatrix} u_2 \\ u_3 \end{bmatrix} = \begin{bmatrix} 0 & 0 \\ -16 & 0 \end{bmatrix} \begin{bmatrix} y_2 \\ y_3 \end{bmatrix} \\
\bar{u}_3 &= \begin{bmatrix} u_3 \\ u_1 \end{bmatrix} = \begin{bmatrix} -2 & 0 \\ 0 & -2 \end{bmatrix} \begin{bmatrix} y_3 \\ y_1 \end{bmatrix}
\end{aligned}$$

leads to a closed loop with poles at -6.7016, -5.6458, -1, -0.3542, and -0.2984. Hence the system is stabilizable with the overlapping decentralized control.

Corollary 2.3 *There always exists a set of dynamical controllers given by (2.16) that stabilize the system (2.4) if*

$$\sigma(A) \subset \mathcal{C}^-. \tag{2.26}$$

Proof: Same as the proof of *Corollary* 1.

Remark: Most of the large flexible structures satisfy condition (2.26), which indicates that the modified overlapping decentralized control is feasible for controlling LFSS.

Chapter 3

Centralized, Decentralized, and Overlapping Control Designs for a Segmented Telescope

The accurate control of the segments of large segmented telescopes to achieve the desired shape could open the way for the construction of much larger telescopes with much better capabilities. In this chapter, we consider the centralized, decentralized and overlapping approaches to designing controllers for shape control of a segmented telescope. In the centralized approach, all the segments and interconnections are considered to be a single dynamical system. In the decentralized case, the interconnections between the segments are neglected for control design purposes. In the overlapping decentralized approach, overlapped segments are considered to be isolated subsystems. In each case, we design controllers using the H_∞ robust control approach. In the centralized control case, the disturbances are rejected over a wide frequency range and all performance requirements are met. The order of the centralized controller, however, is high, which makes it difficult to implement in real time. The decentralized control approach greatly reduces the computational and hardware requirements at the expense of performance deterioration. The overlapping approach is shown to be a trade-off between the centralized and decentralized cases that provides sufficient flexibility to meet both performance and computational requirements.

3.1 Introduction

The performance of astronomical systems is directly related to the size of their reflectors. Since it is very difficult to cast mirrors larger than 7 meters in diameter from a single piece of glass, performance appears to be limited. However one way to improve the performance of optical systems is to increase the size of the mirror by using an array of mirror segments. The problem with segmented optics is that to perform like conventional optics, stringent position-

ing precision is required. Optical performance requires positioning of the mirror segments to achieve the desired mirror shape within an accuracy of a fraction of the wavelength of light. No support structure can provide the mechanical rigidity needed to maintain the position of the mirror segments to such an accuracy. To compensate for the mechanical imperfections, the deformations due to the gravity and thermal loads, and to attenuate the seismic- or maneuver-induced vibrations, the mirror segments must therefore be actively controlled.

Large Flexible Space Structures (LFSS) pose a challenging problem in control system design because of their large size, large modelling uncertainty, low rigidity, low damping, high modal density and extremely low frequency modes. The approaches considered for the control of LFSS have generally been directed toward "centralized control". However, the high-order LFSS model often results in a high-order controller which can not be implemented by real-time parallel processing. In real-time implementation, the order of the controller is limited by the hardware and computational complexity. For that reason, a decentralized control approach may be more appropriate. The motivation for obtaining a decentralized controller is simplicity of implementation which makes parallel computation feasible. In this article we investigate three different approaches for controlling a segmented telescope developed at the Lockheed Palo-Alto Research Laboratory which is designed to represent a LFSS system. We considered initially the centralized approach in which the overall system is treated as a single isolated system. We developed a centralized stabilizing controller based on H_∞ robust control to meet the performance requirements. The order and complexity of the controller was high, making real-time implementation difficult if at all possible. This difficulty motivated the design of a decentralized scheme in which each segment is treated as an isolated subsystem. The H_∞ robust control approach is used to develop six controllers, one for each panel, by neglecting all interactions between the segments. The decentralized scheme developed is easy to implement but does not meet the performance requirements because the neglected interconnections between the segments are rather strong and influence performance. A compromise between the centralized and decentralized approaches is provided by an approach developed by Ikeda and Siljak [23], referred to as the overlapping decentralized method. This approach works effectively when the subsystems are interconnected in an "overlapped" way. We have found that the dynamics of the segmented telescope have this overlapping property. Using [23], a modified overlapping method based only on the input-output characteristics of the system is developed and analyzed. This modified approach has been successfully applied to the model of the segmented telescope. The performance requirements are met, and the control laws are easy to implement in parallel.

The chapter is organized as follows: First, we describe the model of a segmented telescope and the performance requirements. Then we formulate the control design into a standard H_∞ robust control problem, and a central controller is designed. Next we consider the decentralized control approach and then present the modified overlapping method. Finally we present simulation results with different control approaches.

3.2 Description of the ASCIE test-bed and Design Specification

3.2.1 Description of the Structure

The Advanced Structure/Control Integrated Experiment **ASCIE** is a laboratory experiment to study the interaction between the controls and the structure in large flexible systems [11]. The **ASCIE** is an optical system. It emulates a f/1.25 Cassegrain telescope. It operates in the visible spectrum. It comprises three main components: a truss, a primary mirror and a secondary mirror. The truss supports the primary mirror. Some of its elements extend to support the secondary mirror. The primary mirror is composed of seven hexagonal segments, 6 segments around a central one. The central segment is locked to the truss structure. Each of the surrounding segments is attached to the truss at three node points through linear electromagnetic actuators. The segments are shaped so that when they are all in their nominal positions the surface figure is a sphere with focus at the secondary mirror. Each segment to segment interface is instrumented with two inductance sensors. The sensors are fixed to the back surface of each segment and measure the displacement of the edges of each segment relative to the edges of its nearest neighbors.

A 70-state linear model was obtained and validated through a series of system identification experiments performed by Dr. Alain Carrier and his colleagues [12]. In this chapter, we use this model for design, analysis, and simulations. The state-space representation of the open-loop structure is

$$\begin{aligned} \dot{x} &= Ax + Bu \\ y &= Cx + Du, \end{aligned} \tag{3.1}$$

where $A \in \mathcal{R}^{70\times 70}$, $B \in \mathcal{R}^{70\times 18}$, $C \in \mathcal{R}^{24\times 70}$, and $D \in \mathcal{R}^{24\times 18}$. State vector x consists of modal amplitudes and modal rates. Since this model is developed using input output data, x does not necessarily represent any physical quantities; $y = [y_1, y_2, \cdots, y_{24}]'$ is the output vector; y_i represents the output of edge sensor E_i in mm; and $i = 1, 2, \cdots, 24$. The 18 linear electromagnetic actuators working in the current mode are used to provide the required force command to keep the segments in the desired shape. The input vector $u = [u_1, u_2, \cdots, u_{18}]'$ represents the forces applied to the structure. The dynamics of these actuators are neglected so that the output force is represented as $u_i = k_a I_i, i = 1, \cdots, 18$, where I_i is the input current to motor i in amp, u_i is the output force of motor i in $Newton$, and k_a is the force constant.

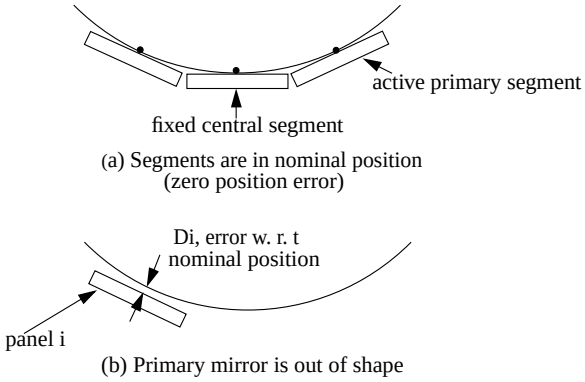

Figure 3.1: Primary mirror nominal shape and shape error

3.2.2 Performance Requirements

The segment alignment control system is tasked to achieve the optical quality of a single continuous mirror. Nominally, the segments must form a sphere as shown in Fig 3.3. In the off nominal case, the center of each segment will deviate from the nominal tangent point on the sphere. The deviation of panel i, denoted as D_i, is also defined in Fig 3.3. Error D_i's are obtained from the 24 edge sensor measurements through a geometric transformation. The wavelength of red light is 0.65 micron. The error has to be within an accuracy of a fraction of the wavelength of light. Therefore the performance requirements are for the root-mean-square (RMS) value of $D_i, i = 1, 2, \cdots, 6$ to be less than 1 micron at steady state.

3.3 Robust Controller Design: Centralized Approach

In this section, we describe the controller design technique used in the centralized control approach. It is based on a mixed-sensitivity H_∞ approach of robust control. Fig 3.4 is the block diagram of the control system, where $G(s)$ represents the transfer function of the plant, $K(s)$ represents the transfer function of the controller, d is the external disturbance, and n is the sensor noise.

Then the system output is given by

$$y = S(s)d - T(s)n \tag{3.2}$$

where $S(s)$ is the transfer function from d to y, known as sensitivity function, and $T(s)$ is the transfer function from n to y, known as complementary sensitivity function. They are

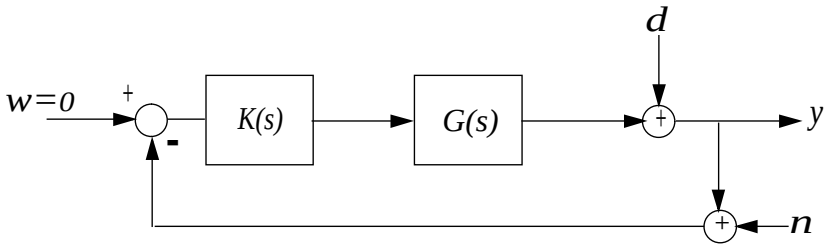

Figure 3.2: Control system block diagram

defined as follows:

$$\begin{aligned} S &\triangleq (I + GK)^{-1} \\ T &\triangleq I - S. \end{aligned} \tag{3.3}$$

The goal of the controller is to keep the output y as small as possible in the presence of disturbance and noise.

The disturbance is typically a low-frequency signal, and therefore it will be successfully rejected if the maximum singular value of $S(j\omega)$ is made small over the same low frequencies. To do this, we select a scalar low-pass filter $W_1(s)$ with a bandwidth equal to that of the disturbance and then find a stabilizing controller that minimizes $\|W_1^{-1}(j\omega)S(j\omega)\|_\infty$.

Another issue of control is noise attenuation. Usually noise is a high-frequency signal, so the maximum singular value of $T(j\omega)$ has to be small at high frequencies where the noise lies. Very similar to the above, we could select a high-pass filter $W_2(s)$ and find a stabilizing controller that minimizes $\|W_2^{-1}(j\omega)T(j\omega)\|_\infty$.

If we augment the plant $G(s)$ with the weights $W_1(s)$ and $W_2(s)$ as shown in Fig 3.5, it becomes a general control configuration as in Fig 3.6 with the transfer function from w to z being

$$T_{zw} = \begin{bmatrix} W_1^{-1}S \\ W_2^{-1}T \end{bmatrix} \tag{3.4}$$

where w represents the external input and z represents the augmented output. The controller transfer function $K(s)$ is derived from the following minimization problem:

$$\min_{K(s)} \left\| \begin{array}{c} \gamma W_1^{-1}S \\ W_2^{-1}T \end{array} \right\|_\infty \tag{3.5}$$

where γ is a design parameter. This can be solved efficiently using the algorithm of Doyle et al. [16], and by increasing γ iteratively, an optimal solution is approached.

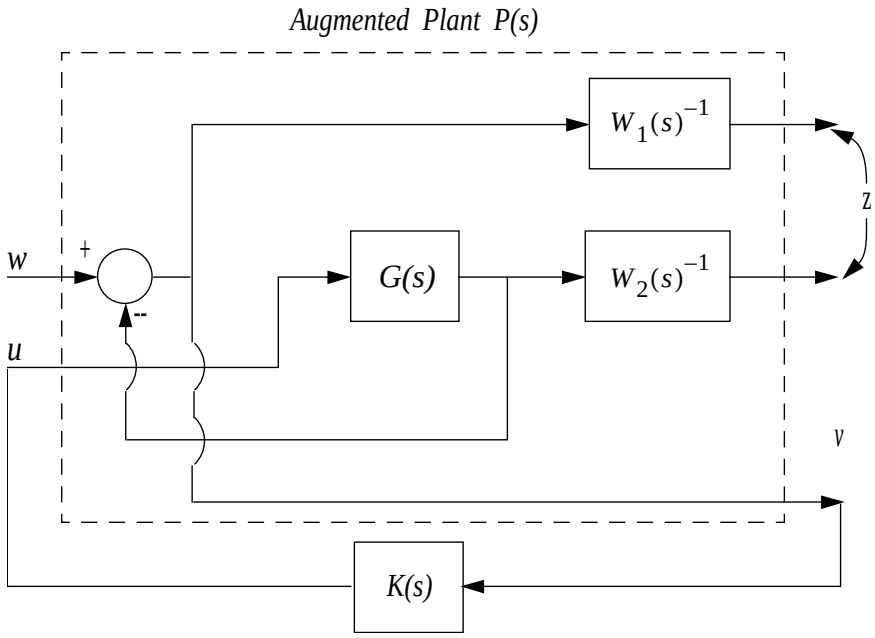

Figure 3.3: Control system block diagram with augmented plant

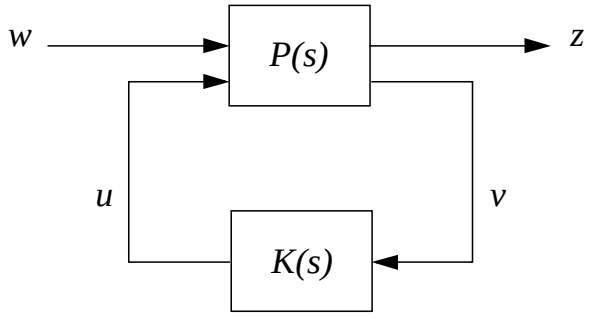

Figure 3.4: General control configuration

From the definitions of sensitivity functions, we have

$$S + T \equiv I. \tag{3.6}$$

Ideally, we want $S(j\omega)$ small to obtain the benefits of feedback and $T(j\omega)$ small to avoid sensitivity to noise and modelling uncertainties at high frequencies. Unfortunately, these requirements cannot be satisfied simultaneously at any frequency, as is clear from the above equality. In addition, the state space model has RHP transmission zeros. The distance from a RHP zero to the origin in the complex plane puts an upper limit to the frequency range of the disturbance rejection [44]. In this case, the plant is non-square with 24 outputs and 18 inputs. To perform the H_∞ optimal design, the plant has to be square. We select 18 measurements out of 24 sensors to make the RHP zero as far from its origin as possible. In the rest of the paper, singular-value Bode diagrams will be used to measure the multi-input

multi-output (MIMO) system performance in frequency domain. A singular-value Bode diagram is a Bode diagram of the singular values of MIMO system transfer function. It is a good measure of MIMO system performance since the singular values give better information about the gain of a MIMO plant. The open-loop singular-value Bode diagram of the ASCIE model is shown in Fig 3.7.

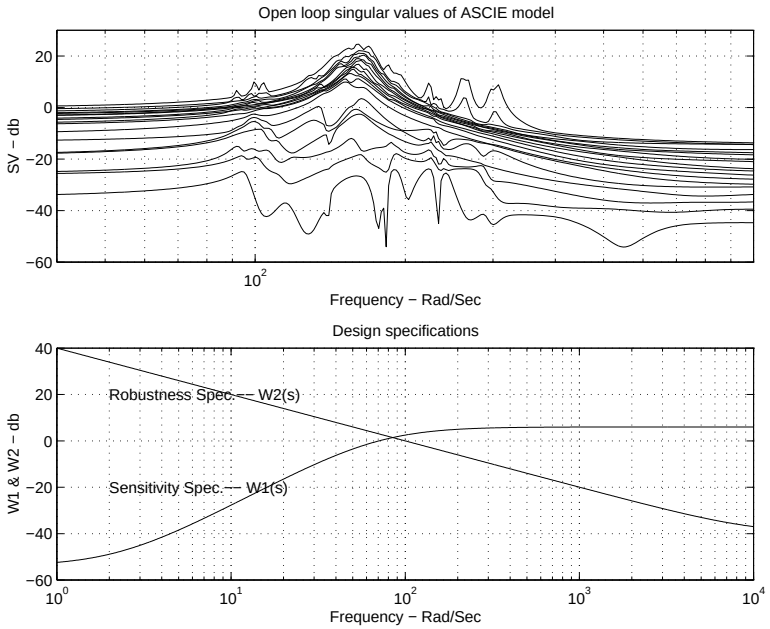

Figure 3.5: General control configuration

The open-loop RMS value of the error $D_i, i = 1, 2, \cdots, 6$ is about 100 microns in the presence of disturbance. The disturbances are typically quasi-static such as gravity loads, thermally induced loads, actuators bias errors and drifts, steady state of outside disturbances. The power spectrum is contained in the frequency range of $0 - 0.1 rad/sec$. To accomplish the performance requirements, the control system must attain at least a $100 : 1$ reduction for disturbance over the same frequency range. In this design, the disturbance rejection is the main concern of the performance requirements. Therefore, the control system bandwidth is not a big issue here. However the bandwidth cannot be arbitrarily small. As we will see in the following design, there is a crossover frequency ω_S in the singular value Bode diagram of the sensitivity function S such that $\|S(j\omega)\|_\infty < 1$ when $\omega < \omega_S$, $\|S(j\omega)\|_\infty \geq 1$ when $\omega \geq \omega_S$. Hence the disturbances with frequency less than ω_S will be attenuated with closed-loop control. For the closed-loop system, the crossover frequency ω_S is always less than the control system bandwidth, denoted as ω_T. In the design, we try to push ω_S to the right as far as possible in order to attenuate the disturbance within a wide frequency range. Therefore, ω_T cannot be too small. Since the actuators have a 25 Hz bandwidth, the control bandwidth is therefore limited to this frequency. In this design, we require the loop gain to roll off at least at $20db$ per decade starting at about $100 rad/sec$ (16 Hz) to take care of

the modelling uncertainties at high frequencies. Also in the design, the singular value Bode diagram of T does not necessarily have to have the same shape as that of $W_2(s)$ as long as $\|T(j\omega)\|_\infty \leq W_2(j\omega)$ is satisfied. We choose the following weights (also see Fig 3.3) to perform the H_∞ control synthesis using the Robust-Control Toolbox [14].

$$\begin{aligned} W_1(s) &= \frac{(s+2.236)^2}{(0.707s+50)^2} \\ W_2(s) &= \frac{10(s+10000)}{(1000s+1)}. \end{aligned} \tag{3.7}$$

The norm in (3.5) is minimized through iterations on γ. The larger γ is, the more penalty we put on the sensitivity function. The maximum value of γ for this problem is found to be 0.4269.

With this design, we have a sensitivity reduction of 100 : 1 at the low frequency up to $1rad/sec$. The complementary sensitivity singular values start to roll off from $100rad/sec$ as shown in Fig 3.8. The original model has 70 states and 18 inputs and outputs. With 3 states added to each input-output channel by the weights $W_1(s), W_2(s)$, the final augmented plant has a total 124 states. Therefore the order of the resultant central controller is 124. More important, this centralized control algorithm can not be implemented in parallel.

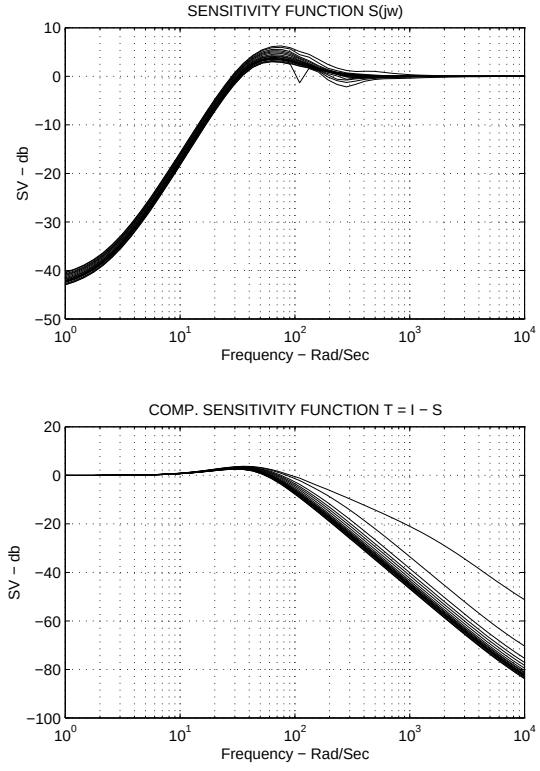

Figure 3.6: Singular value Bode diagram with centralized control

Comment 3.1: The centralized control design presented above requires a single processor

for real-time implementation. As the number of segments increase, in order to create a much large primary mirror the number of computations will increase so much that a single processor may not be adequate to do the job in real time. The choices are to either replace the processor with a faster one or use different control methods that can allow parallel processing that can be achieved with a set of less fast and lower cost processors. In the following sections we explore this second possibility by proposing a decentralized and overlapping decentralized control design approaches.

3.4 Decentralized Control Design

As mentioned in the previous section, the H_∞ central controllers designed for LFSS have the same order as that of the augmented model of the structure. Since the controller order is limited by real-time implementation constraints, the order of the mathematical model of the structure must be kept as small as possible, or in the case where the mathematical model of the structure is of large order, decentralized control together with parallel processing can greatly reduce the computational effort. In this case, we are interested in a decentralized control technique where each sub-controller controls the three actuators of each segment and uses measurements from the sensors of the corresponding segment. The problem is formulated as follows.

Consider a linear time-invariant multivariable system with ν local control stations described by:

$$\begin{aligned} \dot{x} &= Ax + \sum_{i=1}^{\nu} B_i u_i \\ y_i &= C_i x, \qquad\qquad i = 1, \cdots, \nu \end{aligned} \tag{3.8}$$

where $x \in \mathcal{R}^n$ is the state and $u_i \in \mathcal{R}^{m_i}$ and $y_i \in \mathcal{R}^{p_i}$ are the input and output, respectively, of the ith local control station ($i = 1, \cdots, \nu$). The matrices A, B_i and C_i are real, constant, and of appropriate size. The decentralized control problem is to find ν local feedback control laws with dynamic compensation for (3.8) to stabilize the resultant closed-loop system. The set of local feedback laws is assumed to be generated by the following feedback controllers:

$$\begin{aligned} \dot{z}_i &= F_i z_i + G_i y_i \\ u_i &= H_i z_i + K_i y_i + v_i, \qquad\qquad i = 1, \cdots, \nu \end{aligned} \tag{3.9}$$

where $z_i \in \mathcal{R}^{n_i}$ is the state of ith local controller and $v_i \in \mathcal{R}^{m_i}$ is the ith local external input. F_i, G_i, H_i, and K_i are real constant matrices of appropriate size.

The solution to the above stabilization problem is discussed in the previous chapter We apply the standard two-block mixed-sensitivity H_∞ [41] technique to each panel of the

segmented telescope. In terms of decentralized control, the local controller $k_i(s)$ is designed independently and then all the loops are closed. One problem with this technique is that the interactions may cause the overall system to be unstable even though the local loops are stable. Sufficient conditions for closed-loop stability are also given in the previous chapter. We tried the following set of weighting functions for each panel, and the design results are shown in Fig 3.9.

$$\begin{aligned} W_1(s) &= \frac{(s+0.05)^2}{(0.707s+5)^2} \\ W_2(s) &= \frac{20(0.001s+1)}{(1000s+1)} \end{aligned}$$

With decentralized control, the orders of local controllers are $30, 30, 33, 34, 34$, and 30, respectively. Disturbances are rejected over the frequency range $0 - 0.1 rad/sec$. The closed-loop system is not robust at frequencies between 100 and $500 rad/sec$. The reason for this is that we neglected the interconnections between subsystems. By analyzing the transfer function of the plant, we found that the subsystems are strongly interconnected at frequencies between 100 and $300 rad/sec$. Even at low frequencies, the adjacent panels are strongly coupled to each other. In the following section, we proposed a new method for dealing with the problem of strong interconnections in decentralized control.

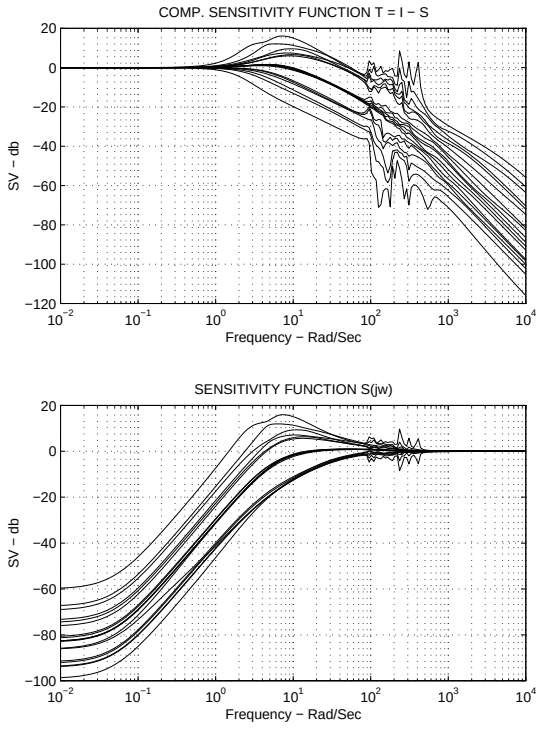

Figure 3.7: Singular value Bode diagram with decentralized control

3.5 Overlapping Decentralized Control Design

In the control of large-scale systems, decentralized control is often the only feasible method for handling the computational complexity; however, subsystems are usually not completely decoupled, as in the case of traffic systems, power systems, chemical processes, and large space structures. They are mostly interconnected in an overlapped fashion, i.e., the subsystems have stronger interconnections with the adjacent subsystems than with the ones that are not adjacent. Ikeda and Siljak came up with an idea that involves expansion of the input, state space, and output to isolate the overlapped subsystems. The control laws are built for the expanded systems and applied to the original system. Overall stability is guaranteed under certain conditions. The fundamental theory behind this idea is the Inclusion Principle [43]; however, to expand the state space of the original system, we need some physical information about the chosen states. In the case of LFSS, input/output models developed using frequency domain system identification techniques are more accurate than the state-space models based on finite element methods. The method of [23] developed for state-space models is modified to be applicable to the input-output models of the LFSS. The controller dynamics are given by:

$$\begin{aligned} \dot{z}_i &= \bar{F}_i z_i + \bar{G}_i \bar{y}_i \\ \bar{u}_i &= \bar{H}_i z_i + \bar{K}_i \bar{y}_i + \bar{v}_i \qquad\qquad i = 1, \cdots, \nu \end{aligned} \tag{3.10}$$

where $z_i \in \mathcal{R}^{n_i}$ is the state of ith sub-controller and $\bar{v}_i \in \mathcal{R}^{m_i + m_{i+1}}$ is the ith local external input. $\bar{F}_i, \bar{G}_i, \bar{H}_i, \bar{K}_i$ are real constant matrices of appropriate size. $\bar{y}_i$ are defined as follows:

$$\bar{y}_i \triangleq \begin{bmatrix} y_i \\ y_{i+1} \end{bmatrix}, \qquad i = 1, \cdots, \nu - 1 \tag{3.11}$$

$$\bar{y}_\nu \triangleq \begin{bmatrix} y_\nu \\ y_1 \end{bmatrix}. \tag{3.12}$$

The control input for each subsystem is obtained as follows:

$$\begin{aligned} u_i &= \frac{1}{2} \begin{bmatrix} \mathbf{0_{m_i \times m_{i-1}}} & \mathbf{I_{m_i}} \end{bmatrix} \cdot \bar{u}_{i-1} + \frac{1}{2} \begin{bmatrix} \mathbf{I_{m_i}} & \mathbf{0_{m_i \times m_{i+1}}} \end{bmatrix} \cdot \bar{u}_i, \quad i = 1, \cdots, \nu - 1 \\ u_\nu &= \frac{1}{2} \begin{bmatrix} \mathbf{0_{m_\nu \times m_{\nu-1}}} & \mathbf{I_{m_\nu}} \end{bmatrix} \cdot \bar{u}_{\nu-1} + \frac{1}{2} \begin{bmatrix} \mathbf{I_{m_\nu}} & \mathbf{0_{m_\nu \times m_1}} \end{bmatrix} \cdot \bar{u}_\nu \end{aligned} \tag{3.13}$$

where $\mathbf{0}$ is a matrix of appropriate size with zero elements and $\mathbf{I}$ is an identity matrix of appropriate size. The solution to the stabilization problem is discussed in Chapter 2. The ASCIE model dynamics has the overlapping characteristics. The overlapping method is applicable. We choose the following set of weight functions for each overlapped subsystem

to perform H_∞ control design. The results are shown in Fig 3.10.

$$\begin{aligned} W_1(s) &= \frac{(s+0.02)^2}{(0.707s+2)^2} \\ W_2(s) &= \frac{20(0.001s+1)}{(1000s+1)} \end{aligned}$$

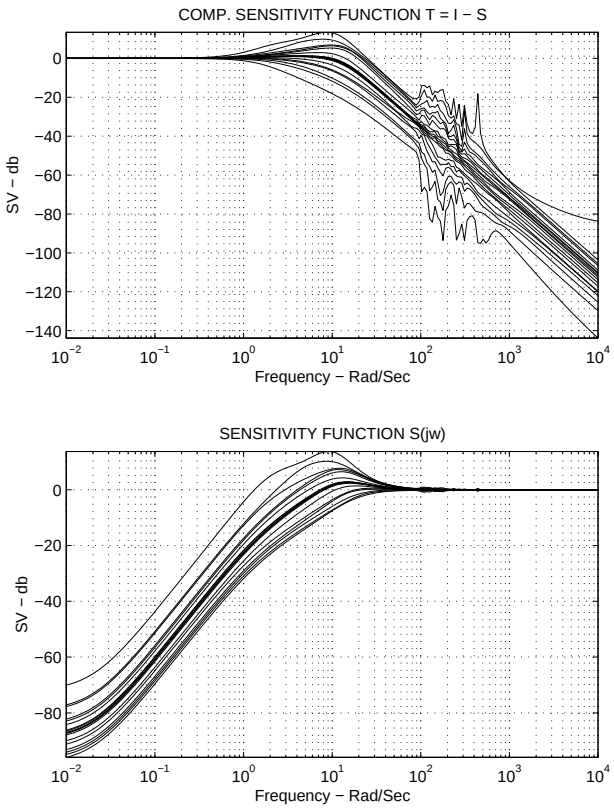

Figure 3.8: Singular value Bode diagram with overlapping decentralized control

The orders of the local controllers are $58, 60, 58, 59, 57$, and 56, respectively. The performance requirements are met as seen in Fig 3.10, and computation with parallel processing is faster than that of the central controller. However, the performance of the centralized scheme is better than that of the overlapping method when we consider the ability of rejecting disturbance in the frequency range of $0 - 1 rad/sec$. In the overlapping approach, the closed-loop bandwidth has been pushed back to suppress the resonance which narrows the frequency range of disturbance rejection.

3.6 Simulation Results

To demonstrate our results, the different control schemes are simulated using the ASCIE model in the time domain. Disturbances are force/torques in nature. The disturbances are

typically quasi-static such as gravity loads, thermally induced loads, actuator bias errors and drifts, steady-state of outside disturbance. The effects of these disturbances are position errors which appear at the edge sensor measurements in the open-loop case. The RMS values of these errors are about 100 microns. the closed-loop system has to achieve a $100:1$ disturbance attenuation which brings the RMS values to about 1 micron. In the simulation, for the sake of simplicity, disturbances with 100 micron magnitude are directly added to the measurements of the edge sensors to emulate the effects of the real disturbances. Therefore, if the closed-loop errors are about 1 micron in magnitude, we can say the $100:1$ disturbance attenuation is achieved. Three different scenarios are simulated here. First, a constant disturbance with magnitude 100 microns is applied to all 18 channels of the telescope. Second, a sinusoidal disturbance with magnitude 100 microns and frequency $0.1rad/sec$ is applied to all 18 channels of the telescope. Finally, a sinusoidal noise with magnitude 1 microns and frequency $400rad/sec$ is added to all the sensor measurements of the telescope. The time domain results are shown in Figs. 3.11-3.13.

In the centralized control case, as shown in Fig 3.11, the closed-loop output of each channel to the disturbance is less than 1 micron after 1 second, which means the disturbance within the frequency range of $0-0.1rad/sec$ has been reduced by 100:1. The closed-loop output of each channel to the sensor noise is less than 0.3 microns which means the loop gain is less than 1 at $400rad/sec$. The closed-loop system is robust at high frequencies (beyond $100rad/sec$), as shown in Fig 3.8.

In the decentralized control case, shown in Fig 3.12, the closed-loop output of each channel to both constant and sinusoidal disturbances of $0.1rad/sec$ is less than 1 micron after 15 seconds, which means the disturbance within the frequency range of $0-0.1rad/sec$ has been reduced by 100:1. However, the sensor noise is not attenuated at $400rad/sec$. Therefore, the closed-loop system is not robust at high frequencies, as shown in Fig 3.9, and the performance requirements are not met.

In the overlapping decentralized control case, shown in Fig 3.13, the closed-loop output of each channel to both constant and sinusoidal disturbances of $0.1rad/sec$ is less than 1 micron after 5 seconds, which means the disturbance within the frequency range of $0-0.1rad/sec$ has been reduced by 100:1. The closed-loop output of each channel to the sensor noise is less than 0.01 micron. Hence the sensor noise is attenuated at $400rad/sec$, which means the loop gain is less than 1 at $400rad/sec$. So the overlapping method can successfully reject the disturbances within the frequency range of $0-0.1rad/sec$. In the meantime, the sensor noise is attenuated and the closed-loop system is robust with respect to modelling uncertainties beyond $100rad/sec$ frequency, as shown in Fig 3.10, in contrast to the decentralized control. The lower order of the local controllers makes computation faster with parallel processing compared to the centralized control.

Centralized, decentralized and overlapping approaches based on H_∞ robust control de-

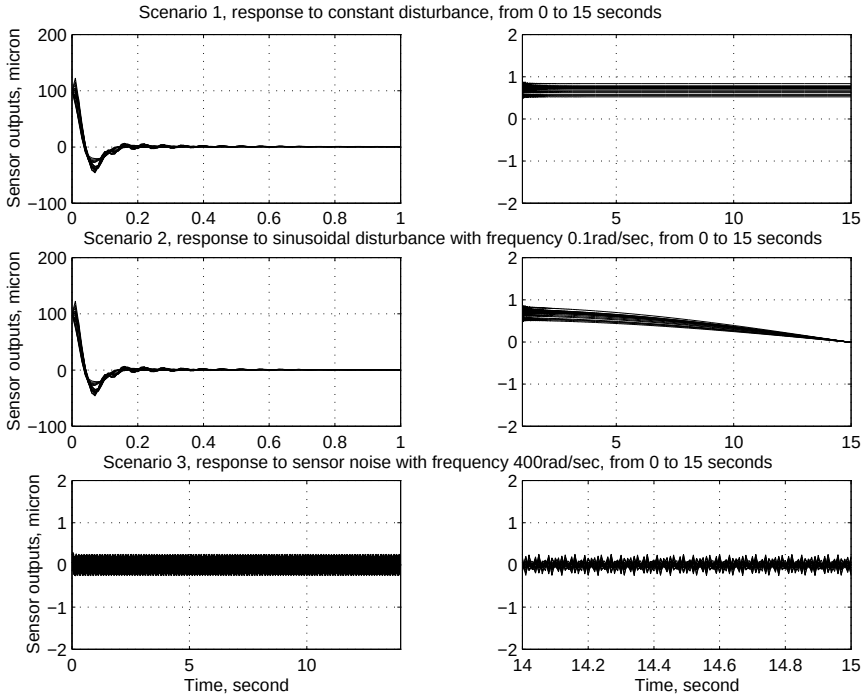

Figure 3.9: Responses of closed-loop system with centralized control

sign are used to develop control laws for a validated model of a large segmented telescope. The centralized control design meets all the performance and robustness requirements but is difficult to implement in real time due to the high order of the controller. The decentralized control design requires less computational effort and enables parallel implementation in real time. However, its performance and robustness properties lag behind those of the centralized scheme. A compromise between the centralized and decentralized approaches is the overlapping control design, which has been shown to meet the performance and robustness requirements and can be easily implemented in real time using parallel processing.

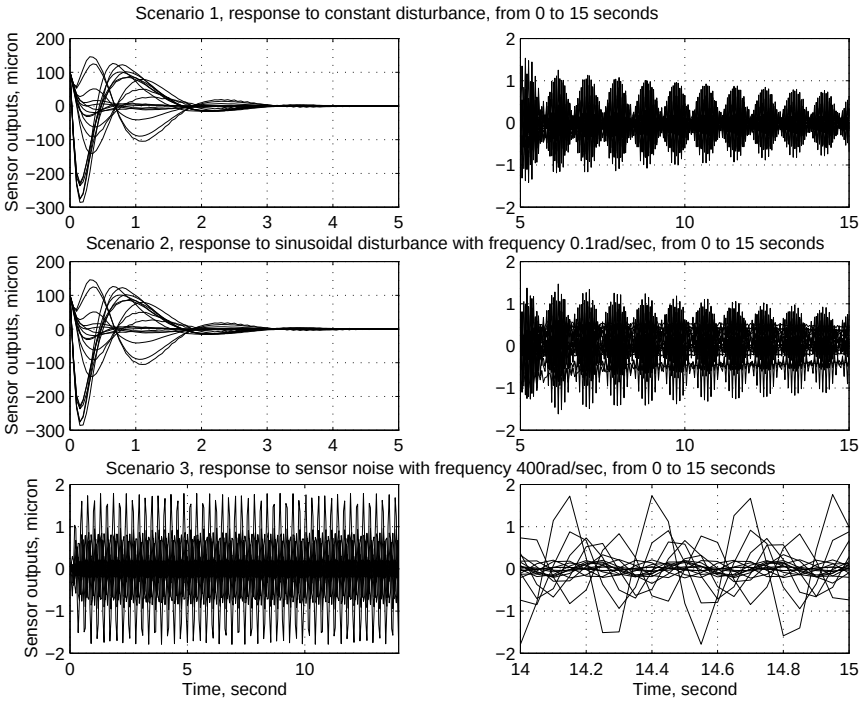

Figure 3.10: Responses of closed-loop system with decentralized control

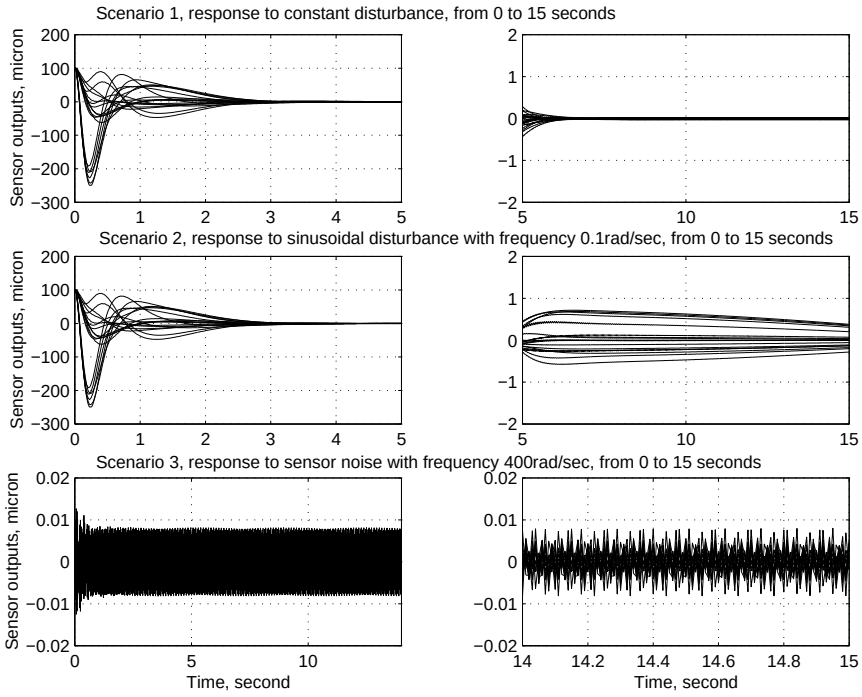

Figure 3.11: Responses of closed-loop system with overlapped decentralized control

Chapter 4

Description Of A Segmented Telescope Test-Bed

The Structures, Pointing And Control Engineering (**SPACE**) laboratory Test-bed is a physical model of a segmented telescope. The test-bed is used to study in an integrated way problems associated with control of large, space-borne, segmented optical telescopes such as modelling, identification, control of multi-input multi-output (MIMO) systems, structural dynamics, control-structure interaction, and disturbance rejection. Real-time control concepts for segmented telescope shape control are being developed and validated over the test-bed. The **SPACE** laboratory is located at California State University, Los Angeles (CSULA), and is funded by NASA. In this chapter we describe the **SPACE** test-bed instrumentation, the features of the equipment and their performance characteristics, hardware interfaces, controller implementation, and overall system architecture.

4.1 Introduction

Future space-borne astronomical missions require increasing levels of optical performance and accuracy, which necessitates larger and larger telescope reflectors. Due to the size, weight and power limitations, as well as the limitations associated with the launch vehicles, the future missions would necessarily employ segmented reflectors instead of monolithic ones that are cast from a single piece of glass. The challenge is to make the segmented reflector emulate the optical properties of a monolithic unit. This requires an active segment-alignment control system for shape control, and a precision pointing system for achieving pointing accuracy.

To study the problems associated with real-time control of large space-borne segmented optical systems, NASA has funded an interdisciplinary team of faculty and students from California State University, Los Angeles (CSULA), University of Southern California (USC), California State University, Long Beach (CSULB), and University of California, Berkeley to design and fabricate a test-bed or a model of a segmented telescope at the **SPACE** lab of

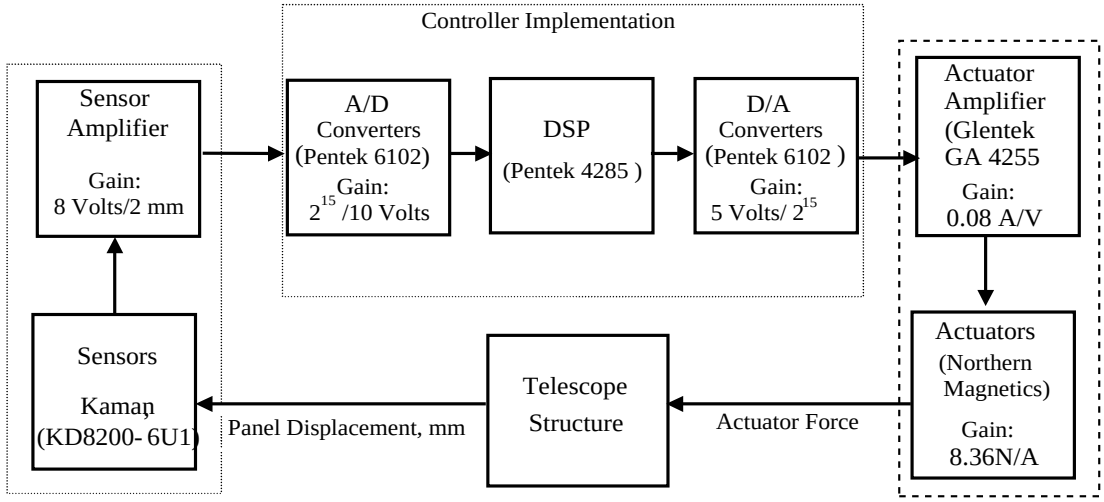

Figure 4.1: **SPACE** Test-bed Hardware Interface Diagram

CSULA.

The work done on the test-bed up to now includes mechanical design, structural analysis, and development of instrumentation and computer architecture, development of system identification techniques and control algorithms, and validation of the control concepts on the test-bed. Continuing work includes development and validation of advanced technologies using high-speed parallel processing for decentralized control, where smaller controllers are developed for individual segments, which are then used together for the shape control of the overall telescope. Future work will include precision pointing, fault identification, controller reconfiguration.

The following sections describe in detail the test-bed instrumentation, the hardware interfaces, and the overall system architecture. The data presented in the paper was taken from hardware manuals and data sheets provided by manufacturers, and earlier reports from the **SPACE** laboratory.

4.2 Hardware Interface and Description of the Structure and Equipment

Fig 4.1 shows a schematic of the hardware interface of the **SPACE** test-bed including the structure, the electronics and the controller implementation. These components are described in detail in the following.

Fig 4.2 shows the features of the telescope structure. The structure of the segmented

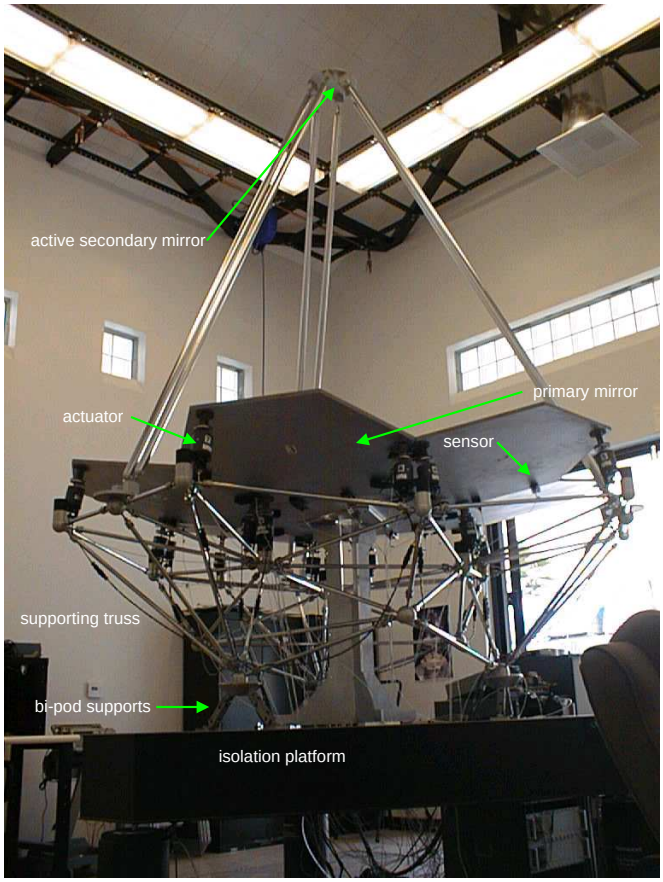

Figure 4.2: View of the Structure Showing the Actuators and Sensors

telescope test bed consists of three main parts: a primary mirror, a secondary mirror, and a truss. The main telescope consists of a 2.4 m focal length Cassegrain optical configuration consisting of a 2.66 m actively controlled primary and an active secondary. The primary mirror is segmented and consists of 7 hexagonal segments. Fig 4.3 shows the dimensions of the structure. Both the primary and the secondary mirrors are completely instrumented with a set of custom designed high-performance actuators, and a set of high bandwidth position sensors. These sensors provide information about the shape of the primary for use in the shape control system, and about the position of the secondary with respect to the focal point of the telescope for use in pointing system.

4.2.1 Primary Mirror

The primary mirror is a 2.61 meters diameter dish supported on a lightweight, flexible truss structure. The optical system emulates a f/2.4 meters Cassegrain telescope. The primary mirror consists of seven hexagonal segments mounted on a lightweight flexible truss struc-

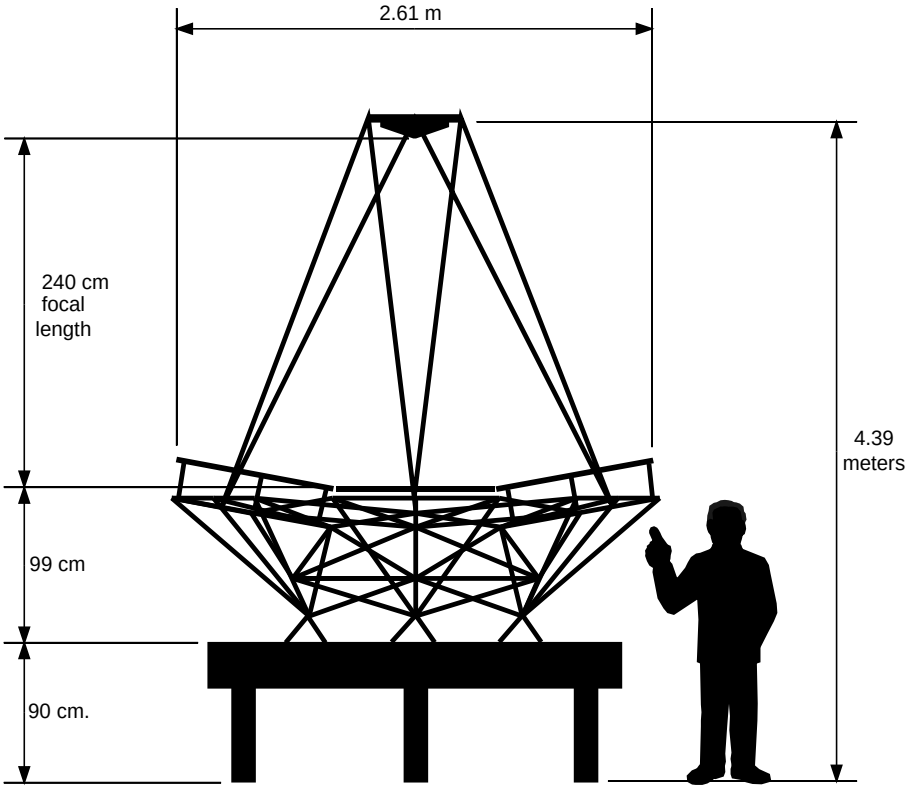

Figure 4.3: Telescope Structure Dimensions

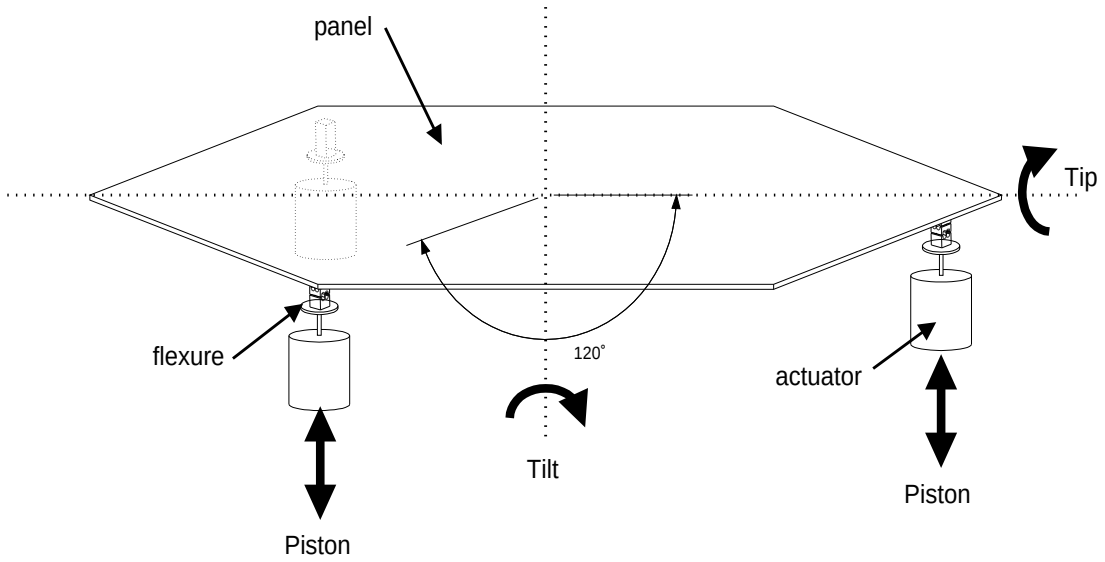

Figure 4.4: Panel Movement in Three Degrees of Freedom

ture. There are 6 peripheral segments mounted around a fixed central segment. On a real segmented telescope the segments would be made of mirrors. On the **SPACE** test-bed, the segments are made of Aluminum with a honeycomb-type core. These segments emulate the mirrors of an optical telescope for the sake of shape control demonstration. The central segment is locked to the isolation table. The six peripheral segments are each actively controlled in three degrees of freedom (DOF's), namely piston, tilt (pitch), and tip (roll) by linear electromagnetic precision actuators. The three degrees of freedom (DOF's) are graphically illustrated in Fig 4.4. Each peripheral segment is attached to the truss at three node points through its three actuators. By actively controlling the position and attitude of the six peripheral segments with reference to the stationary central segment, the actuators maintain the primary mirror shape close to the perfect parabolic surface. The objective of the telescope shape control system is to maintain the shape of the primary mirror to an accuracy of less than 1 micron RMS surface distortion with respect to a perfectly parabolic surface. When the segments are in their nominal positions, the primary mirror surface resembles a parabolic reflector with its focal point located at the secondary mirror.

Twenty-four inductance sensors are used to measure the relative displacements between the segments. There are 2 inductance sensors between every pair of segments, both peripheral and the central segment with one connected to each segment measuring its displacement with respect to the other. Thus there are a total of 24 edge sensors. Collocated with each actuator is a position sensor, 3 per actively controlled segment for a total of 18 collocated sensors.

The primary and secondary mirror segments are both actively controlled, and interact with the actuators, sensors and the supporting truss structure. The control algorithm uses

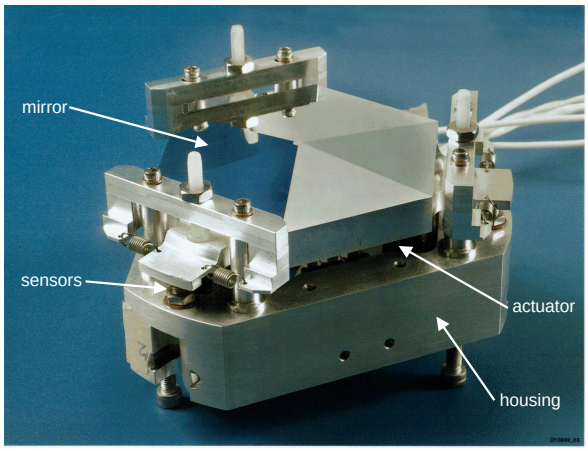

Figure 4.5: Secondary mirror

the outputs of the edge sensors to generate actuator commands for primary mirror shape control. Fig 4.2 is a view of the structure showing the actuators and the sensors mounted below the primary panel. The picture was taken in the **SPACE** laboratory, and shows other elements of the test-bed also, such as the secondary mirror, the supporting truss, and the isolation platform.

4.2.2 Secondary Mirror

The secondary mirror of the test-bed is located 2.4 m above the primary mirror. It consists of an actively controlled mirror whose housing is supported by a secondary truss. The secondary truss consists of six aluminum struts that are attached to the upper part of the primary truss at three points. The mirror is hung from its housing by means of isolation springs

Like the primary mirror segments, the secondary mirror too has three degrees of freedom in the form of a tip, a tilt, and a piston motion. It is equipped with 3 actuators to provide 3-axis active control. The tip and tilt motions provide beam steering by correcting the angular misalignment between the primary and the secondary mirror. The piston motion aligns the mirror to the focal plane of the telescope. It has 3 sensors that provide information about the secondary mirror attitude. The secondary mirror is a six-sided pyramidal aluminum mirror as shown in Fig 4.5

4.2.3 Truss Structure

The structure has been designed to emulate a strong, lightweight truss whose structural-dynamical properties characterize those of a large, flexible, space-borne optical system. Such properties include low frequency modes, high-modal density. The truss is made of thin-wall

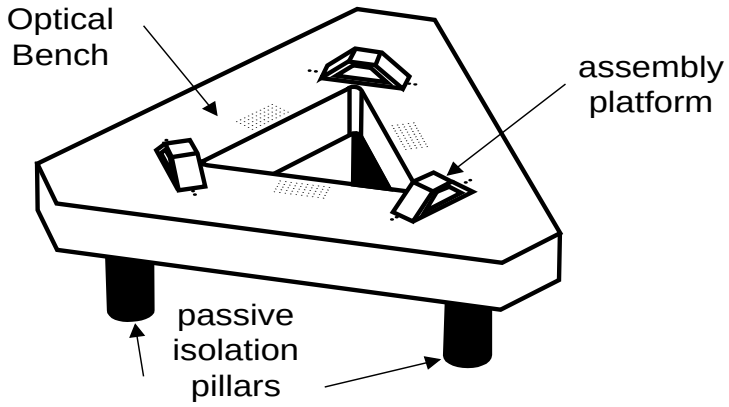

Figure 4.6: Isolation Platform

stainless steel tubing to achieve the highest strength with the lowest mass.

4.2.4 Isolation Platform

The **SPACE** telescope structure is supported on a triangular table that isolates it from any vibrations from the ground. This table is called the isolation platform, and is an I-2000 series Stabilizer and Laminar Flow Isolator made by Newport Company. The platform is made of an aluminum honeycomb core with a stainless steel top skin and bottom skin. It is mounted on three pneumatic cylinders providing a passive isolation system for the structure. Fig 4.6 shows details of the isolation platform.

4.2.5 The Optical Scoring System

In an actual Cassegrain-configuration telescope, the primary mirror collects the incident light and reflects it to a secondary mirror. The secondary mirror will in turn reflect the light to a focal plane where the image is collected. The quality of the reflected image is a measure of the optical performance. For a segmented reflector, a misalignment of either the primary mirror segments or the secondary mirror can cause image quality degradation. Because the **SPACE** test-bed is not a true optical system in the sense that the segments are not actual mirrors, an optical scoring system is used to provide an independent verification of the shape of the primary mirror other than that provided by the edge sensors.

The optical scoring system illustrated in Fig 4.7 works as follows: A Helium-Neon laser source in the center of the primary mirror aims a calibrated laser beam at the secondary mirror. The secondary mirror, which has a six-sided pyramidal design (see Fig 4.5), splits the incoming laser beam into six sub-beams and directs each subbeam to the corresponding peripheral panel. A small mirror, one inch in diameter, mounted on the edge of each pe-

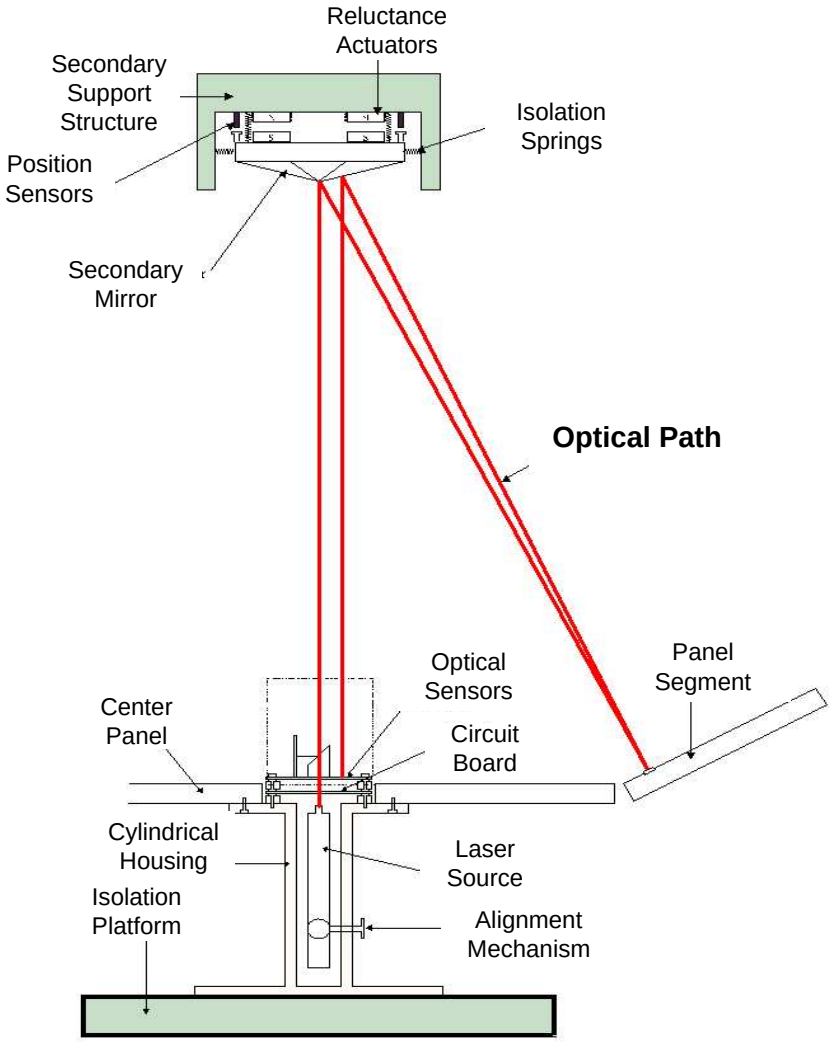

Figure 4.7: Optical Scoring System

ripheral panel, returns each sub-beam back to the secondary mirror, which in turn reflects it back to the center of the primary mirror. The optical sensors located on the central segment detect any deviation of the reflected beam from a reference. The optical scoring system consists of the laser source, the optical module and the small mirrors, and provides a measure of pointing performance. The laser source, the optical sensor module and the center panel are mounted on a tripod shaped housing that is fastened directly to the isolation platform, thus dynamically isolating the optical scoring system from the rest of the structure.

4.2.6 Sensors

The **SPACE** test-bed uses a total of 42 sensors. The sensors are KDM- Series 8200, model 6U1 variable impedance transducers provided by Kaman Instrument Corp. A variable impedance transducer is a device that applies a stimulus (the field produced in a coil by a single frequency AC current) to a conductive target, measures the total opposition to that field by a target, and converts it into an electrical signal proportional to the position of the target relative to the reference. Kaman 8200, 6U1 sensors are low noise, high-resolution inductive transducers with a wide measuring range and frequency spectrum.

The sensors are housed in five racks: there is a master rack and four slave racks, each housing nine channels for a total of 45 channels. Out of these 45 channels, forty-two are used for the 42 sensors used on the **SPACE** test-bed. Of these forty-two position sensors, eighteen sensors are collocated with the actuators to provide information about the relative position of the actuator shaft and it's mounting platform. In addition, twenty-four edge sensors are used to measure the relative displacements of the edges of adjacent segments. Each segment is fitted with edge sensors on the back surface, which measure its edge displacement relative to the nearest segment edge. These sensor measurements are used by the control system to drive the actuators for shape control of the primary mirror.

Fig 4.8 shows the data path for the routing of the sensor data through the test-bed. The edge sensor information indicates the displacement of the peripheral segments compared to a perfect spherical surface, or the shape error. The 24 edge position sensors are used by the control algorithm to generate the actuator commands for segment alignment. The shape control algorithm processes the edge sensor information or the shape error, to obtain the needed axial displacement for the 6 actuated (peripheral) segments relative to the reference (fixed central) segment. The digital signal processor computes the required displacements, and sends force commands to the 18 segment actuators in order to reconfigure the peripheral segments to the desired spherical shape. There is no measurement of the displacement of an individual segment with respect to the support structure but only with respect to the fixed central segment that acts as the reference. The collocated sensors may be used for an independent verification of the associated actuator command.

4.2.7 Segment-Positioning Actuators

The primary mirror shape control is achieved through 18 actuators, three per peripheral segment. In order to achieve precise shape control of the primary mirror, we need high performance segment positioning actuators. The actuators are required to have the following features:

- Extremely low noise level,
- Generate a substantial force over a wide mechanical range,

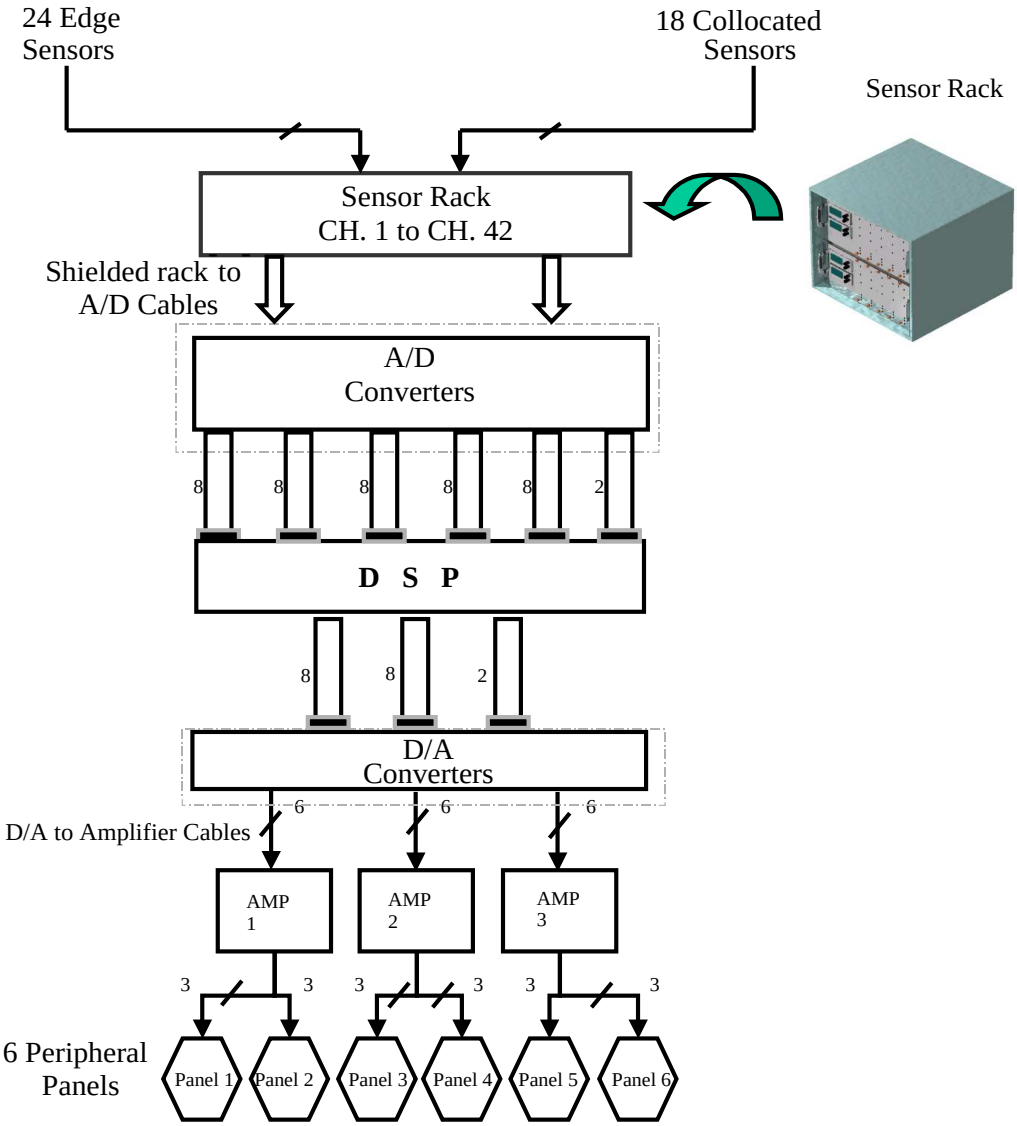

Figure 4.8: Routing of the Sensor Data through the Test-Bed

- Support the weight of a segment in a 1-g field in order to simulate an actual space telescope environment,
- A bandwidth sufficient to accommodate the spectrum of expected disturbance,
- Actuate free of friction,
- Be modular and compact in size, provide an easy interface with the structure,
- Minimize thermal energy dissipation.

In order to meet all of the above requirements, a custom-designed high-performance actuator has been developed for the **SPACE** test-bed by Northern Magnetics. The model ML2-3002-100LB actuators are identical linear electromagnetic force actuators with their own integral control to apply the exact force needed to get the commanded displacements for the overall shape control. The actuator bandwidth is 100 Hz, and the maximum allowable actuator force is 53.576 Newton (equivalent to about 12 pound-force). Custom designed disk flexures are used instead of conventional bearings to eliminate friction. Additionally, an off load spring is used to minimize the amount of actuator force needed when the actuator is mounted below the panel and is supporting the weight of the panel. The off load spring also aids in thermal energy dissipation. The actuators are fitted with collocated position sensors.

On the **SPACE** test-bed there are 18 of these actuators mounted on the primary mirror, 3 per peripheral segment. The actuators are attached below the primary mirror segments as shown in Fig 4.2.

4.2.8 Actuator Amplifiers

The test-bed uses GA4555P Linear Amplifiers made by Glentek. The GA4555P linear amplifier is a modular, high power, high bandwidth servo amplifier that has been designed for use with permanent-magnet actuators. The actuator amplifier receives the output of the DSP board through the D/A converter and serves as the intermediate stage between the output of the digital-to-analog-converter and the actuator.

The GA4555P linear amplifier can be operated in both the velocity and current mode since it is able to accept single-ended as well as differential input signals for amplification. For the **SPACE** test bed, it is used in the current mode.

4.2.9 Digital Signal Processing System

Fig 4.9 shows the overall system architecture of the **SPACE** test-bed. The computer and graphics set-up includes a DSP board, a Dell personal computer (PC) workstation with a Windows NT operating system, disk storage for expanding the memory capacity of the

DSP board, and the graphical display of the Kaman sensor racks. In addition there is an input/output (I/O) unit consisting of A/D and D/A converters.

The **SPACE** test-bed uses Pentek Model 4285, Digital Signal Processor (DSP) Board. The DSP board can be configured with up to eight TMS320C40 (numbered 0-7 or A-H) processors per board for high-speed parallel processing power, hence the name "Octal 'C40 VME board". On the **SPACE** test-bed we are presently using only four TMS320C40 processors (numbered 0,1,4,5 or A, B, E, F). The 4285 DSP board offers communication ports for high-speed connections to the host computer, and other modules such as the A/D and D/A converters.

The DSP is the main computational unit and is responsible for real-time control processing, signal generation, and real-time memory. It is fully programmable from the PC Host. The PC host is used to run the control design and validation experiments on the DSP. The DSP board analyzes the data from sensors after A/D conversion, and generates a digital output to correct for any segment misalignment. This digital output is converted to an equivalent analog output (current), which is amplified and input to the actuators for panel shape correction.

The Pentek model 6102 is a dual Analog-to-Digital (A/D) and Digital-to-Analog (D/A) converter (DAC) package. It is a high-performance 8-channel, 16-bit converter for VME-bus data acquisition, control, and DSP applications. Model 6102 offers differential inputs for the ADC's, 16-bit resolution, and sampling frequencies up to 250 kHz for both ADC's and DAC's .

In order to incorporate the ADC's and DAC's into the system, we need to make sure that the specifications of the sensor's analog output signal match the specifications of the ADC, and likewise match the DAC's output to the actuator's input signal. On the **SPACE** test-bed there are eight dual A/D -D/A boards. Each board provides 8 channels of A/D and D/A conversion. The A/D can receive either single-ended or differential analog inputs, and the D/A produces single-ended analog output. Out of the total 64 channels available, currently 42 A/D channels are being used for converting analog data from the 24 edge and 18 collocated sensors. Out of the 64 D/A channels 18 are being used to convert the actuator commands from the DSP board into analog outputs.

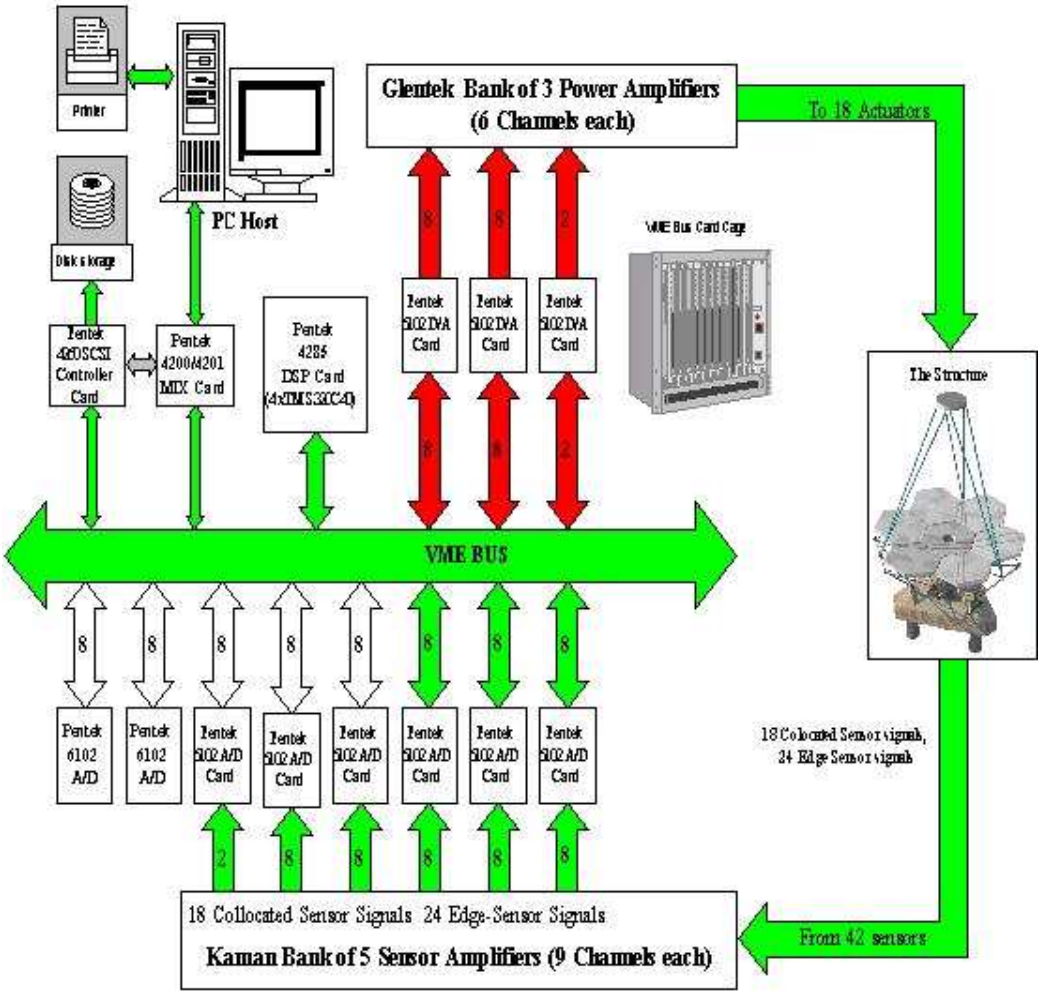

Figure 4.9: **SPACE** Test-Bed Overall System Architecture

Chapter 5

Model Identification of A Segmented Telescope Test Bed

In this chapter a method of frequency domain system identification is presented based on the estimation of a scalar transfer function as a ration of two polynomials. It is a generalization of the well-known SK iteration. The main contribution of this approach is by dividing the frequency domain data into different bands, the resonant frequencies can be located precisely. This approach is successfully applied to the model identification of a large segmented telescope test bed. The state-space model of each segment mirror of the test bed is constructed and proved sufficiently good for the decentralized control design.

5.1 Introduction

Extensive research has been conducted in the active control of large flexible structures [35, 13, 6, 5, 8, 17, 15, 7, 12, 34]. Among those, segmented telescopes are major examples of structures where the size and the complexity issues arise because an array of mirror segments are assembled to perform like one big mirror reflector [33]. Single mirror telescopes would be replaced by large size segmented telescopes that fly a suite of mirrors working in conjunction with each other. Theoretically, such an imaging system would be more robust since as many as two mirrors could break down with no impact to data collection. The difficulty right now is developing the control mechanism for the mirrors to ensure the exact same light wave front arrives simultaneously on each mirror and interpreting the data. To achieve a high control performance on such a structure usually requires an accurate model. Typically such systems are lightly damped and have high-order models with many inputs and outputs as needed. For structure design purposes, the finite element method provides accurate enough models. Then static and dynamic tests on the structure can be performed to refine the finite element model, for instance, tuning the structural modes and mode-shape, etc. However, the model developed from this approach may not be accurate enough for the control system design.

In practice, models identified directly from experimental data are more preferred by control engineers. Even though there are a great number of time-domain identification techniques in the literature [36], if the excitation of the system is well designed, e.g., periodic input or frequency-sweeping sine, estimation of transfer function by fitting complex frequency data has several advantages over the model synthesis in time domain as pointed in [40]: a) Easy noise reduction b) Data reduction: a large number of time-domain samples are replaced by a small number of spectral lines c) When using a discrete Fourier transform (DFT) to calculate the spectra, the frequency-domain noise is asymptotically (number of time domain samples going to infinity) complex distributed d) No initial state estimation of the system needed e) Model validation: Using periodic excitations one has very good point estimates of the frequency response function f) Easy to combine data from different experiments. The problem of fitting a transfer function or transfer function matrix has been addressed by many authors [18, 15]. Based on Least Square (LS) estimation techniques, as used by Levi in [32] and further refined by Sanathanan and Koerner in [42], multivariable frequency domain curve fitting has been formulated in the literature [6, 34]. Motivated by Bayard's multi-band approach [5], this paper presents a method that is a generation of the SK approach. As being used by many people, it is often necessary to express a scalar transfer function of a linear time invariant system as a ratio of two frequency dependent polynomials, namely,

$$G(j\omega) = \frac{N(j\omega)}{D(j\omega)} = \frac{b_{n-1}(j\omega)^{n-1} + \cdots + b_1(j\omega) + b_0}{(j\omega)^n + a_{n-1}(j\omega)^{n-1} + \cdots + a_1(j\omega) + a_0}$$

assuming $G(s)$ is a strictly proper transfer function. Based on the Least Square (LS) estimation technique, Levy [32] formulated a linear LS method by minimizing the following error,

$$Q = \sum_{k=1}^{N} |G(j\omega_k)D(j\omega_k) - N(j\omega_k)|^2$$

However, the above method is naturally a weighted LS method where the data at high frequencies have more influence on the fitting error. It has serious deficiencies as pointed out by Sanathanan and Koerner in [42]. First, if the transfer function has to be determined for frequencies extending several decades, the data at low frequencies have very little influence. Hence, a good fit cannot be obtained at lower frequencies. Second, if $G(s)$ has poles in the complex s-plane such that $|D(j\omega)|^2$ could vary widely throughout the experimental points, large errors would be introduced. To remove the weighting in Q, Sanathanan and Koerner proposed an iterative procedure which minimizes the following error in the Kth iteration,

$$Q_K = \sum_{k=1}^{N} \left| \frac{G(j\omega_k)D_K(j\omega_k) - N_K(j\omega_k)}{D_{K-1}(j\omega)} \right|^2$$

The subscript K denotes the iteration number. Again in each iteration, minimizing Q_K with

respect to the coefficients of $D(s)$ and $N(s)$ involves only linear equations. Iteration starts with $D_0(s) = 1$ which is Levy's method. Here we proposed a different method. By dividing the frequency domain data into different bands, we try to fit the complex data in a certain band by taking the previous fitting results into account as shown in Fig 5.1. By doing this, the resonant frequencies can be well isolated and a good fit can be obtained with a wide frequency range. In section 2, we formulate the error function and present the algorithm. In section 3, an example is given to demonstrate the effectiveness of this proposed method. In section 4, we applied this method to a segmented telescope test bed for the purpose of a decentralized control design. By isolating each segment mirror as an independent subsystem, we construct a state-space model for each segment successfully.

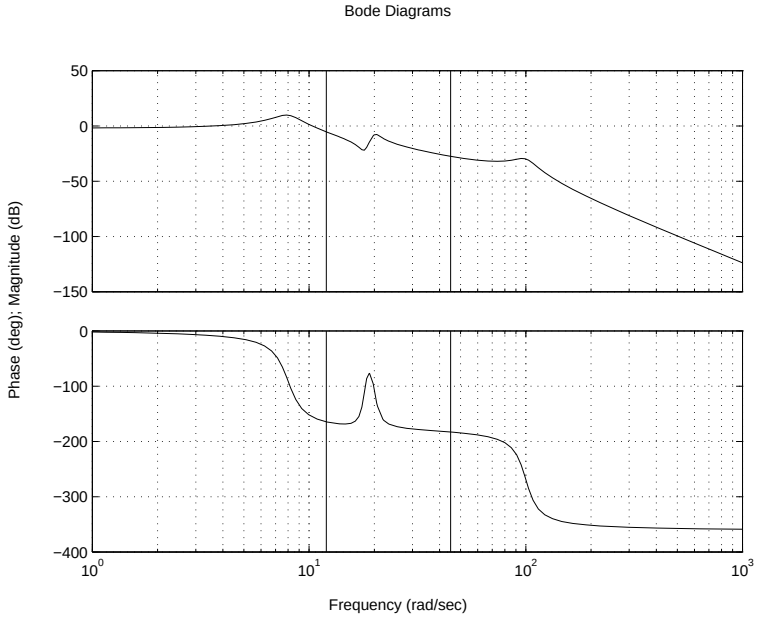

Figure 5.1: Sections of complex frequency domain data

5.2 Problem Formulation and Algorithm

In this section we formulate the fitting error for the least square curve fitting. As shown in Fig 5.1, the data are divided into a number of sections accordingly based of the experimental data. In the first band, we fit the data with an estimated transfer function $G_1(s) = N_1(s)/D_1(s)$ within the frequency range of $[\omega_0, \omega_1]$ using Levy's method. The error is formulated as the following

$$Q_1 = \sum_{k=1}^{n_1} |G(j\omega_k)D_1(j\omega_k) - N_1(j\omega_k)|^2$$

where $G(j\omega)$ is the experimental data and n_1 is the length of the data within the band. The minimization of the above error can be achieved by solving the following set of linear algebraic equations of the form

$$\begin{aligned}
G(j\omega_1)\left[(j\omega_1)^n + a_{n-1}(j\omega_1)^{n-1} + \cdots + a_1(j\omega_1) + a_0\right] \\
- \left[b_{n-1}(j\omega_1)^{n-1} + \cdots + b_1(j\omega_1) + b_0\right] = 0 \\
G(j\omega_2)\left[(j\omega_2)^n + a_{n-1}(j\omega_2)^{n-1} + \cdots + a_1(j\omega_2) + a_0\right] \\
- \left[b_{n-1}(j\omega_2)^{n-1} + \cdots + b_1(j\omega_2) + b_0\right] = 0 \\
\vdots \\
G(j\omega_{n_1})\left[(j\omega_{n_1})^n + a_{n-1}(j\omega_{n_1})^{n-1} + \cdots + a_1(j\omega_{n_1}) + a_0\right] \\
- \left[b_{n-1}(j\omega_{n_1})^{n-1} + \cdots + b_1(j\omega_{n_1}) + b_0\right] = 0
\end{aligned}$$

The above equations can be rewritten as the following form

$$A_1 \cdot x_1 = b_1$$

where,

$$A_1 = \begin{pmatrix}
G(j\omega_1)(j\omega_1)^{n-1} & \cdots & G(j\omega_1)(j\omega_1) & G(j\omega_1 & -(j\omega_1)^{n-1} & \cdots & -(j\omega_1 & -1 \\
G(j\omega_2)(j\omega_2)^{n-1} & \cdots & G(j\omega_2)(j\omega_2) & G(j\omega_2 & -(j\omega_2)^{n-1} & \cdots & -(j\omega_2 & -1 \\
\vdots & \vdots & \vdots & \vdots & \vdots & \vdots & \vdots & \vdots \\
G(j\omega_{n_1})(j\omega_{n_1})^{n-1} & \cdots & G(j\omega_{n_1})(j\omega_{n_1}) & G(j\omega_{n_1} & -(j\omega_{n_1})^{n-1} & \cdots & -(j\omega_{n_1} & -1
\end{pmatrix}$$

$$x_1 = \begin{bmatrix} a_{n-1} & \cdots & a_1 & a_0 & b_{n-1} & \cdots & b_1 & b_0 \end{bmatrix}^T$$

$$b_1 = \begin{bmatrix} -G(j\omega_1)(j\omega_1)^n & -G(j\omega_2)(j\omega_2)^n & \cdots & -G(j\omega_{n_1})(j\omega_{n_1})^n \end{bmatrix}^T$$

In the second data band, we fit the data $G(j\omega)/G_1(j\omega)$ with an estimated transfer function $G_2(s) = N_2(s)/D_2(s)$ within the frequency range of $[\omega_1, \omega_2]$ by minimizing the following error

$$Q_2 = \sum_{k=n_1+1}^{n_2} \left| \frac{\frac{G(j\omega_k)}{G_1(j\omega_k)} D_2(j\omega_k) - N_2(j\omega_k)}{D_1(j\omega)} \right|^2$$

where $n_2 - n_1$ is the length of the data within the second band. Notice that, by introducing $D_1(s)$ into the above error, deficiencies of Levy's approach are eliminated while no iteration is required compared to the SK iteration.

In general the fitting error in data section is formulated as the following

$$Q_L = \sum_{k=n_{L-1}+1}^{n_L} \left| \frac{\frac{G(j\omega_k)}{\prod_i^{L-1} G_i(j\omega_k)} D_L(j\omega_k) - N_L(j\omega_k)}{D_{L-1}(j\omega)} \right|^2$$

And the coefficients of the polynomials can be solved through the following algebraic equations in the least square sense

$$A_L \cdot x_L = b_L$$

where,

$$A_L = \begin{pmatrix} \frac{g(j\omega_{n_{L_1}+1})(j\omega_{n_{L-1}+1})^(n-1)}{d(j\omega_{n_{L-1}+1}} & \cdots & \frac{g(j\omega_{n_{L_1}+1})}{d(j\omega_{n_{L-1}+1}} & -\frac{(j\omega_{n_{L-1}+1})^(n-1)}{d(j\omega_{n_{L-1}+1}} & \cdots & \frac{-1}{d(j\omega_{n_{L-1}+1})} \\ \frac{g(j\omega_{n_{L_1}+2})(j\omega_{n_{L-1}+2})^(n-1)}{d(j\omega_{n_{L-1}+2}} & \cdots & \frac{g(j\omega_{n_{L_1}+2})}{d(j\omega_{n_{L-1}+2}} & -\frac{(j\omega_{n_{L-1}+2})^(n-1)}{d(j\omega_{n_{L-1}+2}} & \cdots & \frac{-1}{d(j\omega_{n_{L-1}+2})} \\ \vdots & \vdots & \vdots & \vdots & \vdots & \vdots \\ \frac{g(j\omega_{n_L})(j\omega_{n_L})^(n-1)}{d(j\omega_{n_L}} & \cdots & \frac{g(j\omega_{n_L})}{d(j\omega_{n_L}} & -\frac{(j\omega_{n_L})^(n-1)}{d(j\omega_{n_L}} & \cdots & \frac{-1}{d(j\omega_{n_L})} \end{pmatrix}$$

$$x_L = \begin{bmatrix} a_{n-1} & \cdots & a_1 & a_0 & b_{n-1} & \cdots & b_1 & b_0 \end{bmatrix}^T$$

$$b_L = \begin{bmatrix} -\frac{g(j\omega_{n_{L_1}+1})(j\omega_{n_{L-1}+1})^n}{d(j\omega_{n_{L-1}+1})} & -\frac{g(j\omega_{n_{L_1}+2})(j\omega_{n_{L-1}+2})^n}{d(j\omega_{n_{L-1}+2})} & \cdots & -\frac{g(j\omega_{n_L}(j\omega_{n_L})^n}{d(j\omega_{n_L})} \end{bmatrix}^T$$

$$d(j\omega_k) \triangleq \prod_{i=1}^{L-1} D_i(j\omega_k), \qquad k = n_{L-1}+1, \cdots, n_L$$

$$g(j\omega_k) \triangleq \frac{G(j\omega_k}{\prod_{i=1}^{L-1} G_i(j\omega_k)}, \qquad k = n_{L-1}+1, \cdots, n_L$$

5.3 Simulation Results

A numerical example is given in this section to illustrate the performance of the proposed algorithm. The transfer function of a **SISO LTI** system is given as

$$G(j\omega) = \frac{N(j\omega)}{D(j\omega)} = \frac{b_2(j\omega)^2 + b_1(j\omega) + b_0}{(j\omega)^6 + a_5(j\omega)^5 + \cdots + a_1(j\omega) + a_0}$$

where,

$$b_0 = 207360000, \;\; b_1 = 960000, \;\; b_2 = 640000$$
$$a_0 = 256000000, \;\; a_1 = 9792000, \;\; a_2 = 4724160$$
$$a_3 = 50288, \;\; a_4 = 10548, \;\; a_5 = 24, \;\; a_6 = 1$$

The Bode diagram is shown in Fig 5.1. In order to measure the transfer function, the

system is excited by a series of random signals and the input/output are recorded to analyze the transfer function. The input signal is a series of random binary signal. The output is corrupted by a random Gaussian noise with 0 mean and variance of 0.0011. The transfer function is estimated and its Bode diagram is plotted in Fig 5.2.

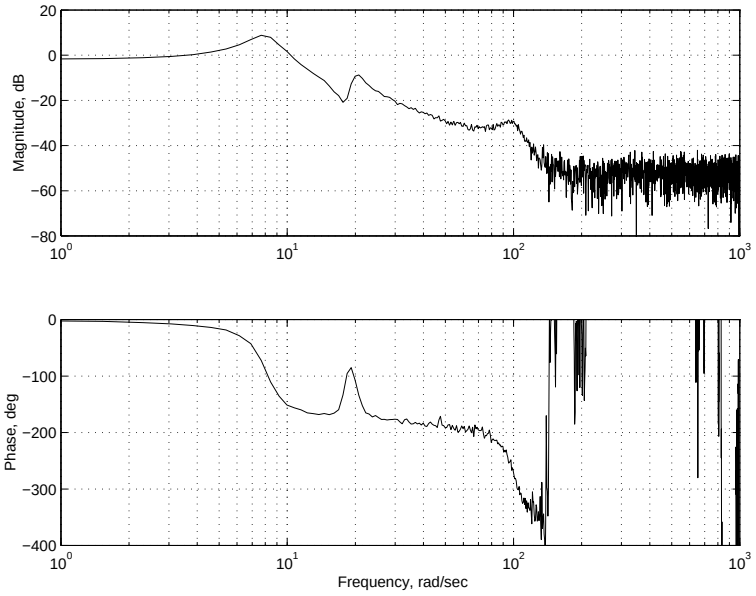

Figure 5.2: Experimental Bode diagram

Here we can see that at high frequencies the output is dominated by the noise, therefore the experimental data is no longer valid. Hence the fitting should be stopped at that point. We cut the data into three bands as shown in Fig 5.1. We fit the first band with $G_1(s)$ and the result is shown in Fig 5.3. In the second band, we try to fit the data with $G_1(s)G_2(s)$ as in Fig 5.4 . Finally, with the data in the third band we fit the data with $G_1(s)G_2(s)G_3(s)$ as in Fig 5.5.

The comparison of poles and zeros are shown below:

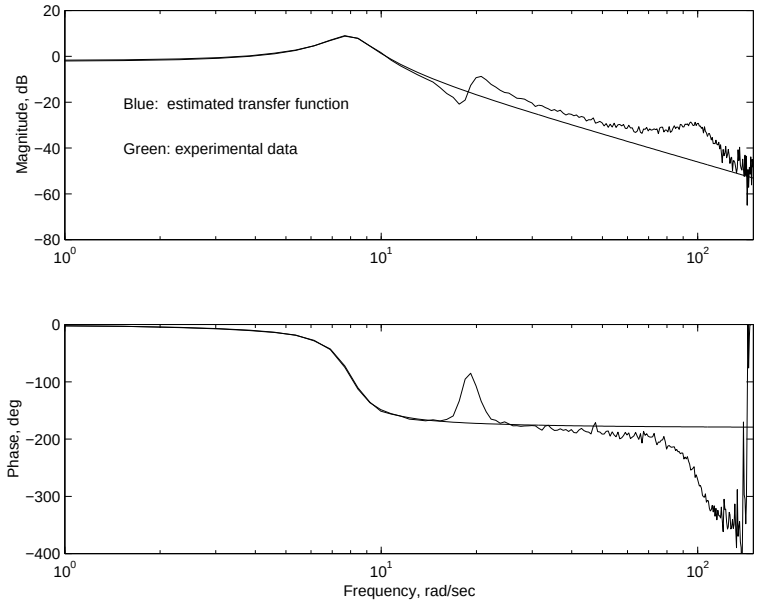

Figure 5.3: Fitting in band 1 with $G_1(s)$

Poles of real model	Poles of estimated model	Zeros of real model	Zeros of estimated model
-10.00 + 99.50j	-9.34 + 99.58j	-0.75 + 17.98j	-0.92 + 18.01j
-10.00 - 99.50j	-9.34 - 99.58j	-0.75 - 17.98j	-0.92 - 18.01j
-1.00 + 19.97j	-1.19 + 20.06j		-242.29
-1.00 - 19.97j	-1.19 - 20.06j		
-1.00 + 7.94j	-1.11 + 7.90j		
-1.00 - 7.94j	-1.11 - 7.90j		
	-169.16		

Table 5.1: Comparison of poles and zeros

5.4 System Identification for SPACE Test Bed

As shown in the Fig 4.2, the primary mirror consists 7 small mirrors. The central mirror is fixed, and the other six peripheral mirrors need to be aligned in a desired shape with the help of control system. Essentially such a large flexible structure makes control system design a very challenging task since the dynamic model is very complicated. In this case decentralized control is a natural option for such a structure [33] by treating each mirror segment as an isolated subsystem and neglecting the interactions between segments. In order to implement the decentralized control, a model identification process has to be carried for each of the six mirror segments. In order to do that, we excite one of the three actuators under that mirror segment at one time, and collect the measurements of the six surrounding edge sensors that can sense the motion of that mirror directly. Here we take mirror segment 1 for example to

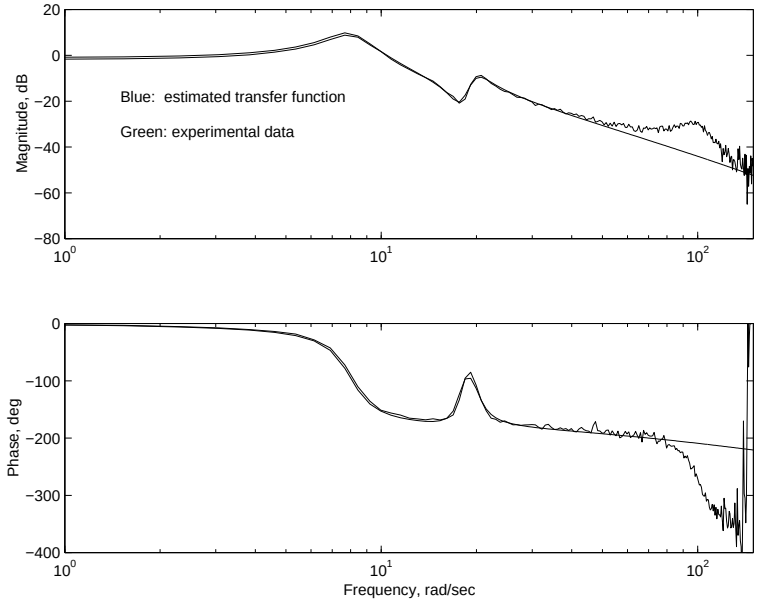

Figure 5.4: Fitting in band 2 with $G_1(s)G_2(s)$

develop the model. A chirp signal with frequency increasing from 1Hz to 20Hz was applied to actuator 1 first, then actuator 2, and 3 accordingly. Each time the outputs of edge sensor 1, 2, 13, 14, 23, and 24 are collected. Then the transfer functions are estimated with the input and output data using Welch's averaged periodogram method. The least square curve fitting method introduced in section 4.2 is used to fit the data, hence the numerator and denominator polynomials are obtained. After all the individual transfer function $\hat{g}_{i,j}(s)$'s are estimated, we can construct the state-space model in the following way.

Let the state space realization of $\hat{g}_{1,1}(s)$ be

$$\begin{aligned} \dot{x}_{1,1} &= A_{1,1} \cdot x_{1,1} + b_{1,1} \cdot u_1 \\ y_1 &= c_{1,1}^T \cdot x_{1,1} \end{aligned} \tag{5.1}$$

In general, the state space realization of $\hat{g}_{i,j}(s)$ be

$$\begin{aligned} \dot{x}_{i,j} &= A_{i,j} \cdot x_{i,j} + b_{i,j} \cdot u_j \\ y_i &= c_{i,j}^T \cdot x_{i,j} \end{aligned} \tag{5.2}$$

where, $i = 1, 2, 13, 14, 23, 24$ and $j = 1, 2, 3$ in this case for mirror segment 1.

The output of edge sensor can be expressed as the following:

$$y_i = g_{i,1}u_1 + g_{i,2}u_2 + g_{i,3}u_3 \tag{5.3}$$

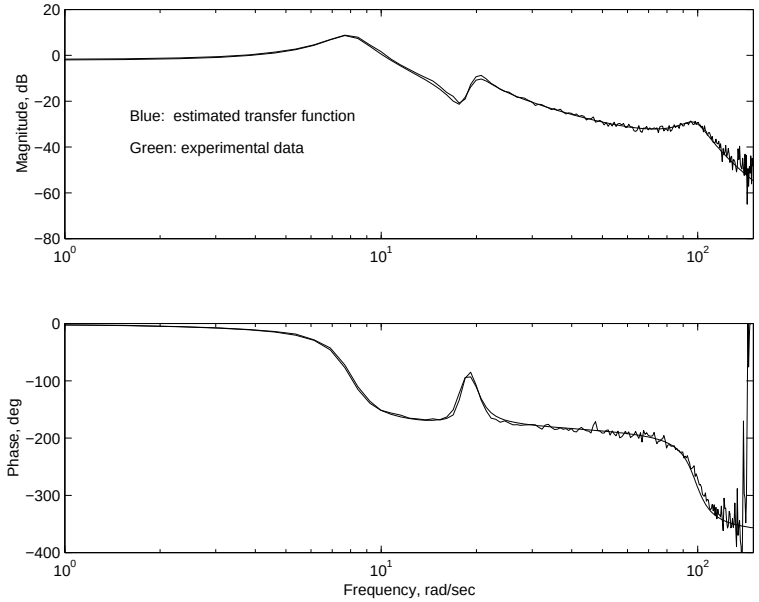

Figure 5.5: Final fitting with $G_1(s)G_2(s)G_3(s)$

The state space realization of the above equation can be expressed as the following:

$$\begin{aligned}\begin{bmatrix} \dot{x}_{i,1} \\ \dot{x}_{i,2} \\ \dot{x}_{i,3} \end{bmatrix} &= \begin{bmatrix} A_{i,1} & 0 & 0 \\ 0 & A_{i,2} & 0 \\ 0 & 0 & A_{i,3} \end{bmatrix} \begin{bmatrix} x_{i,1} \\ x_{i,2} \\ x_{i,3} \end{bmatrix} + \begin{bmatrix} b_{i,1} & 0 & 0 \\ 0 & b_{i,2} & 0 \\ 0 & 0 & b_{i,3} \end{bmatrix} \begin{bmatrix} u_1 \\ u_2 \\ u_3 \end{bmatrix} \\ y_i &= \begin{bmatrix} c_{i,1}^T & c_{i,2}^T & c_{i,3}^T \end{bmatrix} \begin{bmatrix} x_{i,1} \\ x_{i,2} \\ x_{i,3} \end{bmatrix}\end{aligned} \tag{5.4}$$

or,

$$\begin{aligned}\dot{x}_{i,j} &= A_i \cdot x_i + B_i \cdot u \\ y_i &= c_i^T \cdot x_i\end{aligned} \tag{5.5}$$

where,

$$
\begin{aligned}
x_i &\triangleq \begin{bmatrix} x_{i,1} \\ x_{i,2} \\ x_{i,3} \end{bmatrix} \\
u &\triangleq \begin{bmatrix} u_1 \\ u_2 \\ u_3 \end{bmatrix} \\
A_i &\triangleq \begin{bmatrix} A_{i,1} & 0 & 0 \\ 0 & A_{i,2} & 0 \\ 0 & 0 & A_{i,3} \end{bmatrix} \\
B_i &\triangleq \begin{bmatrix} b_{i,1} & 0 & 0 \\ 0 & b_{i,2} & 0 \\ 0 & 0 & b_{i,3} \end{bmatrix} \\
c_i^T &\triangleq \begin{bmatrix} c_{i,1}^T & c_{i,2}^T & c_{i,3}^T \end{bmatrix}
\end{aligned}
\tag{5.6}
$$

Overall, the state space realization of subsystem 1 (mirror segment 1) can be represented as follows

$$
\begin{aligned}
\begin{bmatrix} \dot{x}_1 \\ \dot{x}_2 \\ \dot{x}_{13} \\ \dot{x}_{14} \\ \dot{x}_{23} \\ \dot{x}_{24} \end{bmatrix} &= \begin{bmatrix} A_1 & 0 & 0 & 0 & 0 & 0 \\ 0 & A_2 & 0 & 0 & 0 & 0 \\ 0 & 0 & A_{13} & 0 & 0 & 0 \\ 0 & 0 & 0 & A_{14} & 0 & 0 \\ 0 & 0 & 0 & 0 & A_{23} & 0 \\ 0 & 0 & 0 & 0 & 0 & A_{24} \end{bmatrix} \begin{bmatrix} x_1 \\ x_2 \\ x_{13} \\ x_{14} \\ x_{23} \\ x_{24} \end{bmatrix} \\
&\quad + \begin{bmatrix} B_1 & 0 & 0 & 0 & 0 & 0 \\ 0 & B_2 & 0 & 0 & 0 & 0 \\ 0 & 0 & B_{13} & 0 & 0 & 0 \\ 0 & 0 & 0 & B_{14} & 0 & 0 \\ 0 & 0 & 0 & 0 & B_{23} & 0 \\ 0 & 0 & 0 & 0 & 0 & B_{24} \end{bmatrix} u \\
\begin{bmatrix} y_1 \\ y_2 \\ y_{13} \\ y_{14} \\ y_{23} \\ y_{24} \end{bmatrix} &= \begin{bmatrix} c_1^T & 0 & 0 & 0 & 0 & 0 \\ 0 & c_2^T & 0 & 0 & 0 & 0 \\ 0 & 0 & c_{13}^T & 0 & 0 & 0 \\ 0 & 0 & 0 & c_{14}^T & 0 & 0 \\ 0 & 0 & 0 & 0 & c_{23}^T & 0 \\ 0 & 0 & 0 & 0 & 0 & c_{24}^T \end{bmatrix} \begin{bmatrix} x_1 \\ x_2 \\ x_{13} \\ x_{14} \\ x_{23} \\ x_{24} \end{bmatrix}
\end{aligned}
\tag{5.7}
$$

or,

$$\begin{aligned} \dot{X} &= A \cdot X + B \cdot u \\ y &= C \cdot X \end{aligned} \tag{5.8}$$

where,

$$X \triangleq \begin{bmatrix} x_1 \\ x_2 \\ x_{13} \\ x_{14} \\ x_{23} \\ x_{24} \end{bmatrix}, \qquad y \triangleq \begin{bmatrix} y_1 \\ y_2 \\ y_{13} \\ y_{14} \\ y_{23} \\ y_{24} \end{bmatrix}$$

$$A \triangleq \begin{bmatrix} A_1 & 0 & 0 & 0 & 0 & 0 \\ 0 & A_2 & 0 & 0 & 0 & 0 \\ 0 & 0 & A_{13} & 0 & 0 & 0 \\ 0 & 0 & 0 & A_{14} & 0 & 0 \\ 0 & 0 & 0 & 0 & A_{23} & 0 \\ 0 & 0 & 0 & 0 & 0 & A_{24} \end{bmatrix}$$

$$B \triangleq \begin{bmatrix} B_1 & 0 & 0 & 0 & 0 & 0 \\ 0 & B_2 & 0 & 0 & 0 & 0 \\ 0 & 0 & B_{13} & 0 & 0 & 0 \\ 0 & 0 & 0 & B_{14} & 0 & 0 \\ 0 & 0 & 0 & 0 & B_{23} & 0 \\ 0 & 0 & 0 & 0 & 0 & B_{24} \end{bmatrix} \tag{5.9}$$

$$C \triangleq \begin{bmatrix} c_1^T & 0 & 0 & 0 & 0 & 0 \\ 0 & c_2^T & 0 & 0 & 0 & 0 \\ 0 & 0 & c_{13}^T & 0 & 0 & 0 \\ 0 & 0 & 0 & c_{14}^T & 0 & 0 \\ 0 & 0 & 0 & 0 & c_{23}^T & 0 \\ 0 & 0 & 0 & 0 & 0 & c_{24}^T \end{bmatrix}$$

The above state space realization is balanced in which the controllability and observability Gramians are equal and diagonal. Therefore, each state is just as controllable as it is observable which is essential to the model reduction which works by removing states having little effect on the system's input-output behavior. After the balanced-truncation model reduction, a 48-state space was obtained. By repeating the above procedure for the rest of the mirror segments, we are able to get a decentralized dynamic model of the structure which neglects the interactions between different mirror segments. The singular values of the

estimated model and the experimental data are plotted in Fig 5.6 – Fig 5.11.

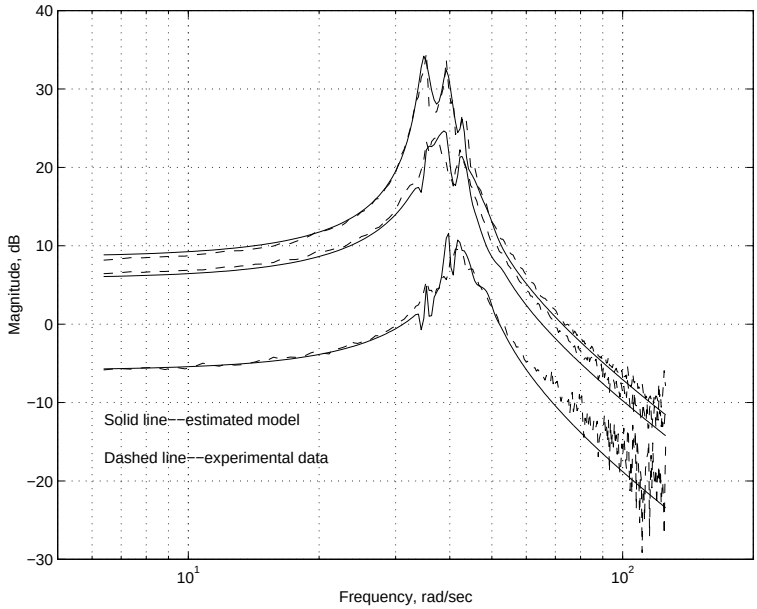

Figure 5.6: Singular value Comparisons for panel 1

*A new **SISO** system identification using frequency domain data is presented in this paper. The method of constructing a **MIMO** state-space model from **SISO** transfer function is also discussed here. This method is applied to the modelling of a segmented telescope test bed structure for the application of decentralized control. The transfer function estimation and the modelling error are also presented. The identified model is validated in the later control system design.*

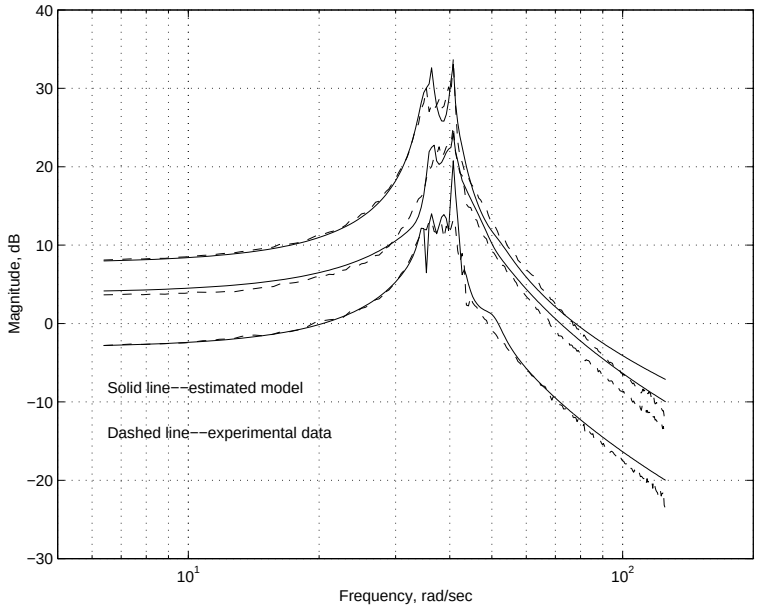

Figure 5.7: Singular value Comparisons for panel 2

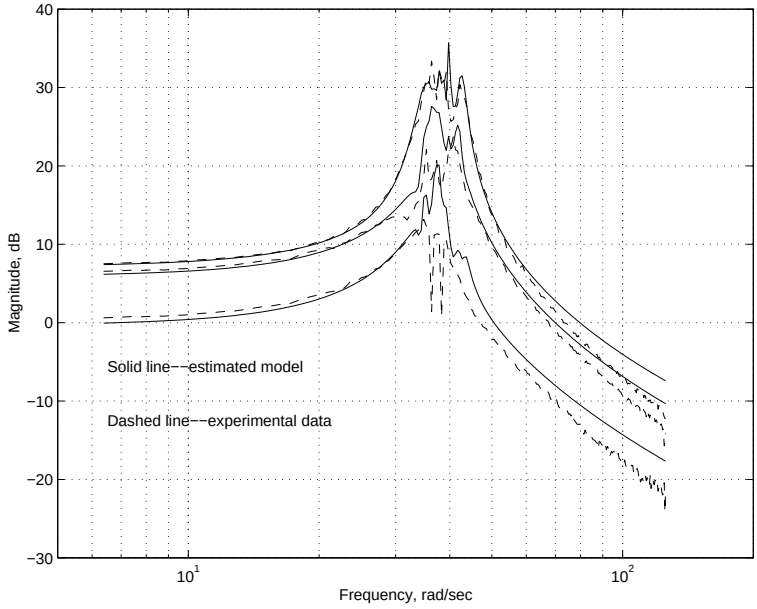

Figure 5.8: Singular value Comparisons for panel 3

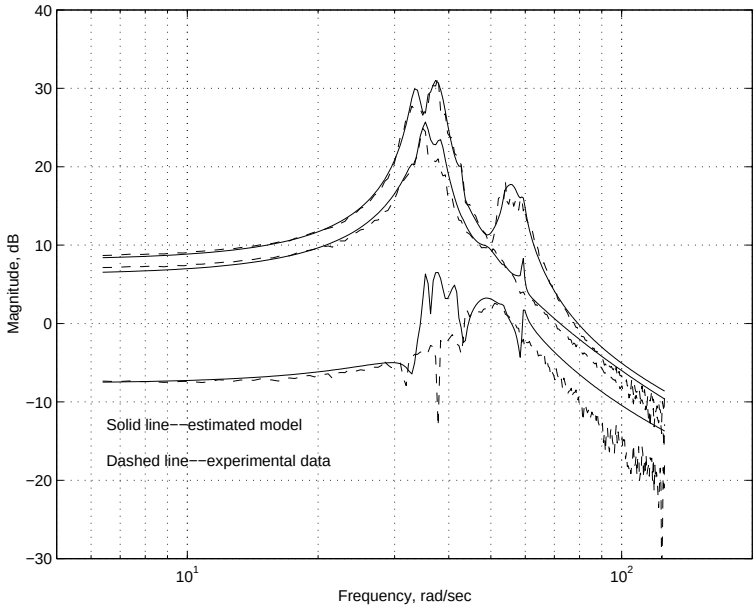

Figure 5.9: Singular value Comparisons for panel 4

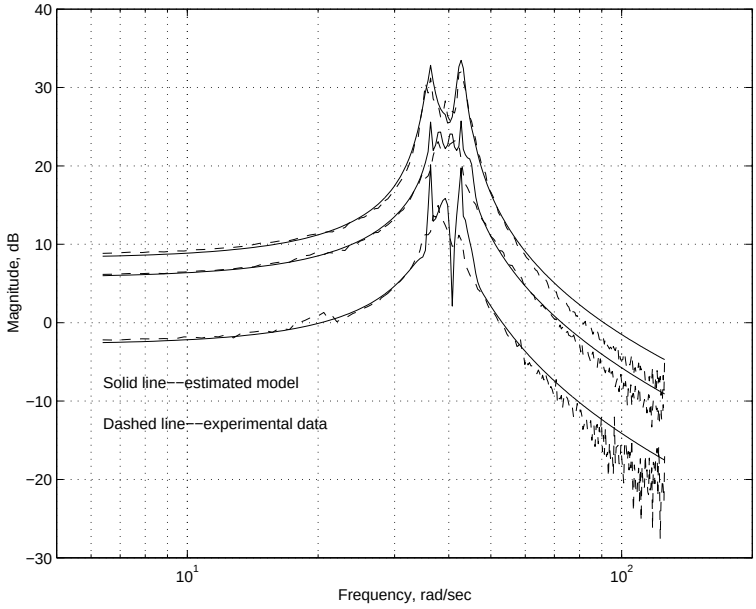

Figure 5.10: Singular value Comparisons for panel 5

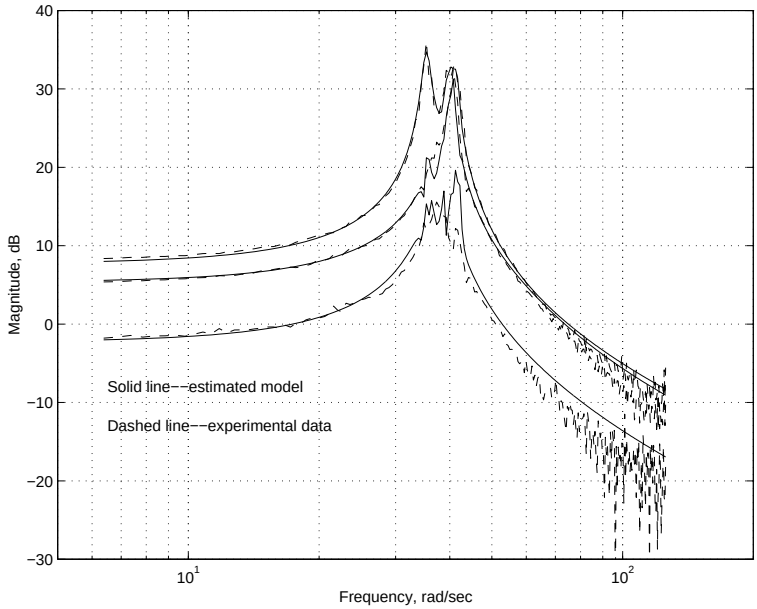

Figure 5.11: Singular value Comparisons for panel 6

Chapter 6

Implementation of Decentralized and Overlapping Decentralized Control Laws For the Segmented Telescope Test Bed

In Chapter 3, different approaches have been investigated for the control design of a large segmented telescope test-bed model and validated through digital simulation. In this Chapter, we apply the two decentralized control approaches to a real telescope structure developed at the Structure Pointing And Control Engineering (SPACE) Laboratory of California State University, Los Angeles. Both the decentralized and the overlapping control algorithms are implemented in real-time in a commercial DSP board. The experimental results proved that the overlapping approach has a better performance than the decentralized approach. Further, by combining the decentralized control with a simple adaptive scheme, the closed-loop performance is greatly improved.

6.1 Control Scheme

6.1.1 Performance Requirements

The segment alignment control system is tasked to achieve the optical quality of a single continuous mirror. Nominally, the segments must form a sphere as shown in Fig 3.3. In the off nominal shape case, the center of each segment will deviate from the nominal tangent point on the sphere. The error has to be within an accuracy of a fraction of the wavelength of light. This optical specification is translated into the requirements for the shape errors to

be within microns at steady state. The shape error is defined as follows:

$$e_i = \sqrt{\frac{y_{i,1}^2 + y_{i,2}^2 + y_{i,3}^2}{3}}, \qquad i = 1, \cdots, 6 \tag{6.1}$$

where, e_i is the *RMS* distortion of mirror segment i; $y_{i,1}, y_{i,2}$ and $y_{i,3}$ are the three virtual sensor outputs of mirror segment i.

The disturbances are typically quasi-static such as gravity loads, thermally induced loads, actuators bias errors and drifts, steady state of outside disturbances. In this work, the disturbance rejection is the main issue of the performance requirements. Therefore, the control system bandwidth is not our primary concern here.

6.1.2 Robust Decentralized and Overlapping Controller Design

The controller design is based on the mixed-sensitivity H_∞ approach of robust control [41]. Assuming r_i and y_i are the reference input and output of the ith mirror segment with the appropriate dimension, and $K_i(s)$ is the H_∞ robust controller for the ith mirror segment in the decentralized control. For the overlapping decentralized control, r_i and y_i are the reference input and output of the ith overlapping subsystem (every two adjacent mirror segments) with the appropriate dimension, $K_i(s)$ is the H_∞ robust controller for the ith overlapping subsystem accordingly. The details about the controller synthesis are discussed in [33]. As an example, the frequency response of decentralized control design is shown in Fig 6.1- 6.6. The frequency response of overlapping decentralized control design is shown in Fig 6.7- 6.12.

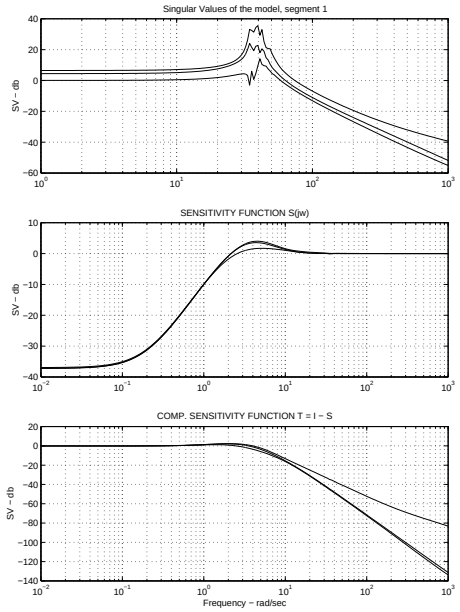

Figure 6.1: Design for segment 1

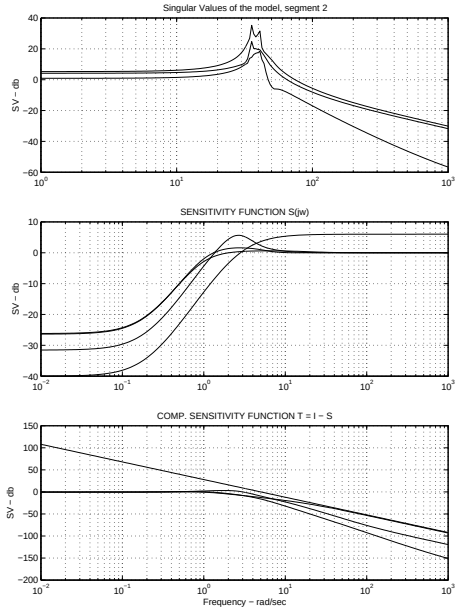

Figure 6.2: Design for segment 2

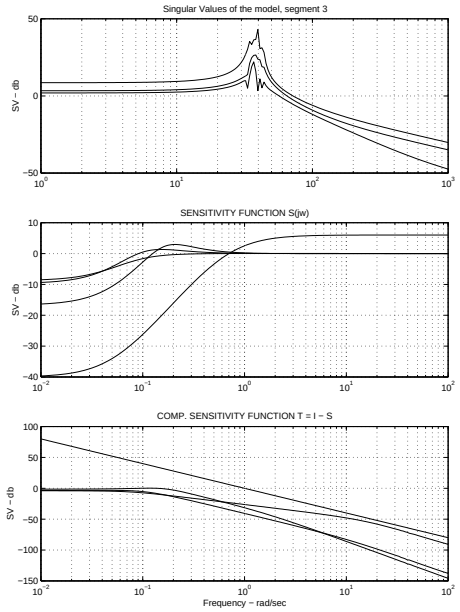

Figure 6.3: Design for segment 3

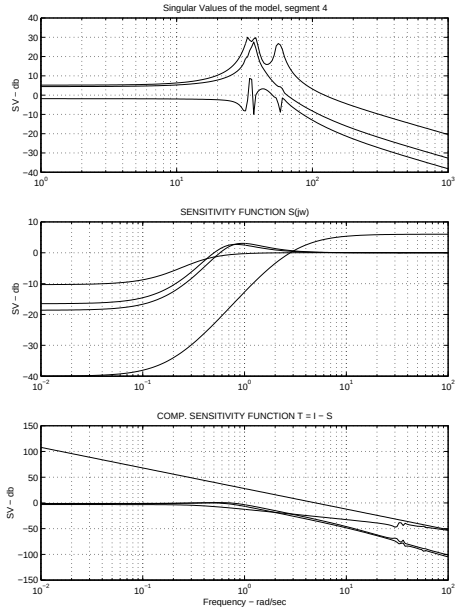

Figure 6.4: Design for segment 4

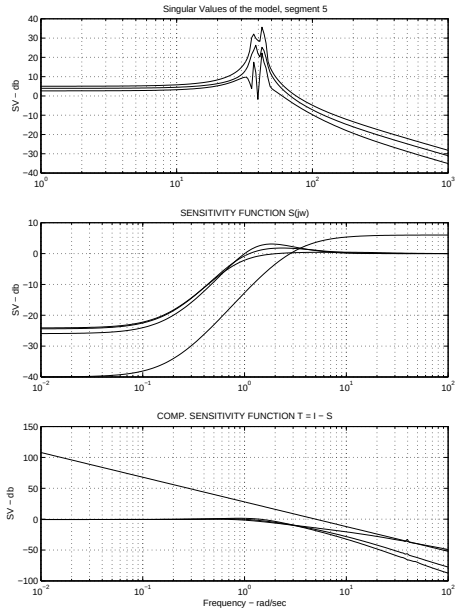

Figure 6.5: Design for segment 5

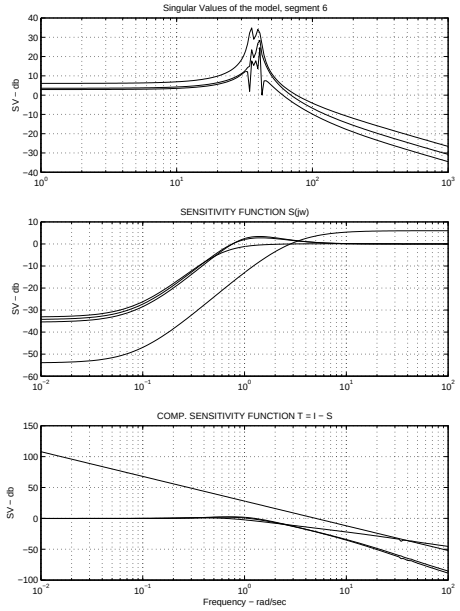

Figure 6.6: Design for segment 6

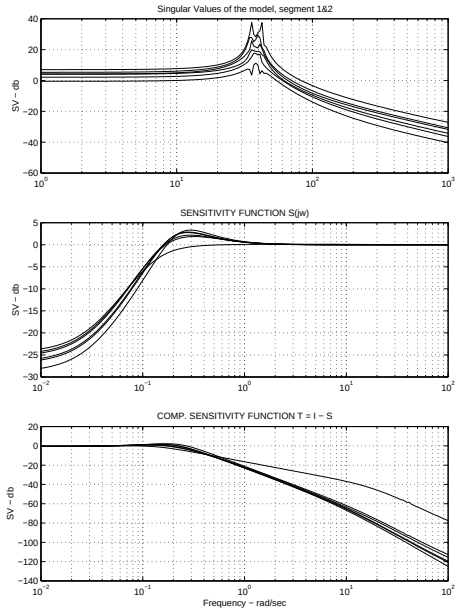

Figure 6.7: Design for segment 1 and 2

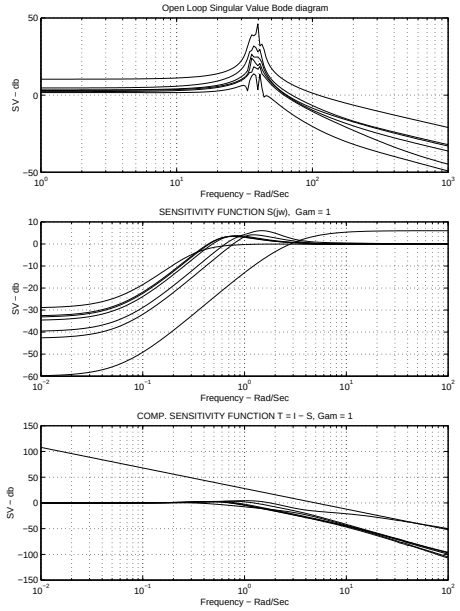

Figure 6.8: Design for segment 2 and 3

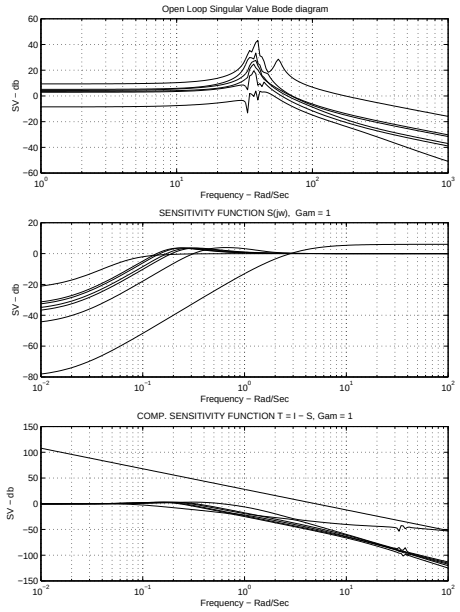

Figure 6.9: Design for segment 3 and 4

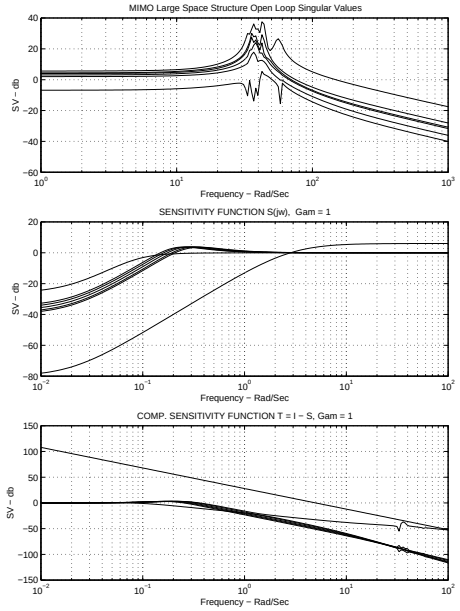

Figure 6.10: Design for segment 4 and 5

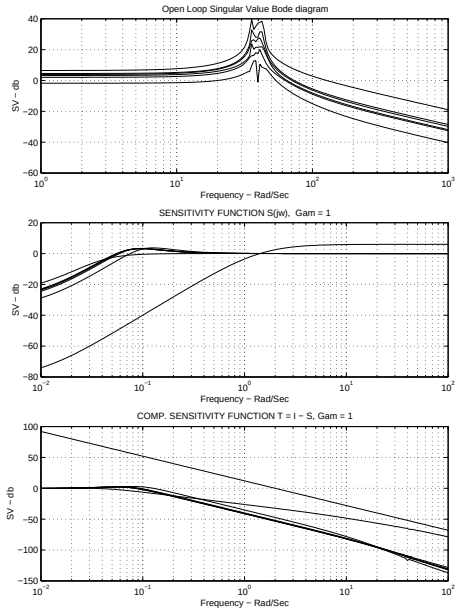

Figure 6.11: Design for segment 5 and 6

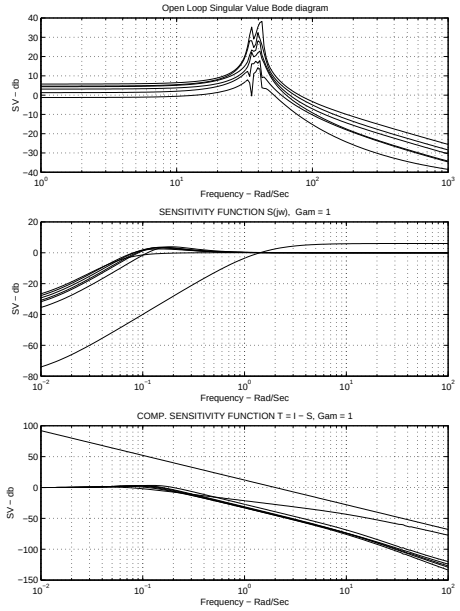

Figure 6.12: Design for segment 6 and 1

6.2 Real-time Implementation

The control laws are implemented in the **SPACE** lab with a **TI TMS320C40** floating-point *DSP*.

There are four processors in the *DSP*. This makes the decentralized control feasible because of the capability of parallel processing with the current hardware architecture. The six controllers were implemented in parallel with a sampling frequency of 320Hz. To introducing the disturbance to the system, a weight is placed on top of each of the six peripheral segment mirrors. The measurements are very noisy since they are corrupted by measurement noise while the structure is still. This can be better understood with Fig 3.4

In Fig 3.4 y, y_m, d and n are the actual virtual displacements, measured virtual displacements, disturbance, and measurement noise respectively. From the block diagram, we have the following expressions:

$$y = S(s)d - T(s)n \tag{6.2}$$

$$y_m = y + n = S(s)d + [1 - T(s)]n = S(s)d + S(s)n \tag{6.3}$$

where, the sensitivity function $S(s)$ and complementary sensitivity function $T(s)$ are defined as follows:

$$S(s) \triangleq [1 - K(s)G(s)]^{-1} \tag{6.4}$$

$$T(s) \triangleq K(s)G(s)[1 - K(s)G(s)]^{-1} \tag{6.5}$$

Since the disturbances are typically quasi-static such as gravity loads, thermally induced loads, actuators bias errors and drifts, steady state of outside disturbances. They will be attenuated if $S(s)$ is small at low frequencies. The noise is high frequency signal, it will be attenuated if $T(s)$ is a low pass filter. Therefore we could make the shape error $y \approx 0$ if $T(s)$ and $S(s)$ are appropriately designed. However, the measurement is corrupted with noise. Even if the shape errors have been greatly attenuated, the measurements will remain as $y_m \approx S(s)n \approx n$. By comparing the standard deviations of the noise in open loop and closed-loop, we found they are almost identical. Therefore we can conclude the quasi-static disturbances are attenuated successfully through the closed-loop decentralized control even though the measurements are noisy. By removing the noise from the primitive measurements with a low-pass filter, we get the shape error of each mirror segment defined in (6.1) as in Fig 6.13. The closed-loop results are shown on Table 6.1.

For the overlapping decentralized control, the results are shown in the Fig 6.14. The closed-loop results are shown on Table 6.2. Compared to the decentralized control, this overlapping approach has significantly improved the performance.

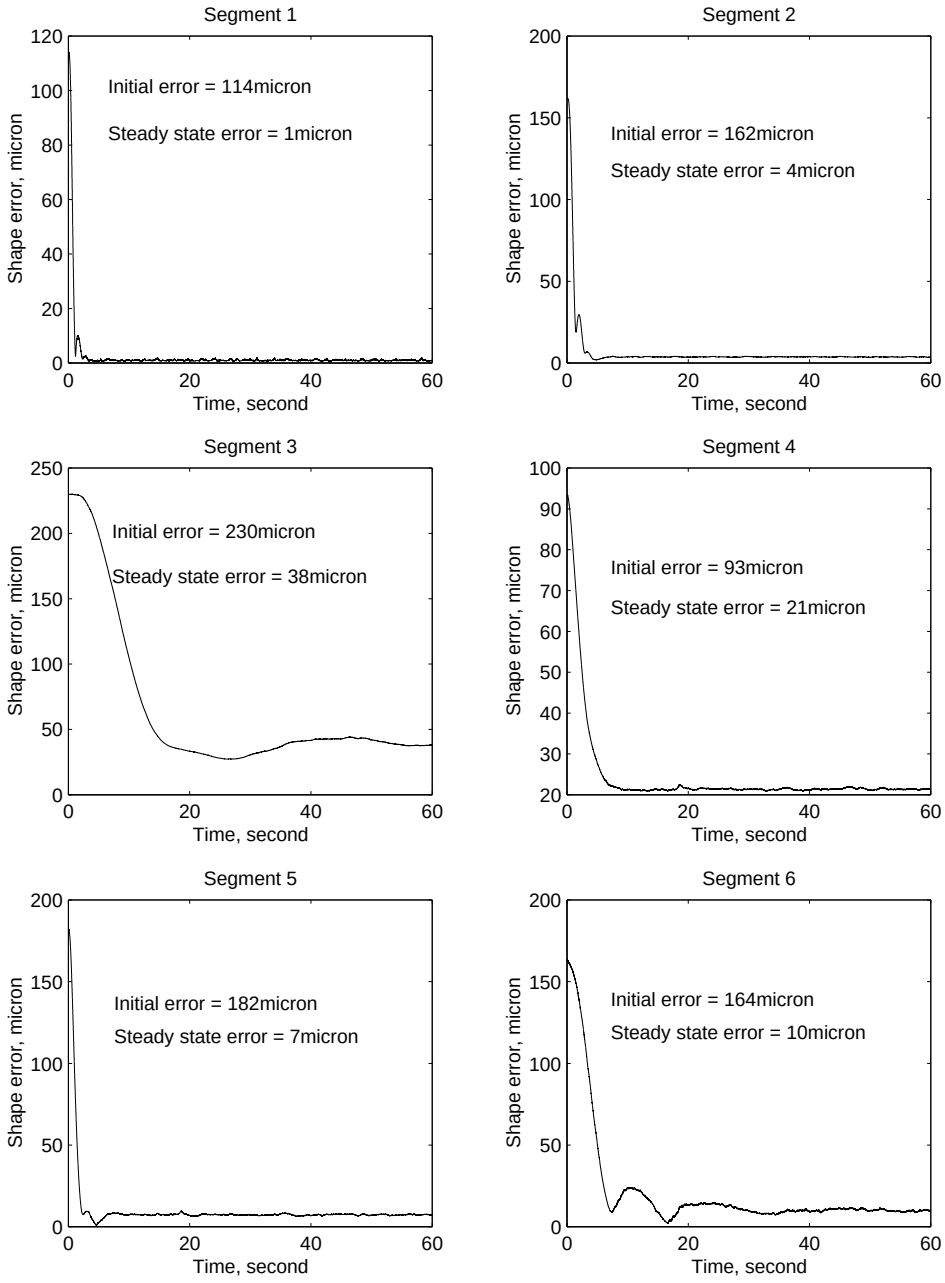

Figure 6.13: Closed-loop real-time results with decentralized control

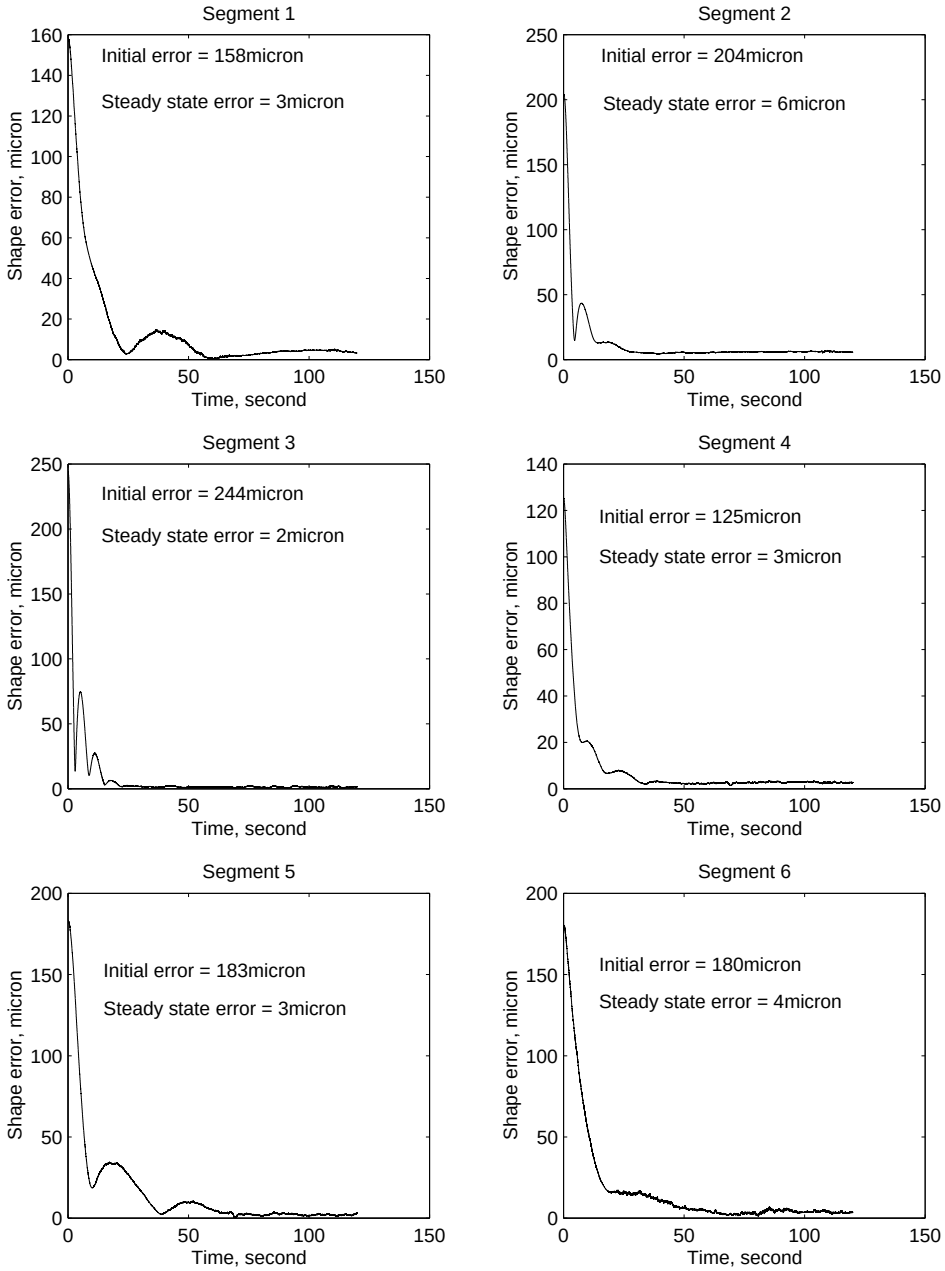

Figure 6.14: Closed-loop real-time results with overlapping decentralized control

Segment	Initial error, micron	RMS error, micron
1	114	1
2	162	4
3	230	38
4	93	21
5	182	7
6	164	10

Table 6.1: Segment shape errors under decentralized control

Segment	Initial error, micron	RMS error, micron
1	158	3
2	204	6
3	244	2
4	125	3
5	183	3
6	180	4

Table 6.2: Segment shape errors under overlapping decentralized control

6.3 Improving the performance with adaptive control

As the structures and their environmental and operational conditions vary within a large range, the adaptive control seems very attractive for the control of large flexible space structures (LFSS). However, most adaptive control methods need some prior knowledge as an upper bound on the order of the plant and also the exact pole-zero excess to guarantee stability of the closed-loop systems, and for the implementation of identifiers or observer-based controllers of the same order as the controlled plant. Since the order of LFSS is very large and unknown, in general, the usual adaptive control techniques cannot be applied unless some prior care is taken to reduce the dimension of the controller. Here we apply a simple adaptive control on top of the decentralized or overlapping decentralized control. This control scheme is proposed in [21] that can stabilize and regulate the output to zero of any plant with arbitrary and unknown order and unknown parameters. The only assumption we made is the existence of a constant output feedback matrix K^* such that the closed-loop transfer function matrix $T(s)$ is **SPR**.

6.3.1 Stability of the adaptive control system

Consider the system $T(s)$ shown in Fig 6.15. In this figure, K is the output feedback gain matrix and $G(s)$ is the transfer function of the plant. It has the following state space

description

$$\begin{aligned} \dot{x} &= Ax + Bu \\ y &= Cx \end{aligned} \tag{6.6}$$

where $A \in \mathcal{R}^{n\times n}$, $B \in \mathcal{R}^{n\times q}$, $C \in \mathcal{R}^{q\times n}$, and $x \in \mathcal{R}^n$, $u \in \mathcal{R}^q$, $y \in \mathcal{R}^r$.

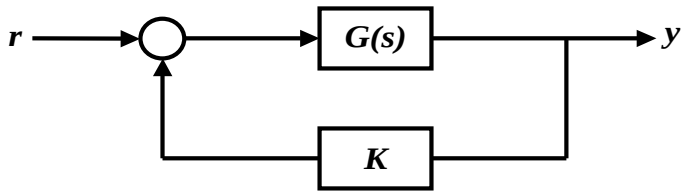

Figure 6.15: Block diagram of the closed-loop system

The closed-loop system of Fig 6.15 can be expressed as

$$\begin{aligned} \dot{x} &= A_k x + Br \\ y &= Cx \end{aligned} \tag{6.7}$$

where $A_k = A - BKC$. The following lemma refers to our main assumption.

Lemma 6.1 (SPR Lemma [31], [1], [2], [26]) *The closed-loop transfer function matrix $T(s) = C(sI - A_k)^{-1}B$ is SPR if and only if there exists a matrix $P = P^T > 0$ such that*

$$PA_k + A_k^T P < 0 \tag{6.8}$$

$$PB = C^T \tag{6.9}$$

We can rewrite (6.7) as

$$\begin{aligned} \dot{x} &= (A - BK^*C)x - B(K - K^*)y \\ y &= Cx \end{aligned} \tag{6.10}$$

or

$$\dot{x} = A^*x - B\tilde{K}y, \qquad y = Cx \tag{6.11}$$

where $A^* = A - BK^*C$, $\tilde{K} = K - K^*$, and $K(t)$ is the estimate of K^* at time t.

Consider the quadratic function

$$V = \frac{x^T P x}{2} + trace(\frac{\tilde{K}^T \Gamma^{-1} \tilde{K}}{2}) \tag{6.12}$$

where P satisfies the SPR Lemma and Γ is an arbitrary positive definite matrix. The time derivative of V along the trajectory of (6.11) is given by

$$\begin{aligned} \dot{V} &= \frac{\dot{x}^T P x + x^T P \dot{x}}{2} + trace(\tilde{K}^T \Gamma^{-1} \dot{\tilde{K}}) \\ &= \frac{x^T (P A^* + A^{*T} P) x}{2} - \frac{y^T \tilde{K}^T B^T P x + x^T P B \tilde{K} y}{2} + trace(\tilde{K}^T \Gamma^{-1} \dot{\tilde{K}}) \end{aligned}$$

According to (6.9), (6.12) can be rewritten as

$$\begin{aligned} \dot{V} &= \frac{x^T (P A^* + A^{*T} P) x}{2} - \frac{y^T \tilde{K}^T C x + x^T C^T \tilde{K}}{2} + trace(\tilde{K}^T \Gamma^{-1} \dot{\tilde{K}}) \\ &= \frac{x^T (P A^* + A^{*T} P) x}{2} - y^T \tilde{K}^T y + trace(\tilde{K}^T \Gamma^{-1} \dot{\tilde{K}}) \\ &= \frac{x^T (P A^* + A^{*T} P) x}{2} + trace(\tilde{K}^T \Gamma^{-1} \dot{\tilde{K}} - \tilde{K}^T y y^T) \end{aligned} \tag{6.13}$$

If we choose

$$\dot{\tilde{K}} = \Gamma y y^T \tag{6.14}$$

we have

$$\dot{V} = \frac{x^T (P A^* + A^{*T} P) x}{2} \tag{6.15}$$

Since V is a quadratic function and $\dot{V} \leq 0$, we conclude that V is a Lyapunov function for the system (6.11), (6.14).

Since V is a nonincreasing function of time, the $lim_{t \to \infty} V(t)$ exists. Therefore, we obtain $x, \tilde{K} \in L_\infty$ and $x \in L_2$. Since $\dot{\tilde{K}} = \Gamma y y^T$ and $y = Cx$ where $x \in L_\infty$, we have $\dot{K} \in L_\infty$. Since $\dot{x} \in L_\infty$ due to $\tilde{K}$, x, $y \in L_\infty$, we conclude from $\dot{x} \in L_\infty$ and $x \in L_2$ [25] that $x(t) \to 0$ as $t \to \infty$.

Hence, $u = -K(t)y$ with $\dot{\tilde{K}} = \Gamma y y^T$ can stabilize any system of any order and drive y, x to zero as long as the assumption of the existence of K^* that makes the closed-loop plant transfer function matrix SPR is satisfied.

6.3.2 Decentralized adaptive control

To accommodate the existing decentralized and overlapping decentralized control scheme, here we apply the decentralized or overlapping decentralized adaptive control on top of the closed-loop. Therefore the plant has been augmented by the decentralized or overlapping control loop as shown on Fig 6.16.

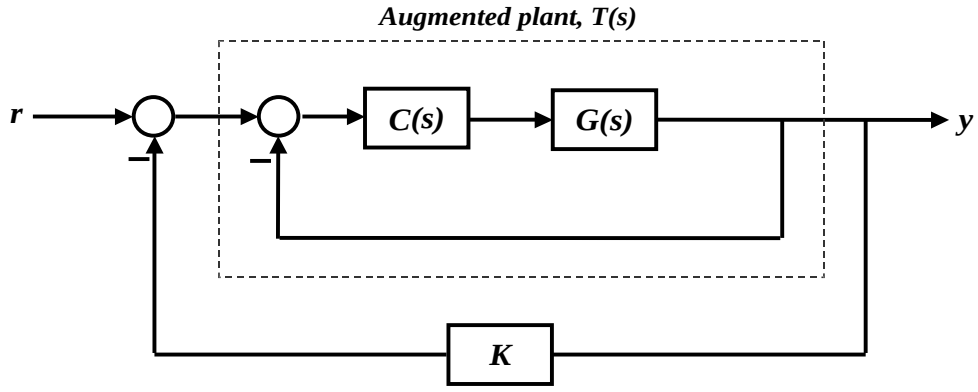

Figure 6.16: Block diagram of decentralized control system with adaptive control

With the decentralized control, the transfer function of the structure can be expressed as

$$\begin{aligned} G(s) &= (I+\Delta)\tilde{G} \\ \Delta &= (G-\tilde{G})\tilde{G}^{-1} \end{aligned} \tag{6.16}$$

where $\tilde{G}$ contains the block diagonal elements of G, as

$$\tilde{G}(s) \triangleq \begin{bmatrix} g_{11}(s) & 0 & \cdots & 0 \\ 0 & g_{22}(s) & \cdots & 0 \\ \vdots & \vdots & \vdots & \vdots \\ 0 & 0 & \cdots & g_{\nu,\nu}(s) \end{bmatrix}. \tag{6.17}$$

We have

$$\begin{aligned} I+GC &= I+(I+\Delta)\tilde{G}C = (I+\tilde{G}C)+\Delta\tilde{G}C \\ &= [I+\Delta\tilde{G}C(I+\tilde{G}C)^{-1}](I+\tilde{G}C) \\ &= (I+\Delta\tilde{T})(I+\tilde{G}C) \end{aligned} \tag{6.18}$$

where,

$$\begin{aligned} \tilde{T} &\triangleq \tilde{G}C(I+\tilde{G}C)^{-1}, \\ \tilde{S} &\triangleq I-\tilde{T}=(I+\tilde{G}C)^{-1} \end{aligned} \tag{6.19}$$

Using (6.17), we have

$$\begin{aligned} T &= GC(I+GC)^{-1} \\ &= GC[(I+\Delta\tilde{T})(I+\tilde{G}C)]^{-1} \\ &= (I+\Delta)\tilde{G}C(I+\tilde{G}C)^{-1}(I+\Delta\tilde{T})^{-1} \\ &= (I+\Delta)(I+\tilde{T}\Delta)^{-1}\tilde{T} \end{aligned} \tag{6.20}$$

Let

$$I+\tilde{\Delta}=(I+\Delta)(I+\tilde{T}\Delta)^{-1}$$

where

$$\begin{aligned} \tilde{\Delta} &\triangleq (I+\Delta)(I+\tilde{T}\Delta)^{-1}-I \\ &= (I+\Delta-I-\tilde{T}\Delta)(I+\tilde{T}\Delta)^{-1} \\ &= \Delta\tilde{S}(I+\tilde{T}\Delta)^{-1} \end{aligned} \tag{6.21}$$

Therefore, the closed-loop transfer function under decentralized or overlapping decentralized control is

$$T=(I+\tilde{\Delta})\tilde{T} \tag{6.22}$$

where,

$$\tilde{T(s)}=\begin{bmatrix} \tilde{T}_1(s) & 0 & \cdots & 0 \\ 0 & \tilde{T}_2(s) & \cdots & 0 \\ \vdots & \vdots & \vdots & \vdots \\ 0 & 0 & \cdots & \tilde{T}_\nu(s) \end{bmatrix}. \tag{6.23}$$

Our assumption is the existence of the constant output feedback matrix $K_i^*, i=1,\cdots,\mu$ such that the closed-loop transfer function matrix $\tilde{T}_iK_i^*[(I+\tilde{T}_iK_i^*)]^{-1}$ is **SPR**. Here the uncertainty term is directly related with the off-diagonal elements (interconnections between segments) and the decentralized controllers $C_i(s)$. In order to make the adaptive control work in the presence of the uncertainty $\tilde{\Delta}$, the gain matrices of the adaptation law (6.14) has to be carefully chosen. Otherwise, the fast adaption will destabilize the overall system.

Segment	Initial error, micron	RMS error, micron
1	240	0
2	278	2
3	256	9
4	120	4
5	270	1
6	314	3

Table 6.3: Segment shape errors under decentralized and adaptive control

Segment	Initial error, micron	RMS error, micron
1	168	4
2	205	6
3	279	1
4	102	2
5	209	2
6	202	4

Table 6.4: Segment shape errors under overlapping decentralized and adaptive control

By implementing the above mentioned adaptive scheme as in Fig 6.16, we get the shape error of each mirror segment as in Fig 6.17. The closed-loop results are shown on the following table.

As we can see from Fig 6.17, the errors are not completely settled down. Given long enough time, the errors will be decreasing more.

For the overlapping decentralized control, the results are shown in the Fig 6.18. The closed-loop results are shown on the following table. Since the overlapping control already achieved good performance, the effect of adaptive control is not as evident as that in the decentralized case.

Decentralized control and overlapping decentralized control laws are developed for the shape control of a large segmented telescope test bed using robust control techniques. The resulted complex control algorithms are easily implemented in parallel with multiple microprocessors. The decentralized control algorithm is relatively simple but cannot meet the performance requirements because the strong dynamic interactions between adjacent segments are ignored. The overlapping decentralized control is a bit complicated but proved to be more effective in meeting the performance requirements by taking into account the dynamic interactions. The performance improvement is demonstrated through the real time experimental results.

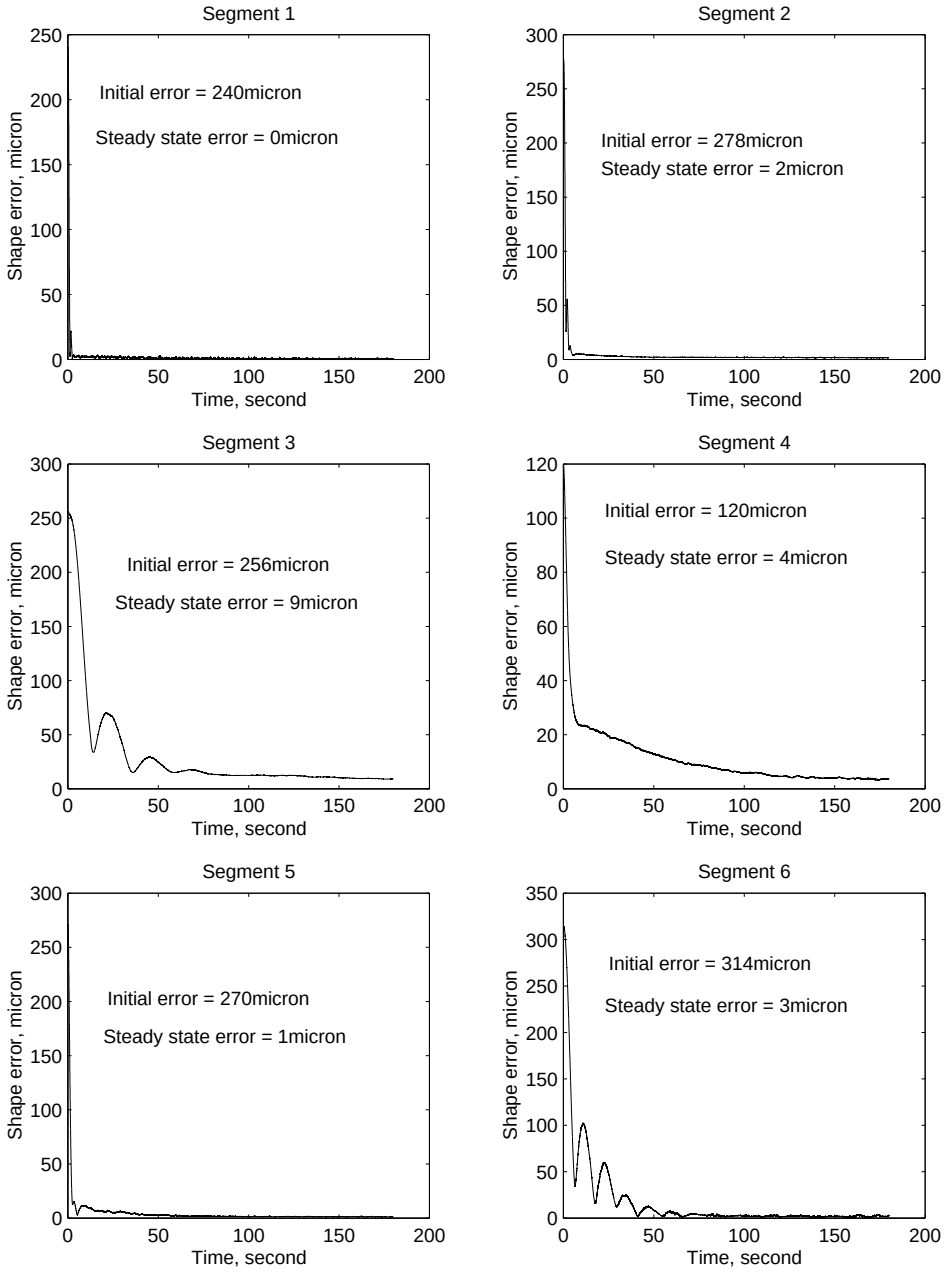

Figure 6.17: Closed-loop real-time results with decentralized and adaptive control

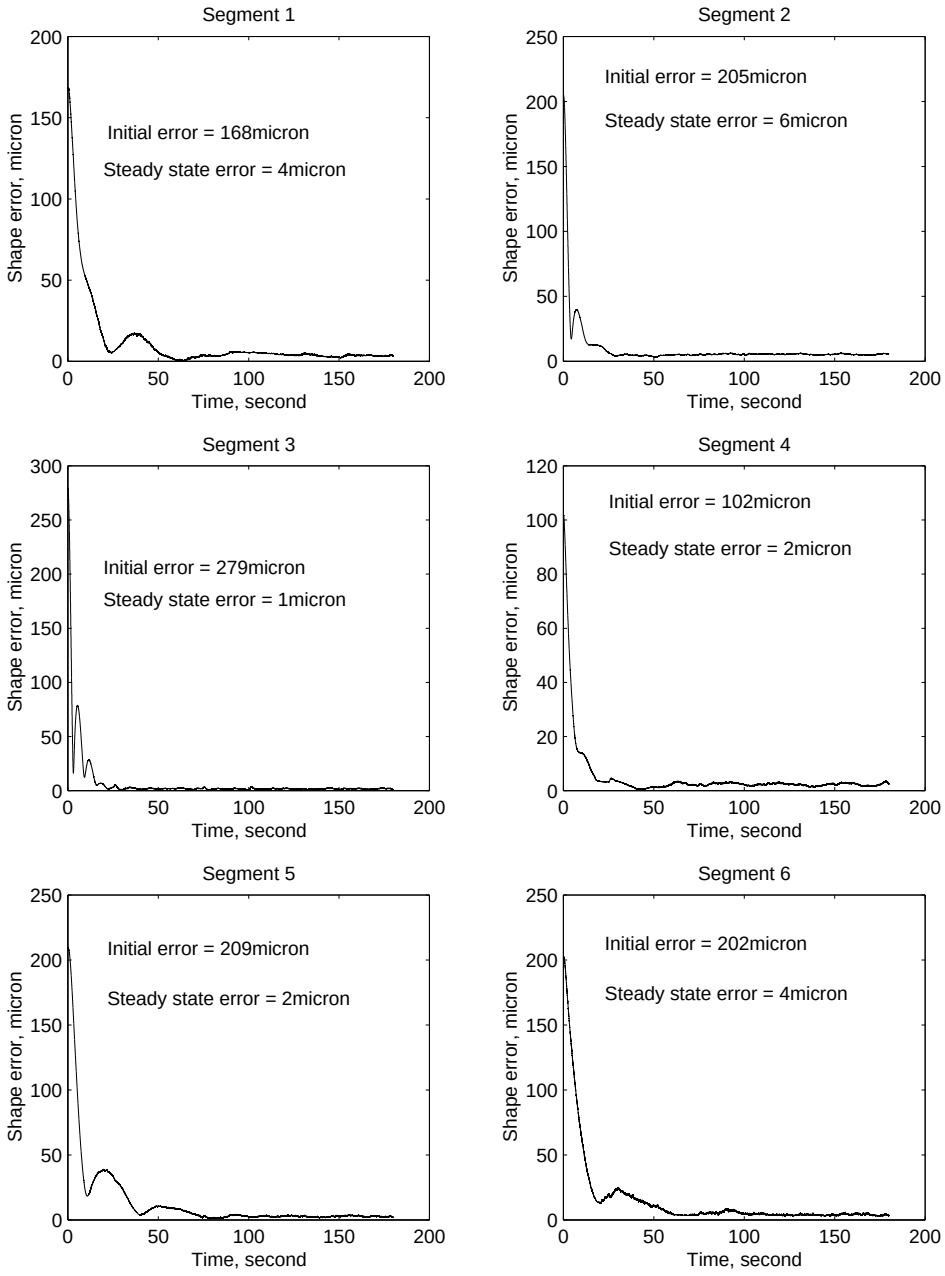

Figure 6.18: Closed-loop real-time results with overlapping decentralized and adaptive control

Chapter 7

Simplified Decentralized Control Design

The control of large segmented telescopes is a challenging one due to the complexity and high order of the system. The high order dynamics lead to high order controllers that require more memory and faster computations for implementation. While this may not pose a serious problem for a small number of segments, as the number of segments increases the computational requirements are becoming enormous.

In this chapter, we use the test-bed developed at California State University in Los Angeles that simulates in real-time a large segmented telescope to test the performance and computational requirements of several control designs. Three decentralized control designs were selected for implementation. These include a decentralized state feedback proportional plus integral ($DSFPI$) controller, a decentralized output feedback proportional plus integral ($DOPFI$) controller, and a decentralized direct adaptive output feedback ($DDAOF$) controller.

The $DSFPI$ controller requires more memory space and computational power than the $DOFPI$ and $DDAOF$ controllers. The $DOFPI$ requires less memory space and computational operations but it fails to meet the performance requirements. The $DDAOF$ requires an acceptable amount of memory space and computational operations and has better performance than the other two controllers.

7.1 Introduction

The model order of the primary mirror system is very large, which means that the computational complexity associated with the implementation of a centralized controller is very high. For example, using an H_∞ or LQR control design technique the order of the resulting controller is equal or larger than the order of the primary mirror model. For real-time implementation of these high order controllers, a single processor with high computational

power is required. These processors are either expansive or not available for a particular implementation. One way to overcome this problem is to divide the primary mirror system into a number of subsystems and then design a less complex controller (local controller) for each subsystem. These local controllers can be simultaneously implemented using a number of less expansive processors working in parallel. In this work, three types of decentralized controllers are designed and implemented to the primary mirror system. Each local controller is responsible for the control of a single active panel, adding up to a total of 6-local controllers. Our objective is to design and implement different simple decentralized control schemes, compare their performance and computational effort, and come up with candidate controllers that meet the performance requirements with the least computational effort.

7.2 Decentralized Control Design

7.2.1 Decentralized State Feedback Proportional Plus Integral ($DSFPI$) Control

For the design of the $DSFPI$ control we express the primary mirror model as:

$$\begin{bmatrix} y_1 \\ y_2 \\ y_3 \\ y_4 \\ y_5 \\ y_6 \end{bmatrix} = \begin{bmatrix} G_{11}(s) & 0 & 0 & 0 & 0 & 0 \\ 0 & G_{22}(s) & 0 & 0 & 0 & 0 \\ 0 & 0 & G_{33}(s) & 0 & 0 & 0 \\ 0 & 0 & 0 & G_{44}(s) & 0 & 0 \\ 0 & 0 & 0 & 0 & G_{55}(s) & 0 \\ 0 & 0 & 0 & 0 & 0 & G_{66}(s) \end{bmatrix} \begin{bmatrix} u_1 \\ u_2 \\ u_3 \\ u_4 \\ u_5 \\ u_6 \end{bmatrix} + \begin{bmatrix} 0 & G_{12}(s) & G_{13}(s) & G_{14}(s) & G_{15}(s) & G_{16}(s) \\ G_{21}(s) & 0 & G_{23}(s) & G_{24}(s) & G_{25}(s) & G_{26}(s) \\ G_{31}(s) & G_{32}(s) & 0 & G_{34}(s) & G_{35}(s) & G_{36}(s) \\ G_{41}(s) & G_{42}(s) & G_{43}(s) & 0 & G_{45}(s) & G_{46}(s) \\ G_{51}(s) & G_{52}(s) & G_{53}(s) & G_{54}(s) & 0 & G_{56}(s) \\ G_{61}(s) & G_{62}(s) & G_{63}(s) & G_{64}(s) & G_{65}(s) & 0 \end{bmatrix} \begin{bmatrix} u_1 \\ u_2 \\ u_3 \\ u_4 \\ u_5 \\ u_6 \end{bmatrix} \tag{7.1}$$

where the diagonal elements in the first matrix represent the dynamics of the 6-active panels when they are isolated from the other panels. The second matrix represents the interactions of the panels with each other. For the purpose of decentralized control design, theses interactions are ignored. The state space representations of the 6-decoupled subsystems are

given by:

$$\dot{x}_i = \widehat{A}_i x_i + \widehat{B}_i u_i \tag{7.2}$$

$$y_i = \widehat{C}_i x_i \qquad i = 1, 2, ..., 6 \tag{7.3}$$

where $x_i \in R^{40}$ is the *i-th* local state vector, $y_i \in R^3$ is the *i-th* local output vector, and $u_i \in R^3$ is the *i-th* local input vector. The $\widehat{A}_i$,$\widehat{B}_i$ and $\widehat{C}_i$ are known matrices of appropriate dimensions satisfying $G_{ii}(s) = \widehat{C}_i(sI - \widehat{A}_i)^{-1}\widehat{B}_i$. The decoupled models (7.2 and 7.3) are used to design the 6-local state feedback proportional plus integral controllers as:

$$local\ state\ estimator\ : \dot{\hat{x}}_i(t) = \widehat{A}_i\hat{x}_i(t) + \widehat{B}_i u_i(t) + F_i(y_i - \widehat{C}_i\hat{x}_i) \tag{7.4}$$

$$local\ controller\ : u_i(t) = -k_i\hat{x}_i(t) - l_i \int_0^t y_i(t)\, dt \qquad i = 1, 2, ..., 6 \tag{7.5}$$

where $\hat{x}_i \in R^{40}$ is the estimate of the *i-th* local state vector x_i. The gain matrices $F_i \in R^{40\times 3}$, $k_i \in R_{,}^{3\times 40}$ and $l_i \in R^{3\times 3}$ are obtained following the standard LQR plus integral design procedure [47]. The controller gains are varied using different weights in the LQR cost until a desired closed-loop response is obtained.

7.2.2 Decentralized Output Feedback Proportional Plus Integral ($DOFPI$) Control

The state space realization of the designed $DSFPI$ control has a large order for each local controller. For this reason, we seek another decentralized control design that has a small order. The obvious way is to consider a $DOFPI$ control instead of using a state feedback. In this case, the order of each local controller is reduced to the number of local outputs. In this work, the $DOFPI$ control is designed following different approach than the one used to design the $DSFPI$ control. In fact, the local controllers are designed using the overall model of the primary mirror system. The 6-local output feedback proportional plus integral controllers are generated by:

$$u_i(t) = -\widehat{k}_i y_i(t) - \widehat{l}_i \int_0^t y_i(t)\, dt \qquad i = 1, 2, ..., 6 \tag{7.6}$$

where the gain matrices $\widehat{k}_i \in R_{,}^{3\times 3}$ and $\widehat{l}_i \in R^{3\times 3}$ are obtained using a Lyapunov inequality equation and the overall system model. The details of computing the controller gains are presented below.

Consider the state space representation of a system given by:

$$\dot{x} = Ax + Bu \tag{7.7}$$
$$y = Cx \tag{7.8}$$

where $x \in R^n$ is the system state vector, $u = \left[\begin{array}{cccc} u_1^T & u_2^T & \dots & u_m^T \end{array} \right]^T \in R^q$ is the input vector, and $y = \left[\begin{array}{cccc} y_1^T & y_2^T & \dots & y_m^T \end{array} \right]^T \in R^q$ is the output vector. The matrices A,B, and C are of appropriate dimensions. We differentiate the state equation (7.7) with respect to time t and express it as:

$$\dot{v} = A_v v + B_v \dot{u} \tag{7.9}$$
$$y = C_v v \tag{7.10}$$

where

$$v = [\dot{x}^T y^T]^T,\ A_v = \left[\begin{array}{cc} A & 0 \\ C & 0 \end{array} \right] \quad , B_v = \left[\begin{array}{c} B \\ 0 \end{array} \right] \quad , and\ C_v = \left[\begin{array}{cc} 0 & I \end{array} \right]$$

We propose the following structure for the local controllers:

$$u_i(t) = -\widehat{k}_i y_i(t) - \widehat{l}_i \int_0^t y_i(t)\, dt \qquad i = 1, 2, ..., m \tag{7.11}$$

where the gain matrices $\widehat{k}_i$, and $\widehat{l}_i$ are to be selected. The local controllers (7.11) can be written in a compact form as $\dot{u} = -F v$ where F has the following structure:

$$F = \left[\begin{array}{ccccc} \widehat{k}_1 C_1 & \widehat{l}_1 & 0 & \cdots & 0 \\ \widehat{k}_2 C_2 & 0 & \widehat{l}_2 & \cdots & 0 \\ \vdots & \vdots & \vdots & \ddots & 0 \\ \widehat{k}_m C_m & 0 & 0 & \cdots & \widehat{l}_m \end{array} \right] \tag{7.12}$$

where $C = [C_1^T, C_2^T, ..., C_m^T]^T$. The following Lyapunov inequality equation is used to compute the constant gain matrix F that stabilizes the closed-loop system.

$$P(A_v - B_v F) + (A_v - B_v F)^T P < 0 \tag{7.13}$$

The problem is to find a positive definite matrix P and the controller gain F satisfying (7.13). This problem is not easy to solve because the Lyapunov inequality equation (7.13) is not linear in terms of P and F. However, if we fix $P > 0$ then the Lyapunov inequality is

converted to a linear matrix inequality (LMI), which can be easily solved for F.

The design procedure for the $DOFPI$ is summarized in the following steps:

1. Add and subtract each of PA_e to the first part and $A_e^T P$ to the second part of the inequality (7.13) to get $P(A_v + A_e - A_e - B_v F) + (A_v + A_e - A_e - B_v F)^T P < 0$ The matrix A_e is selected such that all eigenvalues of $A_v + A_e$ have a negative real part. This modification is required for the next step because A_v has a number of eigenvalues at zero. For example one can select $A_e = \begin{bmatrix} 0 & 0 \\ 0 & \varepsilon I \end{bmatrix}$, where ε is a negative scalar
2. Find the positive definite matrix P satisfying: $P(A_v + A_e) + (A_v + A_e)^T P = -Q$, where Q is any positive definite matrix. For example select $Q = I$
3. Solve $P(-A_e - B_v F) + (-A_e - B_v F)^T P < Q$ for F using the *LMI-toolbox* [49].

7.2.3 Decentralized Direct Adaptive Output Feedback($DDAOF$) Control

The structure of the proposed $DDAOF$ control is shown in Fig 7.1.

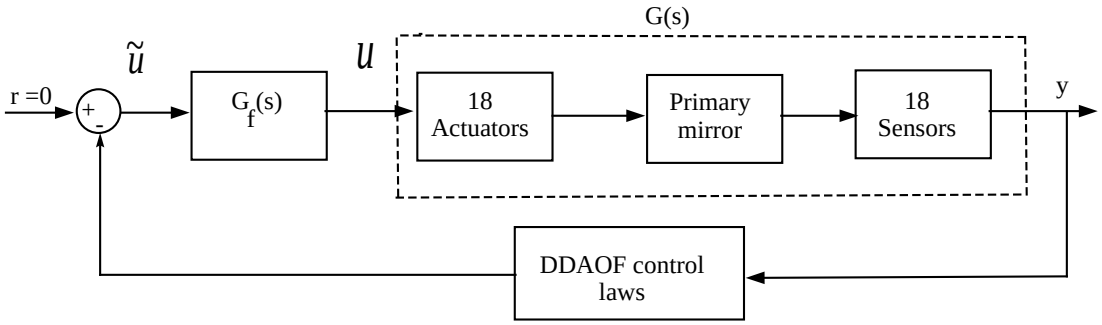

Figure 7.1: Centralized control system

In this figure, the decentralized input filter has the following structure:

$$G_f(s) = diag\{G_{f_1}(s), G_{f_2}(s), ..., G_{f_6}(s)\} \tag{7.14}$$

where $G_{f_i}(s) \in C^{3\times 3}$ is the *i-th* local filter. The $DDAOF$ control laws are generated as follows:

$$
\begin{aligned}
u_i &= G_{f_i}(s)\,\tilde{u}_i && (7.15)\\
\tilde{u}_i(t) &= -\frac{k_i(t)+l_i(t)}{1+\delta\,(k_i(t)+l_i(t))}\,y_i(t) && (7.16)\\
k_i(t) &= \alpha_i y_i^T(t) y_i(t) && (7.17)\\
\dot{l}_i(t) &= \beta_i y_i^T(t) y_i(t) && (7.18)
\end{aligned}
$$

where i =1, 2,. . . , 6, and $k_i \in R,\ l_i \in R$, and $\delta, \alpha_i,\ \beta_i$ are design positive constants. The filter $G_f(s)$ and scalar δ are designed such that $G(s)G_f(s)+\delta I$ is strictly positive real, this idea is generalized from [46]. The passivity is required to ensure the stability of the closed-loop system. The design details and stability analysis of the proposed $DDAOF$ control scheme are presented below.

Consider the proposed $DDAOF$ controller shown in Fig 7.2.

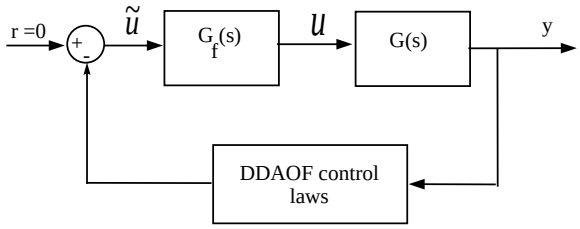

Figure 7.2: The proposed DDAOF controller

The state space realization of the filter $G_f(s)$ is given by:

$$
\begin{aligned}
\dot{\tilde{x}} &= \tilde{A}\,\tilde{x} + \tilde{B}\,\tilde{u} && (7.19)\\
u &= \tilde{C}\,\tilde{x} + \tilde{D}\,\tilde{u} && (7.20)
\end{aligned}
$$

where

$$
\begin{aligned}
\tilde{x} &= \begin{bmatrix} \tilde{x}_1^T & \dots & \tilde{x}_i^T & \dots & \tilde{x}_m^T \end{bmatrix}^T \in R^{\tilde{n}}\\
\tilde{u} &= \begin{bmatrix} \tilde{u}_1^T & \dots & \tilde{u}_i^T & \dots & \tilde{u}_m^T \end{bmatrix}^T \in R^{q}\\
\tilde{A} &= diag\left\{ \begin{array}{ccccc} \tilde{A}_1 & \dots & \tilde{A}_i & \dots & \tilde{A}_m \end{array} \right\}\\
\tilde{B} &= diag\left\{ \begin{array}{ccccc} \tilde{B}_1 & \dots & \tilde{B}_i & \dots & \tilde{B}_m \end{array} \right\}\\
\tilde{C} &= diag\left\{ \begin{array}{ccccc} \tilde{C}_1 & \dots & \tilde{C}_i & \dots & \tilde{C}_m \end{array} \right\}\\
\tilde{D} &= diag\left\{ \begin{array}{ccccc} \tilde{D}_1 & \dots & \tilde{D}_i & \dots & \tilde{D}_m \end{array} \right\}
\end{aligned}
$$

$\tilde{A}_j$, $\tilde{B}_j$, $\tilde{C}_j$, $\tilde{D}_j$ are constant matrices of appropriate dimensions and $G_f(s) = \tilde{C}(sI - \tilde{A})^{-1}\tilde{B} + \tilde{D}$.

Let $G_m(s) = G(s)G_f(s) + \delta\, I$ where δ is a scalar. The state space representation of $G_m(s)$ is given by:

$$\dot{\hat{x}} = \hat{A}\,\hat{x} + \hat{B}\,\tilde{u} \tag{7.21}$$

$$\tilde{y} = \hat{C}\,\hat{x} + \delta\ \tilde{u} = y + \delta\ \tilde{u} \tag{7.22}$$

where

$$\hat{x} = \begin{bmatrix} x^T & \tilde{x}^T \end{bmatrix}^T \in R^{n+\tilde{n}},\ \hat{A} = \begin{bmatrix} A & B\tilde{C} \\ 0 & \tilde{A} \end{bmatrix},\ \hat{B} = \begin{bmatrix} B\tilde{D} \\ \tilde{B} \end{bmatrix},\ \textit{and}\ \hat{C} = \begin{bmatrix} C & 0 \end{bmatrix}$$

and A, B, C are from the state space realization of $G(s) = C(sI - A)^{-1}B$.

Theorem 7.1 *If there exist a scalar δ and filter $G_f(s)$ such that $G_m(s) = G(s)G_f(s) + \delta\, I$ is SPR, then the following DDAOF control laws:*

$$u_i = G_{f_i}(s)\,\tilde{u}_i \qquad i = 1, 2, \ldots, m \tag{7.23}$$

$$\tilde{u}_i(t) = -\frac{k_i(t) + l_i(t)}{1 + \delta\ (k_i(t) + l_i(t))} y_i(t) \tag{7.24}$$

$$k_i(t) = \alpha_i y_i^T(t) y_i(t) \tag{7.25}$$

$$\dot{l}_i(t) = \beta_i y_i^T(t) y_i(t) \tag{7.26}$$

where α_i and β_i are design positive constants, can stabilize the system of Fig. 7.2 and force the output vector y to zero exponentially fast.

The following Lemma is used to prove Theorem 10.1.

Lemma 7.1 (Kalman-Yakubovich-Popov Lemma [51]) *The transfer function matrix $G_m(s) = \hat{C}(sI - \hat{A})^{-1}\hat{B} + \delta\ I$ is SPR if and only if there exist matrices $P = P^T > 0$, L, and W, and a constant $\varepsilon > 0$ such that:*

$$P\hat{A} + \hat{A}^T P = -L^T L - \varepsilon P \tag{7.27}$$

$$P\hat{B} = \hat{C}^T - L^T W \tag{7.28}$$

$$W^T W = 2\delta\ I \tag{7.29}$$

Proof of Theorem 10.1: Use

$$V(\hat{x}) = \frac{1}{2}\hat{x}^T P\,\hat{x} \tag{7.30}$$

as a Lyapunov function candidate. The derivative of (7.30) along the trajectories of the system (7.21) is given by

$$\dot{V}(\hat{x}) = \frac{1}{2}\hat{x}^T P\,\dot{\hat{x}} + \frac{1}{2}\dot{\hat{x}}^T P\,\hat{x} \tag{7.31}$$

Substituting (7.21) into (7.31), we obtain

$$\dot{V}(\hat{x}) = \frac{1}{2}\hat{x}^T(P\hat{A} + \hat{A}^T P)\,\hat{x} + \hat{x}^T P\hat{B}\,\tilde{u} \tag{7.32}$$

Using (7.27) and (7.28) from Lemma 10.1, yields

$$\begin{aligned}\dot{V}(\hat{x}) &= -\tfrac{1}{2}\hat{x}^T L^T L\,\hat{x} - \tfrac{1}{2}\varepsilon\,\hat{x}^T P\,\hat{x} + \hat{x}^T(\hat{C}^T - L^T W)\tilde{u} \\ &= -\tfrac{1}{2}\hat{x}^T L^T L\,\hat{x} - \tfrac{1}{2}\varepsilon\,\hat{x}^T P\,\hat{x} + \hat{x}^T(\hat{C}^T - L^T W)\tilde{u} + \delta\,\tilde{u}^T\tilde{u} - \delta\,\tilde{u}^T\tilde{u} \\ &= -\tfrac{1}{2}\hat{x}^T L^T L\,\hat{x} - \tfrac{1}{2}\varepsilon\,\hat{x}^T P\,\hat{x} + (\hat{C}\,\hat{x} + \delta\ \tilde{u})^T\tilde{u} - \delta\,\tilde{u}^T\,\tilde{u} - \hat{x}^T L^T W\,\tilde{u}\end{aligned} \tag{7.33}$$

Using (7.29) from Lemma 10.1 and (7.22), we obtain

$$\dot{V}(\hat{x}) = -\frac{1}{2}\varepsilon\,\hat{x}^T P\,\hat{x} - \frac{1}{2}(L\,\hat{x} + W\,\tilde{u})^T(L\,\hat{x} + W\,\tilde{u}) + \tilde{y}^T\tilde{u} \tag{7.34}$$

Substituting $\tilde{y}^T\,\tilde{u} = \tilde{y}_1^T\tilde{u}_1 + \ldots + \tilde{y}_j^T\tilde{u}_j + \ldots + \tilde{y}_m^T\tilde{u}_m = \sum_{i=1}^{m}\tilde{y}_i^T\tilde{u}_i$ into (7.34), we have

$$\dot{V}(\hat{x}) = -\frac{1}{2}\varepsilon\,\hat{x}^T P\,\hat{x} - \frac{1}{2}(L\,\hat{x} + W\,\tilde{u})^T(L\,\hat{x} + W\,\tilde{u}) + \sum_{i=1}^{m}\tilde{y}_i^T\tilde{u}_i \tag{7.35}$$

Using the local controllers of Theorem 10.1, we have

$$\begin{aligned}&(1 + \delta\ (k_i(t) + l_i(t)))\,\tilde{u}_i(t) = -(k_i(t) + l_i(t))\,y_i(t) \\ &\textit{or} \\ &\tilde{u}_i(t) = -(k_i(t) + l_i(t))\,(y_i(t) + \delta\,\tilde{u}_i(t)) \\ &\qquad = -(k_i(t) + l_i(t))\,\tilde{y}_i(t)\end{aligned} \tag{7.36}$$

Substituting (7.36) into (7.35), we have

$$\dot{V}(\hat{x}) = -\frac{1}{2}\varepsilon\,\hat{x}^T P\,\hat{x} - \frac{1}{2}(L\,\hat{x} + W\,\tilde{u})^T(L\,\hat{x} + W\,\tilde{u}) - \sum_{i=1}^{m}(k_i + l_i)\tilde{y}_i^T\tilde{y}_i \tag{7.37}$$

Since $(k_i + l_i)\tilde{y}_i^T \tilde{y}_i \geq 0$, we have

$$\dot{V}(\hat{x}) \leq -\frac{1}{2}\varepsilon\, \hat{x}^T P\, \hat{x} \tag{7.38}$$

which implies that $\|\hat{x}(t)\|$ is bounded and converges to zero exponentially fast. Since $\hat{x} = [x^T \tilde{x}^T]^T$ we also have $\|x(t)\|$, $\|\tilde{x}(t)\|$ going to zero exponentially fast. Since $y = Cx$ we have that $\|y(t)\|$ going to zero exponentially fast. The above analysis also implies that x, $\tilde{x}$ and y are square integrable i.e. they are L_2-signals. From (7.26) we have $l_i(t) = \beta_i \int_0^t y_i^T(\tau) y_i(\tau)\, d\tau$, since $y_i \in L_2$ it follows that $l_i(t)$ is bounded and $\lim_{t\to\infty} l_i(t) = \beta_i \int_0^\infty y_i^T(\tau) y_i(\tau)\, d\tau = \bar{l}_i < \infty$. Hence all signals are bounded in addition to $\|y_i(t)\|$ converging to zero exponentially fast.

Remark* 1*: The following lemma shows that there always exists a scalar δ such that $G_m(s)$ is *SPR*.

Lemma 7.2 *For any $n \times n$ proper transfer function matrix $\tilde{G}_m(s) = \hat{C}(sI - \hat{A})^{-1}\hat{B}$ with all elements analytic in the closed right-half complex plane, there exists a scalar δ such that $G_m(s) = \tilde{G}_m(s) + \delta\, I$ is SPR.*

The following Definition is used for the proof of Lemma 10.2.

Definition 7.1 *[48]: Let $G_m(s)$ be an $n \times n$ transfer function matrix and also let $G_h(jw) = G_m(jw) + G_m^T(-jw)$. Then $G_m(s)$ is SPR if:*

1. *$G_m(s)$ is analytic in the closed right-half complex plane*
2. *$G_h(jw) > 0 \;\; \forall\, w \in (-\infty, \infty)$*
3. *$G_h(\infty) \geq 0$*
4. *$\lim_{w\to\infty} w^2 G_h(jw) > 0$ if $G_h(\infty)$is singular.*

***Proof of Lemma* 2:** Since we assumed that all elements of $G_m(s)$ are analytic in the closed right-half complex plane, therefore condition 1 of definition 10.1 is satisfied.

Now $G_m(s)$ is *SPR* if $G_h(jw)$ is positive definite for any real w or the eigenvalues of $G_h(jw)$ are positive for any real w (including $w = \infty$). The characteristic equation of $G_h(jw)$ at each w is

$$\begin{aligned} \Delta(\lambda_w, w) := |\lambda_w I - G_h(jw)| &= \left|\lambda_w I - (\tilde{G}_m(jw) + \tilde{G}_m^T(-jw) + 2\delta\, I)\right| \\ &= \left|(\lambda_w - 2\delta\,)I - (\tilde{G}_m(jw) + \tilde{G}_m^T(-jw))\right| = 0 \end{aligned} \tag{7.39}$$

where λ_w is the eigenvalue of $G_h(jw)$ at each w. Let $\lambda_{\min}$ be the minimum eigenvalue of $\tilde{G}_m(jw) + \tilde{G}_m^T(-jw) \quad \forall\, w \in (-\infty, \infty)$, then for

$$\delta > -\frac{1}{2}\lambda_{\min} \tag{7.40}$$

we have $\lambda_w > 0$. Therefore condition 2 of definition 10.1 is satisfied. For condition 3 of definition 10.1 we have $G_h(\infty) = 2\delta\, I \geq 0$ for $\delta \geq 0$. Therefore condition 3 is satisfied. Choosing $\delta > \max\{0, -\frac{1}{2}\lambda_{\min}\}$ we satisfied conditions 2 and 3 as well as condition 4.

***Remark* 2:** The following Lemma can be used to find the constant matrices of the filter and δ analytically.

Lemma 7.3 *[50]: The transfer function matrix $G_m(s) = \hat{C}(sI - \hat{A})^{-1}\hat{B} + \delta\, I$ is SPR if and only if there exists a positive definite matrix H such that:*

$$\begin{bmatrix} \hat{A}H + H\hat{A}^T & \hat{B} - H\hat{C}^T \\ \hat{B}^T - \hat{C}H & -2\delta\, I \end{bmatrix} < 0 \tag{7.41}$$

The matrix inequality (7.41) is not linear in terms of H and the filter matrices and therefore it is not easy to solve. However, if we select some filter matrices we can convert it to an *LMI* problem. For example, choose $\tilde{A} = \alpha I$ *and* $\tilde{C} = I$ where α is some negative value. In this case the matrix inequality (7.41) can be easily solved for the other design matrices and δ using the *LMI toolbox* [49].

7.3 Experimental Results

The three controllers presented in the previous section are discretized first using a sampling period of 1 ms and then implemented to the primary mirror system. The real-time results for the three controllers are shown in Figures: 7.3, 7.4, and 7.5 for the 18-edge sensor outputs, 18-control commands, and 6-shape errors. In order to examine the effectiveness of the controllers, initial shape errors are created on the position of the primary mirror panels by adding constant loads on the panels. For the $DSFPI$ control, the number of states for each subsystem is 40. The number of computational operations required to implement the $DSFPI$ control is large and cannot be handled by the available $DSPs$. For this reason, we reduced the order of the 6-decoupled system models and designed new controllers with 17-states for each local controller. The 18-edge sensor outputs, 18-control commands, and 6-shape errors for the closed-loop system with reduced order $DSFPI$ control are shown in Fig 7.3.

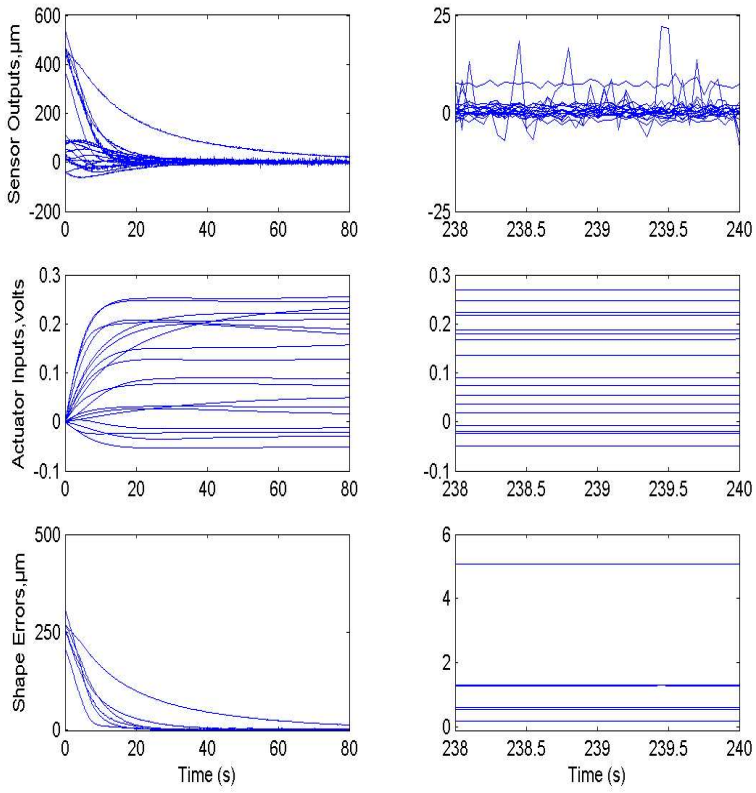

Figure 7.3: Closed-loop real-time results with DSFPI control (right column shows the steady state results)

These plots indicate that the closed-loop system is stable, the effect of the disturbances is reduced, and the control effort for all 18-actuators is within the limits (+/-1 V). For the $DOFPI$ controller, the number of computational operations is dramatically reduced when compared with the $DSFPI$ controller, since the number of controller states is now 3 for each local controller. The closed-loop system performance however is worst than that of the $DSFPI$ controller as shown in Fig 7.4.

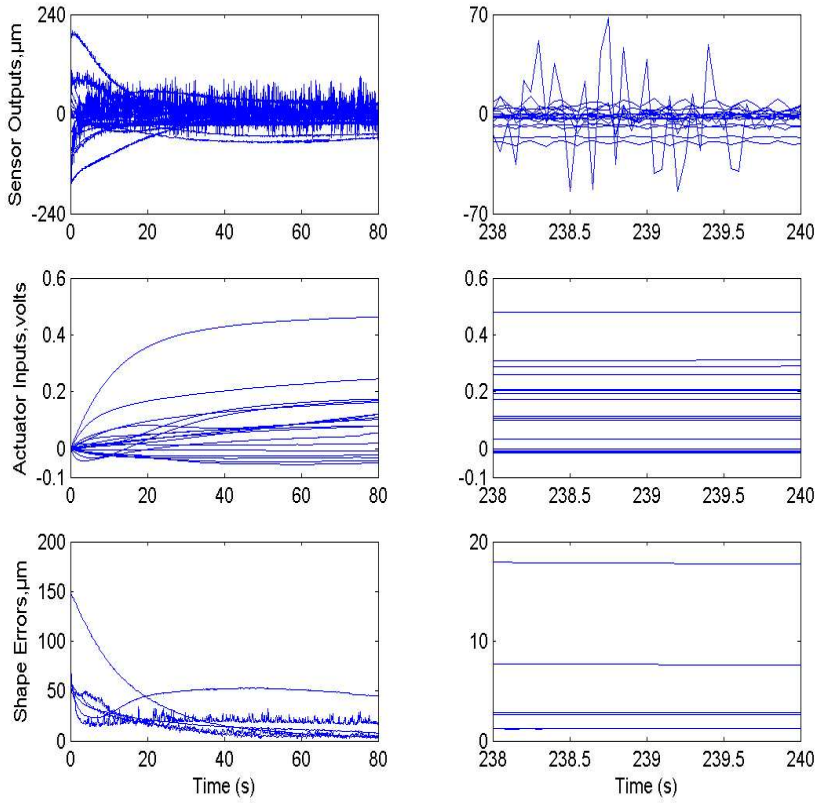

Figure 7.4: Closed-loop real-time results with DOFPI control (right column shows the steady state results)

The implementation results for the proposed $DDAOF$ controller are shown in Fig 7.5. The $DDAOF$ controller reduces the effect of the disturbance on the primary mirror panels by 100:1 faster than the other two designs.

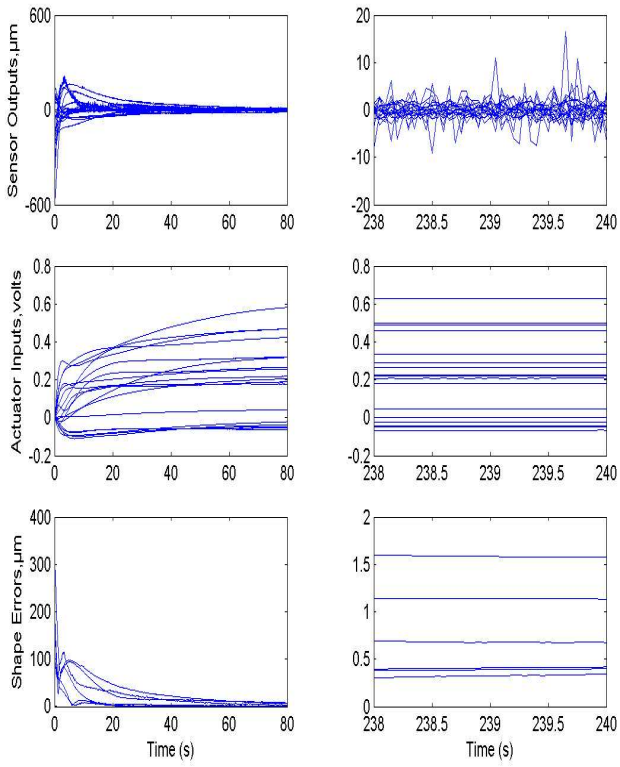

Figure 7.5: Closed-loop real-time results with DDAOF control (right column shows the steady state results)

The time it takes to compute any 18-control command samples by the 3-*DSPs* (the sampling time is 1 ms) is:

- 0.78 ms for the *DSFPI* control
- 0.2 ms for the *DOFPI* control
- 0.29 ms for the *DDAOF* control.

These results indicate that the *DOFPI* and *DDAOF* controllers take much less computational power of the 3-*DSPs* than the *DSFPI* controller. However, the *DOFPI* controller fails to meet the performance requirements. Overall the *DDAOF* controller performs better and required low computational effort. Table 7.1 shows the comparison between the three types of controllers.

Panel no.	Initial shape error values in μm.			Shape error values in μm at 240 s		
	DSFPI control	*DOFPI* control	*DDAOF* control	*DSFPI* control	*DOFPI* control	*DDAOF* control
1	277.339	61.640	107.979	1.43	2.6	0.66
2	318.624	71.132	251.199	0.72	15.7	0.72
3	259.205	151.658	363.237	1.01	1.44	1.52
4	214.905	52.087	233.563	0.27	1.94	1.17
5	272.448	55.378	159.361	4.57	2.69	0.5
6	278.812	101.999	124.334	2.08	7.20	0.3

Table 7.1: The shape error values for the three types of controllers

Chapter 8

Control Designs For The Segmented Telescope Test Bed With A Secondary Mirror

The control design and implementation for the segmented telescope test-bed in **SPACE** Lab has been discussed in Chapter 6 and 7. However the control mechanism for the secondary mirror was not available at that time. In this chapter, we use the finite element model including the secondary mirror for the control design and simulation. In the decentralized case, the secondary is treated as an additional segment just like one of the 6 segments of the primary mirror. In the overlapping decentralized control case, the overlapped subsystem is constituted by combining the secondary mirror with each of the 6 primary mirror segments.

8.1 Description of Finite Element Model

A 124-state linear model was obtained through finite element analysis. In this chapter, we use this model for design, analysis, and simulations. The state-space representation of the open-loop structure is

$$\begin{aligned} \dot{x} &= Ax + Bu \\ y &= Cx, \end{aligned} \tag{8.1}$$

where $A \in \mathcal{R}^{124\times124}$, $B \in \mathcal{R}^{124\times21}$, $C \in \mathcal{R}^{21\times124}$. State vector x consists of modal amplitudes and modal rates. $y = [y_1, y_2, \cdots, y_{21}]'$ is the output vector; $y_1, \cdots, y_{18}$ represents the 18 virtual displacements of the primary mirror in mm; and y_{19}, y_{20}, y_{21} are the outputs of the 3 position sensors of the secondary mirror in mm. The 21 linear electromagnetic actuators working in the current mode are used to provide the required force command to keep the segments in the desired shape. The input vector $[u_1, u_2, \cdots, u_{18}]'$ represents the forces applied

to the primary mirror; and u_{19}, u_{20}, u_{21} are the inputs to the 3 actuators on the secondary mirror. The dynamics of these actuators are neglected so that the output force is represented as $u_i = k_a I_i, i = 1, \cdots, 18$, where I_i is the input current to motor i in amp, u_i is the output force of motor i in $Newton$, and k_a is the force constant. The Singular value Bode plot of the finite element model is shown in Fig 8.1.

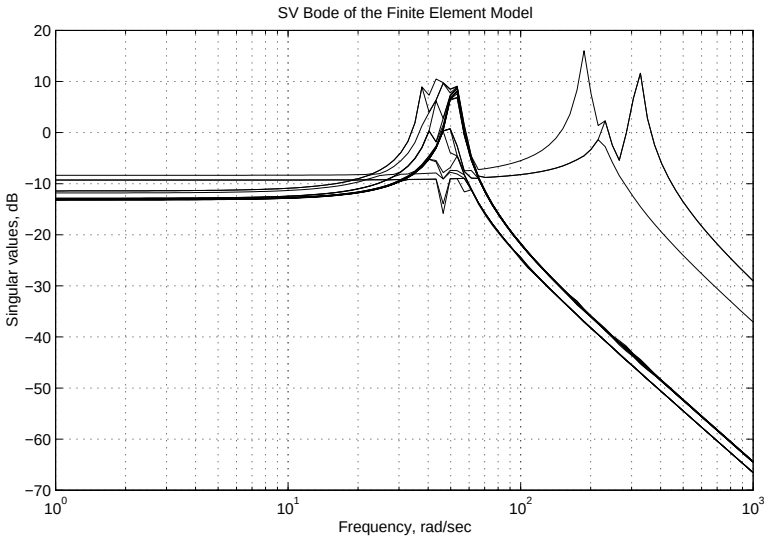

Figure 8.1: **SPACE** Segmented telescope test-bed FEM

8.2 Decentralized Control Design

As we did in Chapter 3, we are interested in a decentralized control technique where each sub-controller controls the three actuators of each segment and uses measurements from the sensors of the corresponding segment. In addition, we will treat the secondary mirror as the 7^{th} subsystem. We chose the following weights in the control design

$$\begin{aligned} W_1(s) &= \frac{(s+0.8944)^2}{(0.707s+10)^2} \\ W_2(s) &= \frac{400}{s^2} \end{aligned}$$

The frequency response of decentralized control design are shown in Fig 8.2- 8.8. The overall frequency response of the closed-loop system is shown in Fig 8.9.

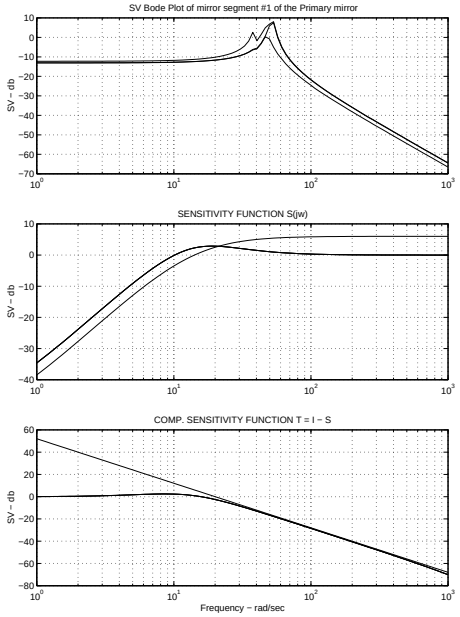

Figure 8.2: Design for mirror segment 1

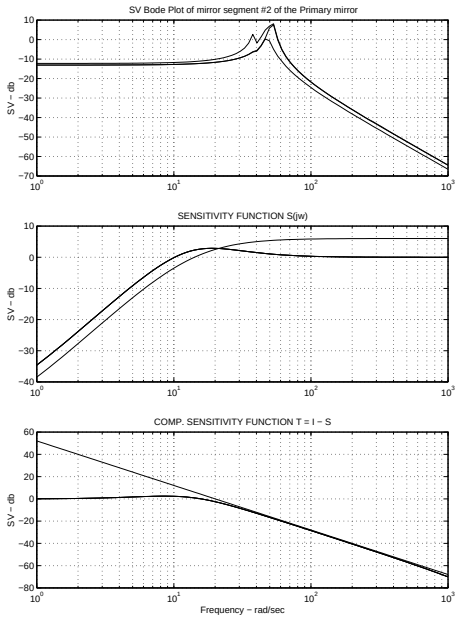

Figure 8.3: Design for mirror segment 2

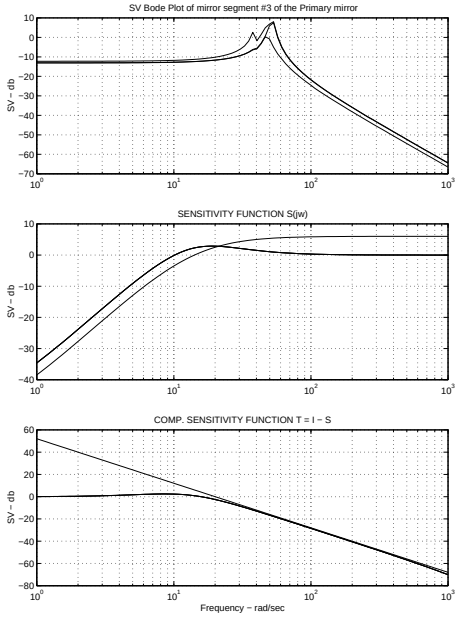

Figure 8.4: Design for mirror segment 3

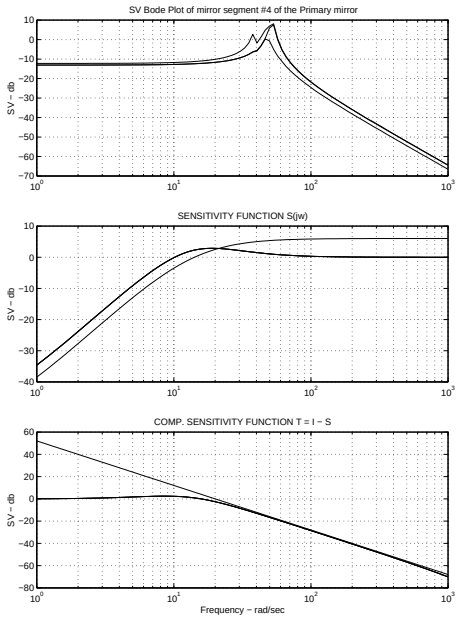

Figure 8.5: Design for mirror segment 4

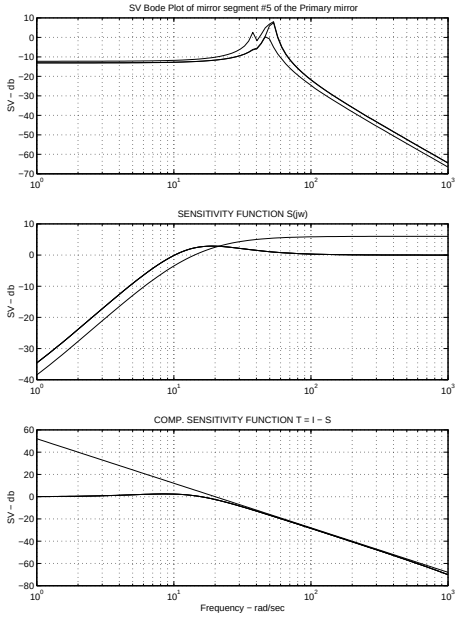

Figure 8.6: Design for mirror segment 5

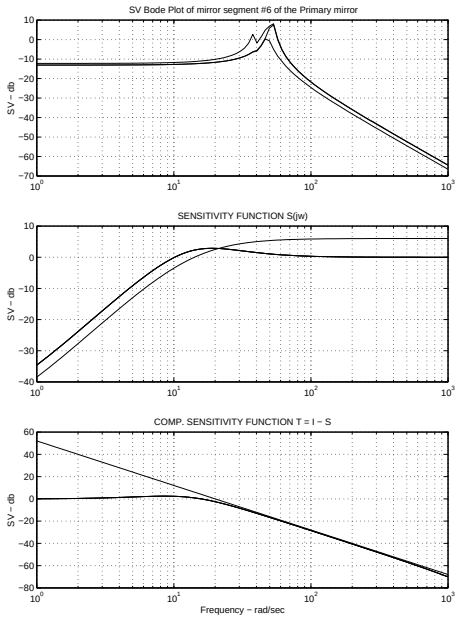

Figure 8.7: Design for mirror segment 6

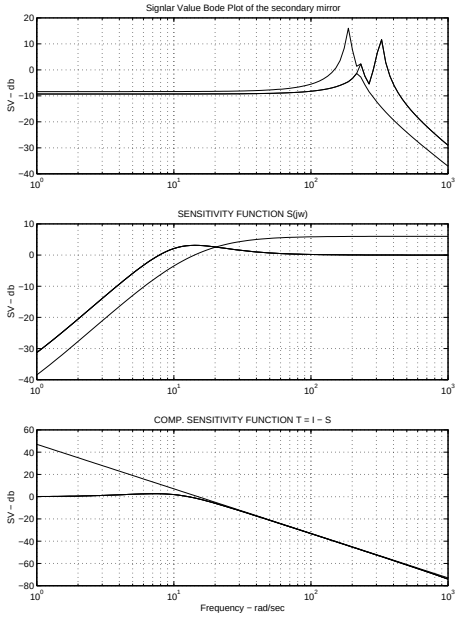

Figure 8.8: Design for secondary mirror

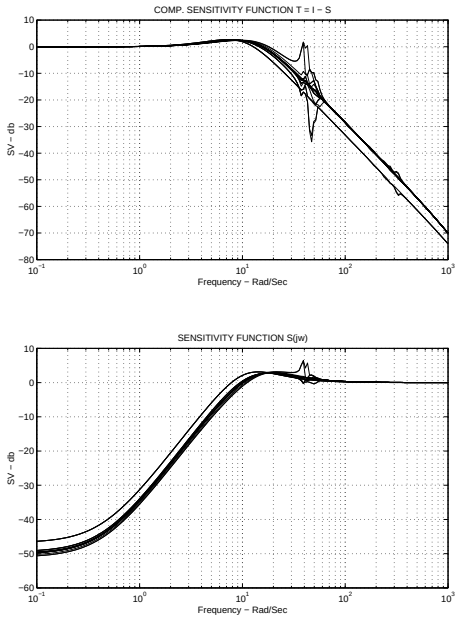

Figure 8.9: Design for secondary mirror

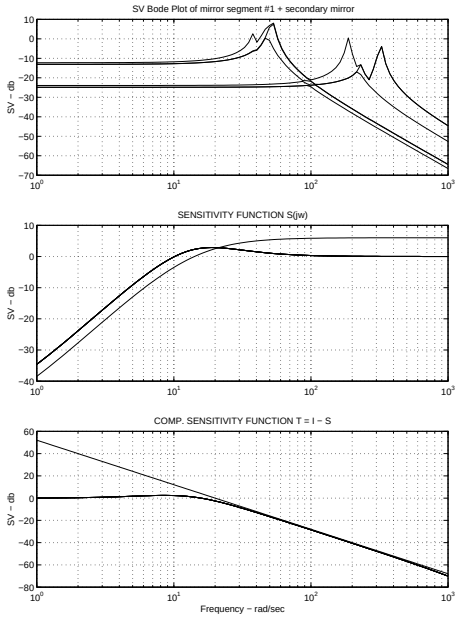

Figure 8.10: Design for mirror segment 1 and secondary

8.3 Overlapping Decentralized Control Design

Since the secondary mirror is coupled with all the segments of the primary mirror dynamically through the truss structure, here we propose the overlapping decentralized control design by combining the secondary mirror with each of the 6 primary mirror segments as an overlapped subsystem. We choose the same weights as in decentralized control

$$\begin{aligned} W_1(s) &= \frac{(s+0.8944)^2}{(0.707s+10)^2} \\ W_2(s) &= \frac{400}{s^2} \end{aligned}$$

The frequency response of overlapping decentralized control design is shown in Fig 8.10-8.15. The overall frequency response of the closed-loop system is shown in Fig 8.16.

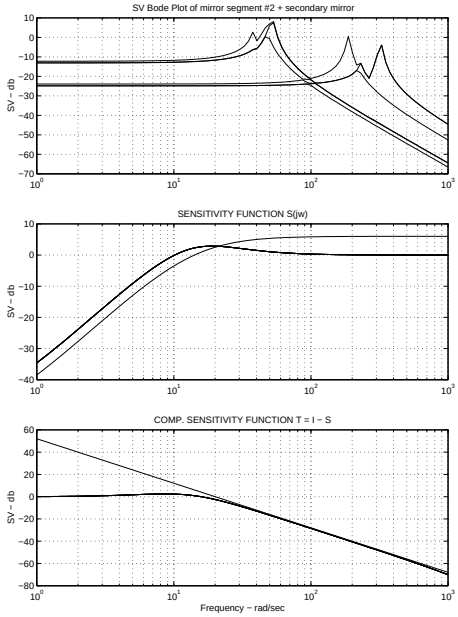

Figure 8.11: Design for mirror segment 2 and secondary

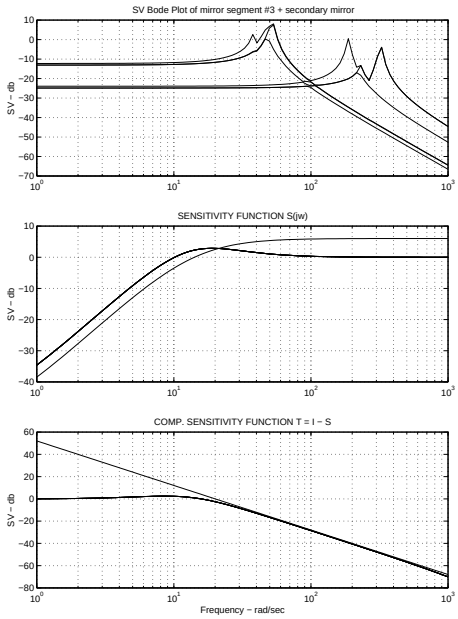

Figure 8.12: Design for mirror segment 3 and secondary

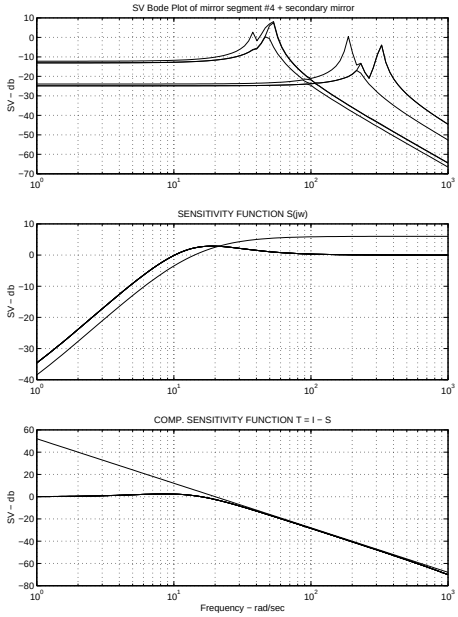

Figure 8.13: Design for mirror segment 4 and secondary

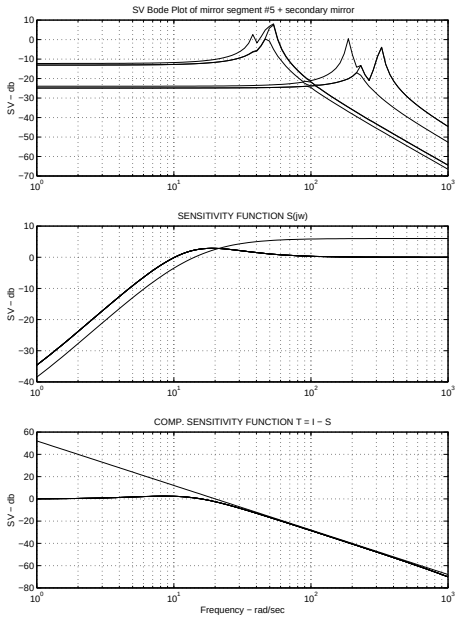

Figure 8.14: Design for mirror segment 5 and secondary

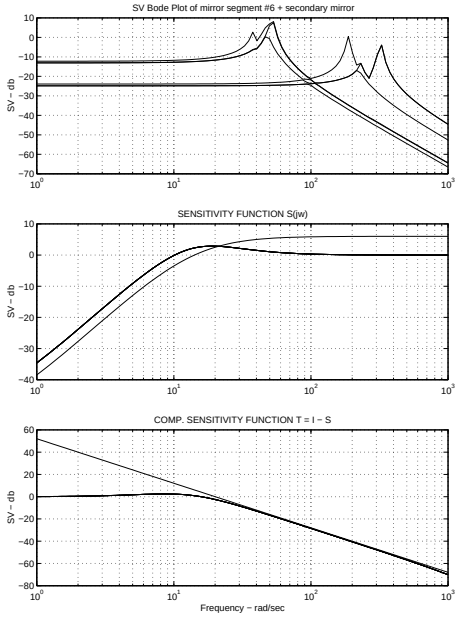

Figure 8.15: Design for mirror segment 6 and secondary

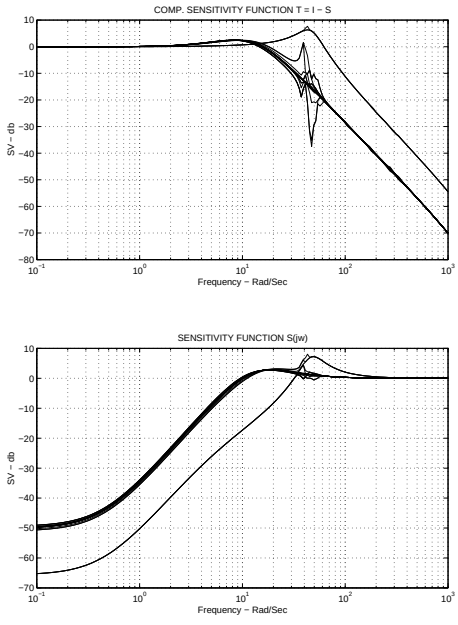

Figure 8.16: Design for secondary mirror

8.4 Simulation Results

To demonstrate our results, the different control schemes are simulated using the finite element model in the time domain. Disturbances are force/torques in nature. The disturbances are typically quasi-static such as gravity loads, thermally induced loads, actuator bias errors and drifts, steady-state of outside disturbance. The effects of these disturbances are position errors which appear on the virtual measurements of the primary mirror and the position sensor measurements of the secondary in the open-loop case. In the simulation, for the sake of simplicity, disturbances with 100 micron magnitude are directly added to the measurements of the 18 virtual measurements of the primary mirror and the 3 position sensor measurements to emulate the effects of the real disturbances. Three different scenarios are simulated here. First, a constant disturbance with magnitude 100 microns is applied to all 21 channels of the telescope. Second, a sinusoidal disturbance with magnitude 100 microns and frequency $0.6rad/sec$ is applied to all 21 channels of the telescope. Finally, a sinusoidal noise with magnitude 1 microns and frequency $1000rad/sec$ is added to all the sensor measurements of the telescope. The time domain results are shown in Figs. 8.17-8.18.

In the decentralized control case, shown in Fig 8.17, the closed-loop output of each channel to both constant and sinusoidal disturbances of $0.6rad/sec$ is less than 1 micron at steady state, except the response of the secondary mirror position sensors. The sensor noise is also attenuated at $1000rad/sec$.

In the overlapping decentralized control case, shown in Fig 8.18, the closed-loop output of each channel to both constant and sinusoidal disturbances of $0.6rad/sec$ is less than 1 micron at steady state, which means the disturbance within the frequency range of $0 - 0.6rad/sec$ has been reduced by 100:1. The closed-loop output of each channel to the sensor noise is less than 0.01 micron. So the overlapping method can successfully reject the disturbances within the frequency range of $0 - 0.6rad/sec$.

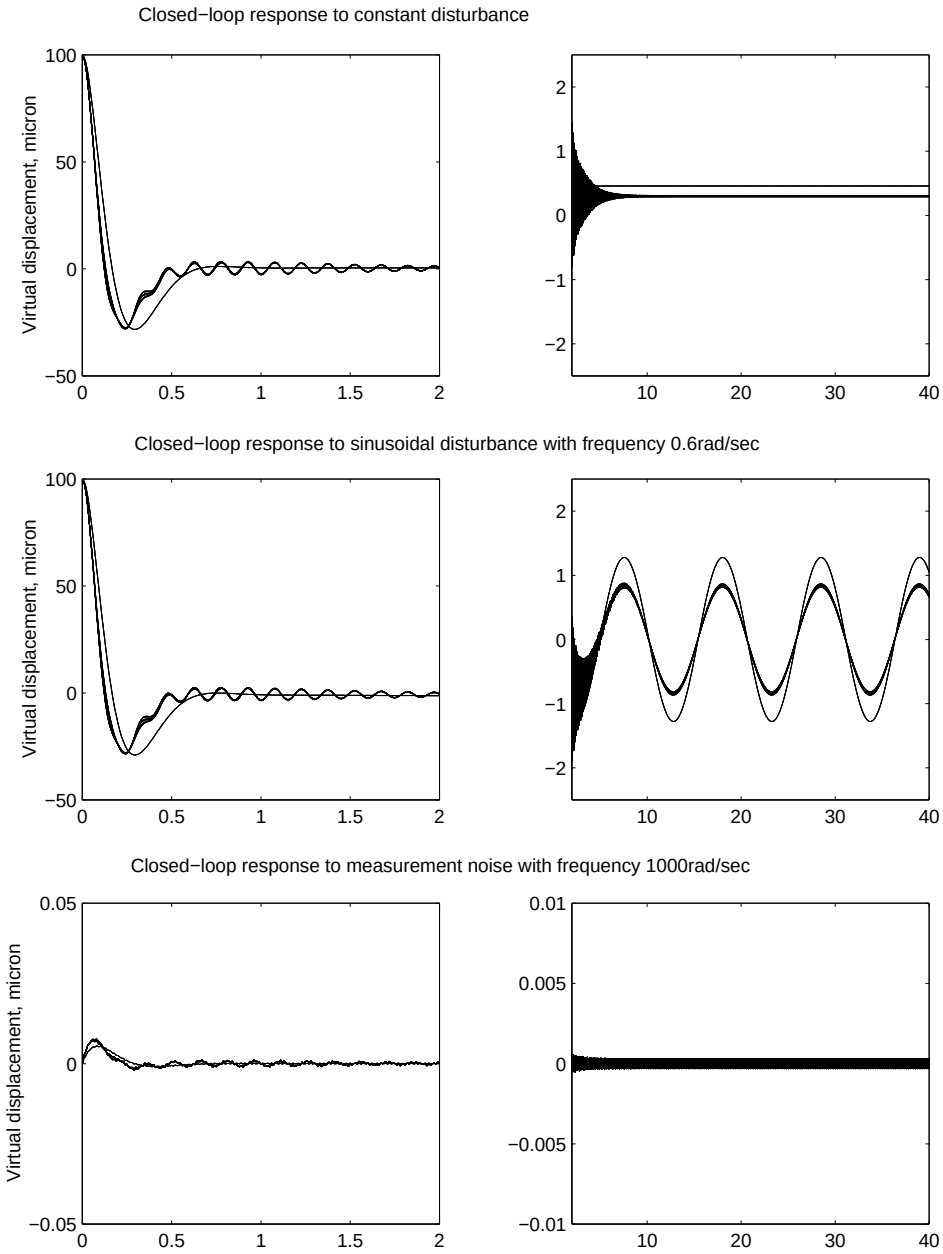

Figure 8.17: Closed-loop responses with decentralized control

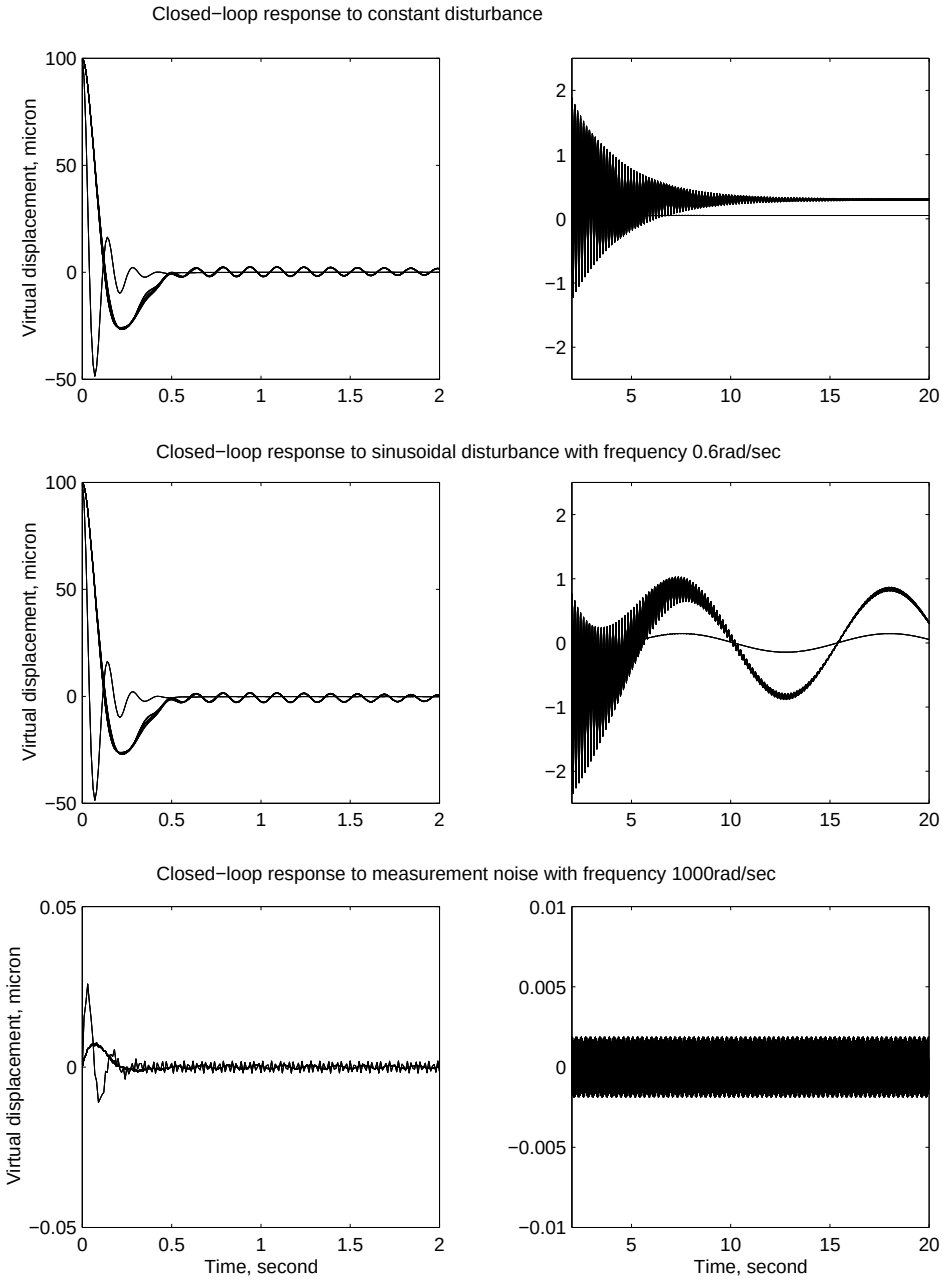

Figure 8.18: Closed-loop responses with overlapping decentralized control

Chapter 9

Overlapping Decentralized Control of Nonlinear Systems

In the chapter 3, we have shown that the overlapping decentralized control can be successfully applied to linear time invariant systems with overlapping interconnections. In this chapter, we apply the overlapping decentralized control to certain type of nonlinear systems.

9.1 Overlapping Decentralized Control With Input, State, And Output Inclusion

Before starting the analysis, let us review some of the results of the overlapping decentralized control of linear systems [23].

9.1.1 Input-output inclusion

We consider a pair of linear systems, $\mathbb{S}$

$$\begin{aligned} \dot{x} &= Ax + Bu \\ y &= Cx \end{aligned} \tag{9.1}$$

and $\tilde{\mathbb{S}}$

$$\begin{aligned} \dot{\tilde{x}} &= \tilde{A}\tilde{x} + \tilde{B}\tilde{u} \\ \tilde{y} &= \tilde{C}\tilde{x} \end{aligned} \tag{9.2}$$

where $x(t) \in \mathcal{R}^n$, $u(t) \in \mathcal{R}^m$, $y(t) \in \mathcal{R}^l$ are the state, input, output of the system $\mathbb{S}$ at time $t \in \mathcal{R}_+$, and $\tilde{x}(t) \in \mathcal{R}^{\tilde{n}}$, $\tilde{u}(t) \in \mathcal{R}^{\tilde{m}}$, $\tilde{y}(t) \in \mathcal{R}^{\tilde{l}}$ are the states of $\tilde{\mathbb{S}}$. The matrices A, B, C and $\tilde{A}$, $\tilde{B}$, $\tilde{C}$ are constant and of appropriate dimensions. The dimensions of the state, input,

and output of $\mathbb{S}$ are smaller than (or at least equal to) those of $\tilde{\mathbb{S}}$, respectively. The systems $\mathbb{S}$ and $\tilde{\mathbb{S}}$ are related by the transformations,

$$\begin{aligned} \tilde{x} &= Vx, & x &= U\tilde{x}, \\ \tilde{u} &= Ru, & u &= Q\tilde{u}, \\ \tilde{y} &= Ty, & y &= S\tilde{y}, \end{aligned} \tag{9.3}$$

where V, R, and T are constant matrices with proper dimensions and full column ranks; U, Q, S are constant matrices with proper dimensions and full row ranks, which satisfies the relations

$$UV = I_n, \qquad QR = I_m, \qquad ST = I_l. \tag{9.4}$$

In (9.4), I_m, I_n, and I_l are identity matrices of indicated dimensions.

Definition 9.1 *[23] We say that the system $\tilde{\mathbb{S}}$ includes the system $\mathbb{S}$, that is, $\mathbb{S}$ is included by $\tilde{\mathbb{S}}$, if there exists a quadruplet (U, V, R, S) such that, for any initial state x_0 and any fixed input $u(t)$ of $\mathbb{S}$, the choice*

$$\begin{aligned} \tilde{x}_0 &= Vx_0 \\ \tilde{u}(t) &= Ru(t) \qquad \forall t \geq 0 \end{aligned} \tag{9.5}$$

of the initial state $\tilde{x}_0$ and the input $\tilde{u}(t)$ of $\tilde{\mathbb{S}}$, implies

$$\begin{aligned} x(t; x_0, u) &= U\tilde{x}(t; \tilde{x}_0, \tilde{u}) \\ y[x(y)] &= S\tilde{y}[\tilde{x}(t)] \qquad \forall t \geq 0 \end{aligned} \tag{9.6}$$

The condition of this definition implies that the system $\tilde{\mathbb{S}}$ contains all the necessary information about the behavior of the system $\mathbb{S}$. we can extract any property such as stability and optimality of $\mathbb{S}$ from $\tilde{\mathbb{S}}$, which is the underlining idea of the Inclusion Principle [24].

If the system $\tilde{\mathbb{S}}$ includes system $\mathbb{S}$, then $\tilde{\mathbb{S}}$ is said to be an expansion of $\mathbb{S}$, and $\mathbb{S}$ is called a contraction of $\tilde{\mathbb{S}}$.

Theorem 9.1 *[23] The system $\tilde{\mathbb{S}}$ includes the system $\mathbb{S}$ if and only if there exists a quadruplet (U, V, R, S) such that*

$$\begin{aligned} A^i = U\tilde{A}^i V, \quad A^i B = U\tilde{A}^i \tilde{B} R, \quad CA^i = S\tilde{C}\tilde{A}^i V, \\ CA^i B = C\tilde{C}\tilde{A}^i \tilde{B} R \qquad \forall i = 0, 1, 2, \ldots \end{aligned} \tag{9.7}$$

When we consider overlapping decompositions of $\mathbb{S}$, we are interested in generating expansions $\tilde{\mathbb{S}}$ of $\mathbb{S}$. If the pairs of matrices (U, V), (Q, R), and (S, T) are specified, the matrices $\tilde{A}$, $\tilde{B}$, and $\tilde{C}$ can be expressed as

$$\tilde{A} = VAU + M, \qquad \tilde{B} = VBQ + N, \qquad \tilde{C} = TCU + L, \tag{9.8}$$

where M, N, and L are complementary matrices of appropriate dimensions. For $\tilde{\mathbb{S}}$ to be an expansion of $\mathbb{S}$, aproper choice of M, N, and L is required, which is provided by the following:

Theorem 9.2 *[23] The system $\tilde{\mathbb{S}}$ is an expansion of the system $\mathbb{S}$, if and only if*

$$\begin{aligned} UM^iV = 0, \qquad & UM^{i-1}NR = 0 \\ SLM^{i-1}V = 0, \qquad & SLM^{i-1}NR = 0 \\ & \forall i = 1, 2, \ldots, \tilde{n} \end{aligned} \tag{9.9}$$

Definition 9.2 *We say that the system $\mathbb{S}$ is a restriction of $\tilde{\mathbb{S}}$, that is, $\tilde{\mathbb{S}}$ is an unrestriction of $\mathbb{S}$, if there exists a triplet (V, R, T), such that, for any initial state x_0 and fixed input $u(t)$ of $\mathbb{S}$, the choice*

$$\begin{aligned} \tilde{x_0} &= Vx_0 \\ \tilde{u} &= Ru(t), \qquad \forall t \geq 0 \end{aligned} \tag{9.10}$$

of the initial state and input of $\tilde{\mathbb{S}}$, implies

$$\begin{aligned} \tilde{x}(t; \tilde{x_0}, \tilde{u}) &= Vx(t; x_0, u) \\ \tilde{y}[\tilde{x}(t)] &= Ty[x(t)], \qquad \forall t \geq 0 \end{aligned} \tag{9.11}$$

Theorem 9.3 *The system $\mathbb{S}$ is a restriction of the system $\tilde{\mathbb{S}}$, if and only if*

$$MV = 0, \qquad NR = 0, \qquad LV = 0 \tag{9.12}$$

9.1.2 Contractibility of controllers

We consider a LTI controller, $\mathcal{C}$

$$\begin{aligned} \dot{z} &= Fx + Gy \\ u &= Hz + Ky + v \end{aligned} \tag{9.13}$$

for system $\mathbb{S}$, and a controller $\tilde{\mathcal{C}}$

$$\begin{aligned} \dot{\tilde{z}} &= \tilde{F}\tilde{z} + \tilde{G}\tilde{y} \\ \tilde{u} &= \tilde{H}\tilde{z} + \tilde{K}\tilde{y} + \tilde{v} \end{aligned} \tag{9.14}$$

for the expansion $\tilde{\mathbb{S}}$ of $\mathbb{S}$, where $z(t) \in \mathcal{R}^p$ and $\tilde{z}(t) \in \mathcal{R}^{\tilde{p}}$ are the states of the controllers $\mathcal{C}$ and $\tilde{\mathcal{C}}$ at time $t \in \mathcal{R}_+$, and $v(t) \in \mathcal{R}^m$ and $\tilde{v}(t) \in \mathcal{R}^{\tilde{m}}$ are new inputs to the resulting closed-loop systems. All matrices in (9.13) and (9.14) are constant and have appropriate dimensions. The state spaces of $\mathcal{C}$ and $\tilde{\mathcal{C}}$ are related by the transformations,

$$\tilde{z} = Ez, \qquad z = D\tilde{z}, \tag{9.15}$$

where E is a constant matrix with proper dimensions and full column rank; D is a constant matrix with proper dimension and full row rank, which satisfies the relation

$$DE = I_p. \tag{9.16}$$

Definition 9.3 *[23] We say that the controller $\tilde{\mathcal{C}}$ for the expansion $\tilde{\mathbb{S}}$ is contractible to the controller $\mathcal{C}$ for the original system $\mathbb{S}$, if there exists a pair (D, E) such that, for any initial state x_0 and any fixed input $u(t)$ of $\mathbb{S}$, any initial state z_0 of $\mathcal{C}$, the choice*

$$\begin{aligned} \tilde{x}_0 &= Vx_0 \\ \tilde{u}(t) &= Ru(t), \qquad \forall t \geq 0 \end{aligned} \tag{9.17}$$

of the initial state and input of $\tilde{\mathcal{C}}$, and

$$\tilde{z}_0 = Ez_0 \tag{9.18}$$

of the initial state $\tilde{\mathcal{C}}$, implies

$$\begin{aligned} z(t; z_0, y) &= D\tilde{z}(t; \tilde{z}_0, \tilde{y}) \\ R[Hz(t) + Ky(t)] &= \tilde{H}\tilde{z}(t) + \tilde{K}\tilde{y}(t) \qquad \forall t \geq 0 \end{aligned} \tag{9.19}$$

The above definition implies that if $\tilde{\mathcal{C}}$ is contractible to $\mathcal{C}$, then the closed-loop system (plant $\mathbb{S}$ and controller $\mathcal{C}$) is a contraction of the expanded closed-loop system (expansion $\tilde{\mathbb{S}}$ and controller $\tilde{\mathcal{C}}$). Then the definition of inclusion implies:

Theorem 9.4 *If the controller $\tilde{\mathcal{C}}$ for the expansion $\tilde{\mathbb{S}}$ is contractible to the controller $\mathcal{C}$ for the original system $\mathbb{S}$, the stability of the expanded closed-loop system implies the stability of the stability of the original closed-loop system.*

Now we consider the state feedback control laws

$$u = Kx + v \tag{9.20}$$

and

$$\tilde{u} = \tilde{K}\tilde{x} + \tilde{v} \tag{9.21}$$

for the system $\mathbb{S}$ and the expansion $\tilde{\mathbb{S}}$, respectively, we have the following:

Corollary 9.1 *The control law $\tilde{u} = \tilde{K}\tilde{x}+\tilde{v}$ for $\tilde{\mathbb{S}}$ is contractible to the control law $u = Kx+v$, if and only if*

$$\tilde{K}\tilde{A}^i V = RKA^i, \quad \tilde{K}\tilde{A}^i\tilde{B}^i R = RKA^i B, \quad \forall i = 0, 1, 2, \ldots \tag{9.22}$$

Corollary 9.2 *When $\mathbb{S}$ is a restriction of $\tilde{\mathbb{S}}$, the control law $\tilde{u} = \tilde{K}\tilde{x}+\tilde{v}$ for $\tilde{\mathbb{S}}$ is contractible to the control law $u = Kx + v$, if*

$$\tilde{K}T = RK \tag{9.23}$$

9.2 Overlapping Decentralized Control With State Feedback

Consider the system

$$\dot{x} = f(x, u) \tag{9.24}$$

where $f(0, 0) = 0$ and $f(x, u)$ is contionuously differentiable in a domain $D_x \times D_u$ with $x(t) \in \mathcal{R}^n$, $u(t) \in \mathcal{R}^m$ that contains the origin $(x = 0, u = 0)$. Furthermore, system (9.24) is assumed to have the following structure of dynamics

$$\begin{aligned} \dot{x}_1 &= f_1(x_1) + g_1(x_1)u_1 + h_1(x) \\ \dot{x}_2 &= f_2(x_2) + g_2(x_2)u_2 + h_2(x) \\ \dot{x}_3 &= f_3(x_3) + g_3(x_3)u_3 + h_3(x) \end{aligned} \tag{9.25}$$

where $f_i, g_i, h_i, x_i, u_i, i = 1, 2, 3$ have the appropriate dimensions. $h_i(x), i = 1, 2, 3$ are the interconnections. We want to design a state feedback control $u = \gamma(x)$ to stabilize the system. Linearization of (9.24) about $(x = 0, u = 0)$ results in the linear system

$$\begin{bmatrix} \dot{x}_1 \\ \dot{x}_2 \\ \dot{x}_3 \end{bmatrix} = \begin{bmatrix} A_{11} & A_{12} & A_{13} \\ A_{21} & A_{22} & A_{23} \\ A_{31} & A_{32} & A_{33} \end{bmatrix} \begin{bmatrix} x_1 \\ x_2 \\ x_3 \end{bmatrix} + \begin{bmatrix} B_{11} & 0 & 0 \\ 0 & B_{22} & 0 \\ 0 & 0 & B_{33} \end{bmatrix} \begin{bmatrix} u_1 \\ u_2 \\ u_3 \end{bmatrix} \tag{9.26}$$

where

$$A = \frac{\partial f(x,u)}{\partial x}|_{x=0,u=0}; B = \frac{\partial f(x,u)}{\partial u}|_{x=0,u=0} \tag{9.27}$$

Assume the pair (A, B) is controllable, or at least stabilizable.

We treat the system as composed of two overlapping subsystems

$$\begin{bmatrix} \dot{x}_1 \\ \dot{x}_2 \end{bmatrix} = \begin{bmatrix} A_{11} & A_{12} \\ A_{21} & A_{22} \end{bmatrix} \begin{bmatrix} x_1 \\ x_2 \end{bmatrix} + \begin{bmatrix} B_{11} & 0 \\ 0 & B_{22} \end{bmatrix} \begin{bmatrix} u_1 \\ u_2 \end{bmatrix} \tag{9.28}$$

and

$$\begin{bmatrix} \dot{x}_2 \\ \dot{x}_3 \end{bmatrix} = \begin{bmatrix} A_{22} & A_{23} \\ A_{32} & A_{33} \end{bmatrix} \begin{bmatrix} x_2 \\ x_3 \end{bmatrix} + \begin{bmatrix} B_{22} & 0 \\ 0 & B_{33} \end{bmatrix} \begin{bmatrix} u_2 \\ u_3 \end{bmatrix} \tag{9.29}$$

Consider the following state feedback laws,

$$\begin{bmatrix} u_1 \\ u_2 \end{bmatrix} = \begin{bmatrix} {k_{11}}^1 & {k_{12}}^1 \\ {k_{21}}^1 & {k_{22}}^1 \end{bmatrix} \begin{bmatrix} x_1 \\ x_2 \end{bmatrix} \tag{9.30}$$

$$\begin{bmatrix} u_2 \\ u_3 \end{bmatrix} = \begin{bmatrix} {k_{11}}^2 & {k_{12}}^2 \\ {k_{21}}^2 & {k_{22}}^2 \end{bmatrix} \begin{bmatrix} x_2 \\ x_3 \end{bmatrix} \tag{9.31}$$

Now we generate an expansion $\tilde{\mathbb{S}}$ of $\mathbb{S}$ using the transformation matrices:

$$V = \begin{bmatrix} I_{n_1} & 0 & 0 \\ 0 & I_{n_2} & 0 \\ 0 & I_{n_2} & 0 \\ 0 & 0 & I_{n_3} \end{bmatrix}, U = (V^T V)^{-1} V^T = \begin{bmatrix} I_{n_1} & 0 & 0 & 0 \\ 0 & I_{n_2}/2 & I_{n_2}/2 & 0 \\ 0 & 0 & 0 & I_{n_3} \end{bmatrix} \tag{9.32}$$

$$R = \begin{bmatrix} I_{m_1} & 0 & 0 \\ 0 & I_{m_2} & 0 \\ 0 & I_{m_2} & 0 \\ 0 & 0 & I_{m_3} \end{bmatrix}, Q = (R^T R)^{-1} R^T = \begin{bmatrix} I_{m_1} & 0 & 0 & 0 \\ 0 & I_{m_2}/2 & I_{m_2}/2 & 0 \\ 0 & 0 & 0 & I_{m_3} \end{bmatrix} \tag{9.33}$$

So that $\mathbb{S}$ is a restriction of $\tilde{\mathbb{S}}$.

Applying the above theorem, we obtain the expansion $\tilde{\mathbb{S}}$ as

$$\begin{aligned}\begin{bmatrix} \dot{\tilde{x}}_1 \\ \dot{\tilde{x}}_2 \end{bmatrix} &= \begin{bmatrix} A_{11} & A_{12} & 0 & A_{13} \\ A_{21} & A_{22} & 0 & A_{23} \\ A_{21} & 0 & A_{22} & A_{23} \\ A_{31} & 0 & A_{32} & A_{33} \end{bmatrix} \begin{bmatrix} \tilde{x}_1 \\ \tilde{x}_2 \end{bmatrix} \\ &+ \begin{bmatrix} B_{11} & 0 & 0 & 0 \\ 0 & B_{22} & 0 & 0 \\ 0 & 0 & B_{22} & 0 \\ 0 & 0 & 0 & B_{33} \end{bmatrix} \begin{bmatrix} \tilde{u}_1 \\ \tilde{u}_2 \end{bmatrix}\end{aligned} \tag{9.34}$$

where $\tilde{x}_1 = (x_1^T, x_2^T)^T, \tilde{x}_2 = (x_2^T, x_3^T)^T, \tilde{u}_1 = (u_1^T, u_2^T)^T, \tilde{u}_2 = (u_2^T, u_3^T)^T$. The complementary matrices are

$$\begin{aligned} M &= \begin{bmatrix} 0 & A_{12}/2 & -A_{12}/2 & 0 \\ 0 & A_{22}/2 & -A_{22}/2 & 0 \\ 0 & -A_{22}/2 & A_{22}/2 & 0 \\ 0 & -A_{32}/2 & A_{32}/2 & 0 \end{bmatrix} \\ N &= \begin{bmatrix} 0 & 0 & 0 & 0 \\ 0 & B_{22}/2 & -B_{22}/2 & 0 \\ 0 & -B_{22}/2 & B_{22}/2 & 0 \\ 0 & 0 & 0 & 0 \end{bmatrix} \\ L &= \begin{bmatrix} 0 & 0 & 0 & 0 \\ 0 & I_{n_2}/2 & -I_{n_2}/2 & 0 \\ 0 & -I_{n_2}/2 & I_{n_2}/2 & 0 \\ 0 & 0 & 0 & 0 \end{bmatrix} \end{aligned} \tag{9.35}$$

The decentralized state feedback is

$$\begin{bmatrix} \tilde{u}_1 \\ \tilde{u}_2 \end{bmatrix} = \begin{bmatrix} {k_{11}}^1 & {k_{12}}^1 & 0 & 0 \\ {k_{21}}^1 & {k_{22}}^1 & 0 & 0 \\ 0 & 0 & {k_{11}}^2 & {k_{12}}^2 \\ 0 & 0 & {k_{21}}^2 & {k_{22}}^2 \end{bmatrix} \begin{bmatrix} \tilde{x}_1 \\ \tilde{x}_2 \end{bmatrix} \tag{9.36}$$

The above control law is decentralized, but is not contractible for implementation in the

original system $\mathbb{S}$. For that reason, we have to modify (9.36) so that

$$\begin{bmatrix} \tilde{u}_1 \\ \tilde{u}_2 \end{bmatrix} = \begin{bmatrix} {k_{11}}^1 & {k_{12}}^1 & 0 & 0 \\ {k_{21}}^1 & ({k_{22}}^1 + {k_{11}}^2)/2 & 0 & {k_{12}}^2 \\ {k_{21}}^1 & 0 & ({k_{22}}^1 + {k_{11}}^2)/2 & {k_{12}}^2 \\ 0 & 0 & {k_{21}}^2 & {k_{22}}^2 \end{bmatrix} \begin{bmatrix} \tilde{x}_1 \\ \tilde{x}_2 \end{bmatrix} \tag{9.37}$$

This modification is motivated by the requirement that the m_2-dim component u_2 of $\tilde{u}_1$ has to be identical to the m_2-dim component u_2 of $\tilde{u}_2$. The overall system with the state feedback now can be described as

$$\begin{aligned} \dot{\tilde{x}} &= (\tilde{A} + \tilde{B}\tilde{K})\tilde{x} \\ &= \begin{bmatrix} A_{11} + B_{11}{k_{11}}^1 & A_{12} + B_{12}{k_{12}}^1 & 0 & 0 \\ A_{21} + B_{21}{k_{21}}^1 & A_{22} + B_{22}{k_{22}}^1 & 0 & 0 \\ 0 & 0 & A_{22} + B_{22}{k_{11}}^2 & A_{23} + B_{23}{k_{12}}^2 \\ 0 & 0 & A_{32} + B_{32}{k_{21}}^2 & A_{33} + B_{33}{k_{22}}^2 \end{bmatrix} \tilde{x} + \\ &\quad \begin{bmatrix} 0 & 0 & 0 & A_{13} \\ 0 & \frac{B_{22}({k_{11}}^2 - {k_{22}}^1)}{2} & 0 & A_{23} + B_{22}{k_{12}}^2 \\ A_{21} + B_{22}{k_{21}}^1 & 0 & \frac{B_{22}({k_{11}}^2 - {k_{22}}^1)}{2} & 0 \\ A_{31} & 0 & 0 & 0 \end{bmatrix} \tilde{x} \end{aligned} \tag{9.38}$$

Let's rewrite the above equation in the following way:

$$\begin{bmatrix} \dot{\tilde{x}}_1 \\ \dot{\tilde{x}}_2 \end{bmatrix} = \begin{bmatrix} \tilde{A}_1 & 0 \\ 0 & \tilde{A}_2 \end{bmatrix} \begin{bmatrix} \tilde{x}_1 \\ \tilde{x}_2 \end{bmatrix} + \begin{bmatrix} \tilde{M}_{11} & \tilde{M}_{12} \\ \tilde{M}_{21} & \tilde{M}_{22} \end{bmatrix} \begin{bmatrix} \tilde{x}_1 \\ \tilde{x}_2 \end{bmatrix} \tag{9.39}$$

where

$$\begin{aligned} \tilde{A}_1 &= \begin{bmatrix} A_{11} + B_{11}{k_{11}}^1 & A_{12} + B_{12}{k_{12}}^1 \\ A_{21} + B_{21}{k_{21}}^1 & A_{22} + B_{22}{k_{22}}^1 \end{bmatrix} \\ \tilde{A}_2 &= \begin{bmatrix} A_{22} + B_{22}{k_{11}}^2 & A_{23} + B_{23}{k_{12}}^2 \\ A_{32} + B_{32}{k_{21}}^2 & A_{33} + B_{33}{k_{22}}^2 \end{bmatrix} \\ \tilde{M}_{11} &= \begin{bmatrix} 0 & 0 \\ 0 & \frac{B_{22}({k_{11}}^2 - {k_{22}}^1)}{2} \end{bmatrix}, \qquad \tilde{M}_{12} = \begin{bmatrix} 0 & A_{13} \\ 0 & A_{23} + B_{22}{k_{12}}^2 \end{bmatrix} \\ \tilde{M}_{21} &= \begin{bmatrix} A_{21} + B_{22}{k_{21}}^1 & 0 \\ A_{31} & 0 \end{bmatrix}, \qquad \tilde{M}_{22} = \begin{bmatrix} \frac{B_{22}({k_{11}}^2 - {k_{22}}^1)}{2} & 0 \\ 0 & 0 \end{bmatrix} \end{aligned} \tag{9.40}$$

Since system $\dot{\tilde{x}}_i = \tilde{A}_i\tilde{x}_i$, for $i = 1, 2$ is a stable system, there exists a positive definite

decrecent Lyapunov function $V_i(\tilde{x}_i)$ which satisfies

$$\dot{V}_i(\tilde{x}_i) = \frac{\partial V_i}{\partial \tilde{x}_i}\tilde{A}_i\tilde{x}_i \leq -\alpha_i\phi_i^2(\tilde{x}_i) \tag{9.41}$$

and suppose

$$\left\|\frac{\partial V_i}{\partial \tilde{x}_i}\right\| \leq \beta_i\phi_i(\tilde{x}_i) \tag{9.42}$$

for $\tilde{x} \in \mathcal{R}^{\tilde{n}}$ for some positive constants α_i and β_i, where ϕ_i are positive definite and continuous. Furthermore, suppose the interconnection terms satisfy the bound

$$\begin{aligned}\left\|\tilde{M}_{11}\tilde{x}_1 + \tilde{M}_{12}\tilde{x}_2\right\| &\leq \gamma_{11}\phi_1(\tilde{x}_1) + \gamma_{12}\phi_2(\tilde{x}_2)\\ \left\|\tilde{M}_{21}\tilde{x}_1 + \tilde{M}_{22}\tilde{x}_2\right\| &\leq \gamma_{21}\phi_1(\tilde{x}_1) + \gamma_{22}\phi_2(\tilde{x}_2)\end{aligned} \tag{9.43}$$

for all $\tilde{x} \in \mathcal{R}^{\tilde{n}}$ and for some nonnegative constants $\gamma_{ij}, i = 1, 2; j = 1, 2$.

Define matrix W as

$$\begin{aligned} w_{ij} &= \alpha_i - \beta_i\gamma_{ii}, \qquad if \quad i = j\\ w_{ij} &= -\beta_i\gamma_{ij}, \qquad if \quad i \neq j\end{aligned} \tag{9.44}$$

Then we have the following regarding the stability of the interconnected system.

Theorem 9.5 *The expanded closed-loop system is stable if matrix W is a M-matrix.*

Proof: Immediately following the Vector-Lyapunov method.

Here the key feature is that the interconnection terms contain the feedback gains. In case of high gains, it may fail to prove the stability of the expanded system. When the stability of the expanded system is established, the original closed-loop system stability is guaranteed by theorem 3.1.4.

9.3 Overlapping Decentralization With Direct Nonlinear Control

Consider the nonlinear system

$$\dot{x} = f(x, u) \tag{9.45}$$

where $f(0, 0) = 0$ and $f(x, u)$ is contionuously differentiable in a domain $D_x \times D_u$ with $x(t) \in \mathcal{R}^n$, $u(t) \in \mathcal{R}^m$ that contains the origin $(x = 0, u = 0)$. Furthermore, system (9.45) is

assumed to have the following overlapping dynamics

$$\begin{aligned}\dot{x}_1 &= f_1(x_1) + g_1(x_1)u_1 + h_{1,2}(x_1, x_2) + h_1(x)\\ \dot{x}_2 &= f_2(x_2) + g_2(x_2)u_2 + h_{2,1}(x_1, x_2) + h_{2,3}(x_2, x_3) + h_2(x)\\ \dot{x}_3 &= f_3(x_3) + g_3(x_3)u_3 + h_{3,2}(x_2, x_3) + h_3(x)\end{aligned} \tag{9.46}$$

where $h_{1,2}(x_1, x_2), h_1(x), h_{2,1}(x_1, x_2), h_{2,3}(x_2, x_3), h_2(x), h_{3,2}(x_2, x_3), h_3(x)$ are the interconnections. We want to design the control $u_i, i = 1, 2, 3$ to stabilize the system.

First we decompose the system in (9.46) into two overlapped subsystems, $\mathbb{S}_{\not\in}$:

$$\begin{aligned}\dot{x}_1 &= f_1(x_1) + g_1(x_1){u_1}^1 + h_{1,2}(x_1, x_2)\\ \dot{x}_2 &= f_2(x_2) + g_2(x_2){u_2}^1 + h_{2,1}(x_1, x_2)\end{aligned} \tag{9.47}$$

and $\mathbb{S}_{\not\ni}$:

$$\begin{aligned}\dot{x}_2 &= f_2(x_2) + g_2(x_2){u_2}^2 + h_{2,3}(x_2, x_3)\\ \dot{x}_3 &= f_3(x_3) + g_3(x_3){u_3}^2 + h_{3,2}(x_2, x_3)\end{aligned} \tag{9.48}$$

Suppose the control laws ${u_1}^1 = {u_1}^1(x_1, x_2)$, ${u_2}^1 = {u_2}^1(x_1, x_2)$ for $\mathbb{S}_{\not\in}$ and ${u_2}^2 = {u_2}^2(x_2, x_3)$, ${u_3}^2 = {u_3}^2(x_2, x_3)$ for $\mathbb{S}_{\not\ni}$ are continuously differentiable in a domain $D_x \subset \mathcal{R}^n$ that contains the origin $(x_1 = 0, x_2 = 0, x_3 = 0)$. Furthermore there exist positive definite decrecent Lyapunov functions $V_1(x_1, x_2)$ and $V_2(x_2, x_3)$ which satisfy

$$\begin{aligned}\dot{V}_1(x_1, x_2) &\leq -\alpha_1\phi_1^2(x_1, x_2)\\ \dot{V}_2(x_2, x_3) &\leq -\alpha_2\phi_2^2(x_2, x_3)\end{aligned} \tag{9.49}$$

and suppose

$$\left\| \begin{matrix} \frac{\partial V_1}{\partial x_1} \\ \frac{\partial V_1}{\partial x_2} \end{matrix} \right\| \leq \beta_1\phi_1(x_1, x_2), \qquad \left\| \begin{matrix} \frac{\partial V_2}{\partial x_2} \\ \frac{\partial V_2}{\partial x_3} \end{matrix} \right\| \leq \beta_2\phi_2(x_2, x_3) \tag{9.50}$$

for $x \in \mathcal{R}^n$ for some positive constants α_i and β_i, where ϕ_i are positive definite and continuous.

For the implementation, let us choose the following control law for the original system (9.46)

$$\begin{aligned}u_1 &= {u_1}^1(x_1, x_2)\\ u_2 &= {u_2}^1(x_1, x_2) + {u_2}^2(x_2, x_3)\\ u_3 &= {u_3}^2(x_2, x_3)\end{aligned} \tag{9.51}$$

and the function

$$V(x_1, x_2, x_3) = d_1 V_1(x_1, x_2) + d_2 V_2(x_2, x_3) \tag{9.52}$$

be a composite Lyapunov function for the overall system for all values of the positive constants d_1, d_2. The derivative of $V(x_1, x_2, x_3)$ along the trajectories of (9.46) is given by

$$\begin{aligned}
\dot{V}(x_1, x_2, x_3) = d_1\{&\frac{\partial V_1}{\partial x_1}[f_1(x_1) + g_1(x_1){u_1}^1(x_1, x_2) + h_{1,2}(x_1, x_2)] \\
&+\frac{\partial V_1}{\partial x_2}[f_2(x_2) + g_2(x_2){u_2}^1(x_1, x_2) + h_{2,1}(x_1, x_2)] \\
+\frac{\partial V_1}{\partial x_1}h_1(x) + &\frac{\partial V_1}{\partial x_2}[g_2(x_2){u_2}^2(x_2, x_3) + h_{2,3}(x_2, x_3) + h_2(x)]\} \\
&+d_2\{\frac{\partial V_2}{\partial x_2} + [f_2(x_2) + g_2(x_2){u_2}^2(x_2, x_3) + h_{2,3}(x_2, x_3)] \\
&+\frac{\partial V_2}{\partial x_3}[f_3(x_3) + g_3(x_3){u_3}^2(x_2, x_3) + h_{3,2}(x_2, x_3)] \\
+\frac{\partial V_2}{\partial x_3}h_3(x) + &\frac{\partial V_2}{\partial x_2}[g_2(x_2){u_2}^1(x_1, x_2) + h_{2,1}(x_1, x_2) + h_2(x)]\}
\end{aligned} \tag{9.53}$$

Therefore, $V(x_1, x_2, x_3)$ satisfies

$$\begin{aligned}
\dot{V}(x_1, x_2, x_3) = d_1\{&-\alpha_1\phi_1(x_1, x_2) + \frac{\partial V_1}{\partial x_1}h_1(x) \\
+\frac{\partial V_1}{\partial x_2}&[g_2(x_2){u_2}^2(x_2, x_3) + h_{2,3}(x_2, x_3) + h_2(x)]\} \\
&+d_2\{-\alpha_2\phi_2(x_2, x_3) + \frac{\partial V_2}{\partial x_3}h_3(x) \\
+\frac{\partial V_2}{\partial x_2}&[g_2(x_2){u_2}^1(x_1, x_2) + h_{2,1}(x_1, x_2) + h_2(x)]\}
\end{aligned} \tag{9.54}$$

Furthermore, suppose the interconnection terms together with the controls satisfy the bound

$$\begin{aligned}
\left\| \begin{array}{c} h_1(x) \\ g_2(x_2){u_2}^2(x_2, x_3) + h_{2,3}(x_2, x_3) + h_2(x) \end{array} \right\| &\leq \gamma_{11}\phi_1 + \gamma_{12}\phi_2 \\
\left\| \begin{array}{c} g_2(x_2){u_2}^1(x_1, x_2) + h_{2,1}(x_1, x_2) + h_2(x) \\ h_3(x) \end{array} \right\| &\leq \gamma_{21}\phi_1 + \gamma_{22}\phi_2
\end{aligned} \tag{9.55}$$

for all $x \in \mathcal{R}^n$ and for some nonnegative constants $\gamma_{ij}, i = 1, 2; j = 1, 2$. Define matrix W as

$$\begin{aligned}
w_{ij} &= \alpha_i - \beta_i\gamma_{ii}, \qquad if \quad i = j \\
w_{ij} &= -\beta_i\gamma_{ij}, \qquad if \quad i \neq j
\end{aligned} \tag{9.56}$$

Then we have the following regarding the stability of the interconnected system (9.46).

Theorem 9.6 *The expanded closed-loop system is stable with the overlapping decentralized control law in (9.51) if matrix W is a M-matrix.*

Proof: Immediately following the Vector-Lyapunov method.

Let's consider the following example:

$$\begin{aligned} \dot{x}_1 &= x_1^3 + u_1 + x_1x_2 + 0.1x_1x_2x_3 \\ \dot{x}_2 &= x_2^3 + u_2 + x_1x_2 + x_2x_3 + 0.1x_1x_2x_3 \\ \dot{x}_3 &= x_3^3 + u_3 + x_2x_3 + 0.1x_1x_2x_3 \end{aligned} \tag{9.57}$$

The original system is decomposed into two overlapped subsystems, $\mathbb{S}_{\not\in}$

$$\begin{aligned} \dot{x}_1 &= x_1^3 + {u_1}^1 + x_1x_2 \\ \dot{x}_2 &= x_2^3 + {u_2}^1 + x_1x_2 \end{aligned} \tag{9.58}$$

with the control law for $\mathbb{S}_{\not\in}$

$$\begin{aligned} {u_1}^1(x_1, x_2) &= -a_1x_1 - x_1^3 - x_1x_2 \\ {u_2}^1(x_1, x_2) &= -{a_2}^1x_2 - x_2^3 - x_1x_2 \end{aligned} \tag{9.59}$$

and subsystem $\mathbb{S}_{\not\in}$

$$\begin{aligned} \dot{x}_2 &= x_2^3 + {u_2}^2 + x_2x_3 \\ \dot{x}_3 &= x_3^3 + {u_3}^2 + x_2x_3 \end{aligned} \tag{9.60}$$

with the control law for $\mathbb{S}_{\not\in}$

$$\begin{aligned} {u_2}^2(x_2, x_3) &= -{a_2}^2x_2 - x_2^3 - x_2x_3 \\ {u_3}^2(x_2, x_3) &= -a_3x_3 - x_3^3 - x_2x_3 \end{aligned} \tag{9.61}$$

Let

$$V_1(x_1, x_2) = \frac{1}{2}(x_1^2 + x_2^2), \quad V_2(x_2, x_3) = \frac{1}{2}(x_2^2 + x_3^2) \tag{9.62}$$

be the Lyapunov functions of $\mathbb{S}_{\not\in}$ and $\mathbb{S}_{\not\in}$ respectively. Therefore we have

$$\begin{aligned} \dot{V}_1 &= -(a_1x_1^2 + {a_2}^1x_2^2) \leq -\min(a_1, {a_2}^1)(x_1^2 + x_2^2) = -\alpha_1\phi_1^2 \\ \left\| \begin{array}{c} \frac{\partial V_1}{\partial x_1} \\ \frac{\partial V_1}{\partial x_2} \end{array} \right\| &= \left\| \begin{array}{c} x_1 \\ x_2 \end{array} \right\| \leq (x_1^2 + x_2^2)^{1/2} \end{aligned} \tag{9.63}$$

where

$$\alpha_1 = \min(a_1, {a_2}^1), \qquad \beta_1 = 1, \quad \phi_1(x_1, x_2) = (x_1^2 + x_2^2)^{1/2}$$

and

$$\begin{aligned} \dot{V}_2 &= -(a_3 x_3^2 + {a_2}^3 x_2^2) \le -\min(a_3, {a_2}^3)(x_3^2 + x_2^2) = -\alpha_2 \phi_2^2 \\ \left\| \begin{array}{c} \frac{\partial V_2}{\partial x_2} \\ \frac{\partial V_2}{\partial x_3} \end{array} \right\| &= \left\| \begin{array}{c} x_2 \\ x_3 \end{array} \right\| \le (x_3^2 + x_2^2)^{1/2} \end{aligned} \tag{9.64}$$

where

$$\alpha_2 = \min(a_3, {a_2}^2), \qquad \beta_2 = 1, \quad \phi_2(x_2, x_3) = (x_3^2 + x_2^2)^{1/2}$$

We also have

$$\begin{aligned} \left\| \begin{array}{c} 0.1 x_1 x_2 x_3 \\ -{a_2}^2 x_2 - x_2^3 + 0.1 x_1 x_2 x_3 \end{array} \right\| &\le \|({a_2}^2 + 1.2) x_2\| \le \gamma_{11}\phi_1 + \gamma_{12}\phi_2 \\ \left\| \begin{array}{c} -{a_2}^1 x_2 - x_2^3 + 0.1 x_1 x_2 x_3 \\ 0.1 x_1 x_2 x_3 \end{array} \right\| &\le \|({a_2}^1 + 1.2) x_2\| \le \gamma_{11}\phi_1 + \gamma_{12}\phi_2 \end{aligned}$$

for $|x_1| \le 1$, $|x_2| \le 1$, and $|x_3| \le 1$, where

$$\begin{aligned} \gamma_{11} &= p_1({a_2}^2 + 1.2), \quad \gamma_{12} = (1 - p_1)({a_2}^2 + 1.2) \\ \gamma_{21} &= p_2({a_2}^1 + 1.2), \quad \gamma_{22} = (1 - p_2)({a_2}^1 + 1.2) \end{aligned} \tag{9.65}$$

with $0 \le p_1 \le 1, 0 \le p_2 \le 1$. Then the element of W matrix is

$$\begin{aligned} w_{11} &= \alpha_1 - \beta_1\gamma_{11} = \min(a_1, {a_2}^1) - p_1({a_2}^2 + 1.2) \\ w_{12} &= -\beta_1\gamma_{12} = -(1 - p_1)({a_2}^2 + 1.2) \\ w_{21} &= -\beta_2\gamma_{21} = -p_2({a_2}^1 + 1.2) \\ w_{22} &= \alpha_2 - \beta_2\gamma_{22} = \min(a_3, {a_2}^2) - (1 - p_2)({a_2}^1 + 1.2) \end{aligned} \tag{9.66}$$

Therefore the choice of $a_1 = 3, a_3 = 3, {a_2}^1 = 2, {a_2}^2 = 2, p_1 = 1, p_2 = 0$ will make matrix W a M matrix. Therefore the control law in (9.51) will stabilize the system (9.57) in the region $|x_1| \le 1$, $|x_2| \le 1$, and $|x_3| \le 1$.

Chapter 10

Decentralized Reconfiguration control for Large Scale Systems with Application to the Segmented Telescope Test-Bed

A decentralized reconfiguration control *DRC* system is designed and analyzed for a class of large-scale systems. The objective of the *DRC* system is to meet the performance requirements under normal and failure situations. The objective is accomplished by integrating three schemes: nominal controller, fault detection and isolation, and re-configurable control schemes. These schemes have a decentralized structure for the reason that the implementation of a centralized reconfiguration control system for large-scale systems is usually not feasible with existing digital signal processors. However, with a decentralized approach the feasibility of real-time implementation can be achieved by dividing the total task of the reconfiguration control system into a number of smaller tasks implemented by a number of processors working in parallel. The proposed design is implemented in real time on a segmented telescope test-bed, and demonstrated to meet the performance requirements in the presence of sensor failures.

10.1 Introduction

The design of fault-tolerant control systems is one of the most important issues for highly critical systems such as nuclear power stations, chemical plants, aircrafts, and spacecrafts. In fact, fault-tolerant control system is used to improve system reliability, maintainability, and survivability by completing a task after failure, increasing maintenance time, and preventing damages, respectively. Most control systems are designed to meet performance

requirements in the presence of small modeling errors, noise, and disturbances. In many cases these robust control systems can not guarantee closed-loop stability or performance in the presence of faults. The inability of robust control systems to accommodate faults has motivated researchers to design controllers with the ability to tolerate predetermined faults. These controllers are known as reliable controllers or passive fault-tolerant controllers where fault tolerance is achieved using a single controller with fixed structure and parameters. Methods for passive fault-tolerant control include for example: LQG control [52], observer-based control with H_∞ norm bound [53], decentralized observer-based control with H_∞ norm bound [54], and H_∞ control [55]. This approach of fault tolerance has many disadvantages for instance: a) it is limited to specific types of faults like outage, bias, and gain changing, b) it can tolerate a pre-selected set of sensors or actuators failures, and c) it degrades system performances in order to achieve fault tolerance. Therefore, another class of control system designs that can tolerate various types of faults at the same time maintain acceptable level of performance is considered especially for systems where failures can lead to human death/injury or heavy cost. These control systems are called active fault-tolerant control systems and their structure or parameters or both can be changed on-line to accommodate failures. The key element for achieving active fault tolerance is system redundancies. Redundancies can be provided by: Hardware (physical redundancies), software (analytical redundancies), or both hardware and software. One method of sensor fault tolerance using the physical redundancy approach is to have a number of redundant sensors operating in parallel with system sensors and voters are used to determine which sensor is failed and should be taken out of service. Generally speaking, n sensors measuring a quantity can be used to tolerate $(n-1)/2$ failed sensors. One practical example of using redundant sensors for sensor fault tolerance is an electro-mechanical brake pedal system [56]. Four position sensors are used to sense the movement of the brake pedal and two voters are used to detect a sensor fault and remove a faulty sensor from the electro-mechanical brake pedal system. The physical redundancy approach for sensor fault tolerance is straightforward and most likely has better performance than analytical redundancy approach especially for reducing the risk of false alarms. However, the cost and space are the main limitations for applying the physical redundancy approach. The analytical redundancy approach is attractive for fault tolerance when redundancies can be generated by mathematical functions in software. Following this approach one can reduce the cost of additional hardware and overcome the problem of space limitation but with expensive of computational complexity and some possible performance degradation. In the last decade, the subject of active fault-tolerant control system has drawn a lot of attention from researchers; see for example [57]- [62]. A good survey on fault-tolerant control systems is written by Patton [63]. For concepts and methods in fault-tolerant control one can refer to [64]. Below we discussed some of the techniques proposed in literatures for sensor fault tolerance using the analytical redundancy approach.

- *Multiple observers with sensor fault detection and isolation (SFDI) scheme* [65]: In this case, n number of state observers are used to estimate n redundant state vectors where n is the number of sensors. Each observer is driven by one sensor output and all actuator inputs to generate the estimate of one redundant state vector. A faulty sensor is identified by a detection logic that operates on the n state vectors and one healthy redundant state vector selected by the detection logic to be used by the feedback controller. This approach may not be feasible for large order systems with many sensors. Because n redundant state vectors must be estimated leading to computationally complex calculation when the order of the system is high and n is large. Also, the question of accurate state estimation in the presence of disturbances needs to be considered.

- *Multiple observers using majority rule* [66]: This approach also uses multiple observers but without *SFDI* scheme. For a state feedback controlled system, the system outputs are divided into three sets where each output belongs to only one set. Three observers are used to estimate three redundant state vectors where each observer is driven by all actuator inputs and one set of sensor outputs. Based on a decision by majority rule, which is an extension of the scalar case where a middle value of a scalar function is adopted at time t, one estimated state vector is selected at time t for use by the state feedback controller. In general this method cannot identify a faulty sensor and the possibility to adopt an estimated state vector generated by a faulty sensor is possible.

- *Pre-computed controllers with SFDI* [67]: A number of controllers with a switching logic are used to select the right controller in the presence of sensor faults. In this case, each controller is designed off line by taking into account a faulty sensor. When a sensor fails, a *SFDI* scheme identifies the faulty sensor and the switching logic selects one controller designed for that particular faulty sensor case. This method assumes that the system remains observable with the remaining healthy sensors.

- *Neural networks* [68]- [70]: In this case, neural networks are used to generate the model of the system instead of state observers. For example in [70], neural networks are used to tolerate sensor faults in outdoor ventilation control unit. Three neural networks are trained to predict the measurements of three airflow sensors that are used in a control unit. The difference between a sensor reading and its predicted reading generated by the neural network is used to detect a sensor fault and identify the faulty sensor. For sensor fault tolerance, the faulty sensor reading is replaced with its estimated value from the neural network. Many questions are raised in this approach, such as: how to select the structure of the neural network, the complexity of the neural network structure, and the time needed for estimation.

- *Fault estimation and control reconfiguration* [71]: A *SFDI* scheme is used to identify the location of the faulty sensor, estimate its magnitude, and use it to modify the control

law by adding a new compensating term to it. In order to achieve sensor fault tolerance, this method requires sensor fault magnitudes and estimation of these values requires heavy computational operations for a large order system with many sensors. Also, the accuracy of the estimated sensor fault magnitude could be affected by disturbances.

Most of the above techniques require *SFDI* in order to achieve sensor fault tolerance. The main task of the *SFDI* scheme is to detect a sensor fault and identify its location. Several fault detection and isolation (*FDI*) design methods (mostly for sensor/actuator faults) have been proposed in the last three decades. Examples of well-known methods are: state estimation ([72]- [74]), parity equations ([75]- [77]), parameter estimation [78], and neural network approach ([79]- [82]). For a good survey in *FDI* methods, see [83] and for comparison of different methods of *FDI*, see [84]. A lot of work have been done to enhance the performance of *FDI* schemes in the presence of modeling errors, disturbances, and noise. The objective in robust FDI is to increase the sensitivity of fault indication signals (residuals) for specific faults and at the same time reduce the sensitivity of the fault indication signals in the absence of these faults. Some of the propsed methods for robust *FDI* include the use of: robust observer ([85]- [87]), robust parity equations ([88]- [90]), and frequency-domain optimization ([91]- [93]). For more details on robust *FDI*, see [94], and [95].

In this chapter, we consider the design and analysis of a decentralized reconfiguration control *DRC* system for a class of large-scale systems. We restrict the reconfiguration control system to have a decentralized structure in order to reduce computational complexity. We show that sensor faults can be detected, isolated and the decentralized control schemes can be reconfigured on-line in order to accommodate sensor faults. The proposed design is demonstrated in real time by implementing it on the segmented telescope test-bed, which consists of 6-segments giving an overall high order system.

10.2 Large Scale System

A wide class of large-scale systems can be modeled as

$$\dot{x}(t) = A\,x(t) + B\,u(t) \tag{10.1}$$

$$y(t) = C\,x(t) \tag{10.2}$$

where $y \in R^{n_y}$ is the measured output vector, $u \in R^{n_u}$ is the input vector, $x \in R^{n_x}$ is the state vector, and A, B, and C are constant matrices of appropriate dimensions. In the input-output transfer function matrix the equations (10.1 and 10.2) take the form

$$y = G(s)\,u,\;\; G(s) = C(sI - A)^{-1}B \tag{10.3}$$

where

$$G(s) = \begin{bmatrix} G_{11}(s) & \dots & G_{1N}(s) \\ \vdots & \ddots & \vdots \\ G_{N1}(s) & \dots & G_{NN}(s) \end{bmatrix} \tag{10.4}$$

is the overall transfer matrix. The (10.3) can be expressed as

$$y_i(s) \;=\; G_{ii}(s)\, u_i(s) \;+\; \sum_{\substack{j=1 \\ j \neq i}}^{N} G_{ij}(s)\, u_j(s) \qquad\qquad i \;=\; 1,\, 2,\, ...,\, N \tag{10.5}$$

where $y_i \in R^{n_{y_i}}$, $u_i \in R^{n_{u_i}}$ is the output and input vectors of the $i-th$ subsystem, $G_{ii}(s) \in C^{n_{y_i} \times\, n_{u_i}}$, and $G_{ij}(s) \in C^{n_{y_i} \times\, n_{u_j}}$ represents the interconnection transfer function matrix between subsystems i *and* j. The state space representation of (10.5) with the interconnections shown separately is given by

$$\begin{aligned} \dot{x}_i(t) \;&=\; A_i\, x_i(t) \;+\; B_i\, u_i(t) \;+\; d_i(t) \\ y_i(t) \;&=\; C_i\, x_i(t) \qquad\qquad\qquad\qquad\qquad\qquad i \;=\; 1,\, 2,\, ...,\, N \end{aligned} \tag{10.6}$$

where

$G_{ii}(s) := C_i(sI - A_i)^{-1}B_i$, and $\displaystyle\sum_{\substack{j=1 \\ j \neq i}}^{N} G_{ij}(s)\, u_j(s) := C_i(sI - A_i)^{-1}d_i(s)$.

In this paper we consider both models (10.1 and 10.2), and (10.6) to design a decentralized reconfiguration control system that guarantees performance in the presence of sensor faults. In order to reduce the dimensionality of the control reconfiguration system the interconnections d_i in (10.6) are considered as disturbances whose effects are minimized in the design of the reconfiguration control system.

10.3 Structure of the decentralized reconfiguration control (DRC) system

For a wide class of large scale systems the model order and the number of sensors and actuators are large. The number of computational operations needed to implement a reconfiguration control system scheme for such systems is large and often exceeds the processing limits of available digital signal processors. The design of an efficient reconfiguration con-

trol system that guarantees system performance in normal and failure situations and at the same time its algorithm can be implemented in real time with available processors is often a challenging problem in large scale systems. One possible way of designing reconfiguration controllers for large-scale systems is to consider a decentralized approach. Where the system is divided into subsystems and a number of local reconfiguration control systems are designed for each subsystem. Although the decentralized approach reduces the number of computations and makes real-time implementation easier, it may affect stability and robustness of the overall closed-loop system systems.
In this chapter, we proposed a DRC system for large-scale systems. The large scale system consists of N subsystems with N local input/output vectors. Each local input and output vector generated by a number of actuators and sensors, respectively. N local reconfiguration control systems are designed for the N subsystems. Fig 10.1 shows the structure of the proposed DRC system.

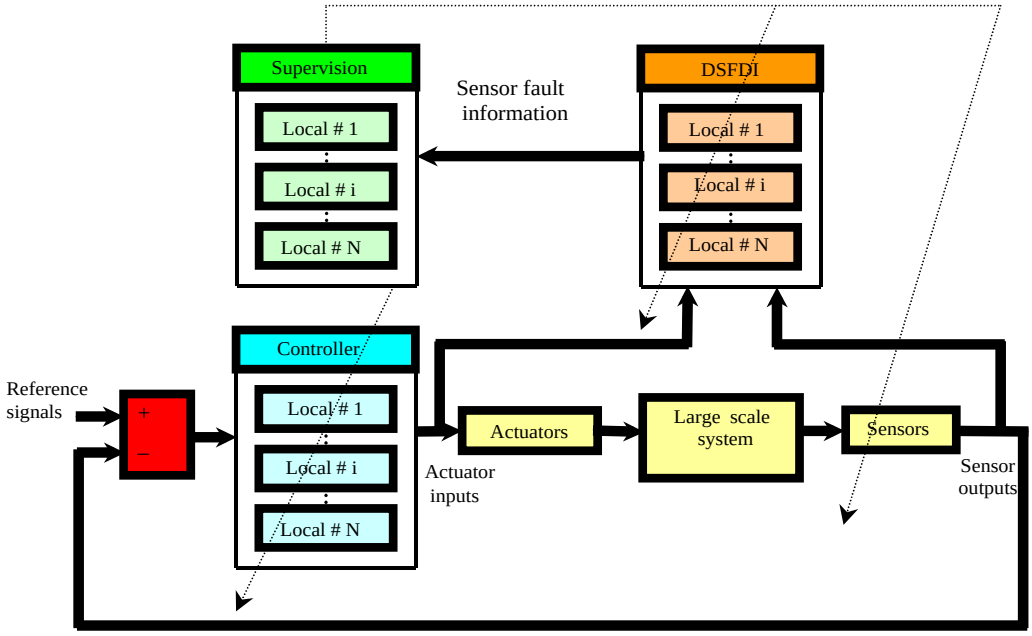

Figure 10.1: The structure of the DRC system

Local sensor fault detection and isolation units are detect local sensor faults and identify their location. Two types of signals are provided to each local fault detection and isolation unit: local actuator input and sensor output signals. Based on the information provided by

the local fault detection and isolation unit, the corresponding local supervision unit isolates the faulty sensor from the control path, selects a new set of sensors, replaces the existing local controller with a new local controller, and restructures the local fault detection and isolation unit for continuous subsystem monitoring.

In the following sections, the three main parts of the DRC system shown in Fig 10.1 are described in more details.

10.3.1 Decentralized control system design

Most of the existing controllers like H_∞ control and LQG control cannot be directly applied in reality to large-scale systems due to processor limitations. A reduced order controller that is one way to overcome the problem of processor limitations. If the reduced order controller still cannot be implemented and no further reduction can be achieved, one can choose a decentralized approach where a number of less complex controllers (called local controllers) are designed to control the overall system.

In this section, we present the developed decentralized direct adaptive output feedback ($DDAOF$) controller that has two features. The first one, is the simplicity of the decentralized controller since its has a small order independent of system model order, the second feature is the stability of closed-loop system can be ensured without tuning the local controllers. The stability is ensured because the local controllers are designed using the overall model. The decentralized controller is briefly introduced here, for more details see chapter 7. Fig 10.2 shows the proposed $DDAOF$ for a large-scale system.

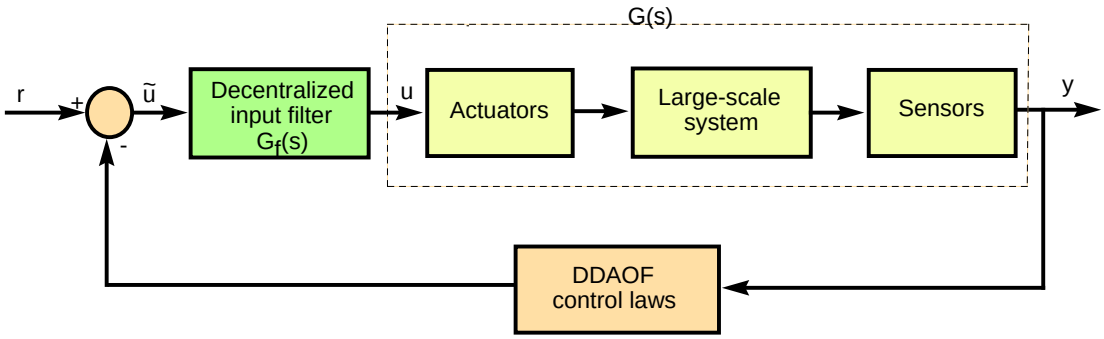

Figure 10.2: Large-scale system with DDAOF control

The N local adaptive control laws are computed as:

$$u_i = G_{f_i}(s)\,\tilde{u}_i \qquad i = 1, 2, ..., N \tag{10.7}$$

$$\tilde{u}_i(t) = -\frac{k_i(t) + l_i(t)}{1 + \delta\,(k_i(t) + l_i(t))}\, y_i(t) \tag{10.8}$$

$$k_i(t) = \alpha_i y_i^T(t) y_i(t) \tag{10.9}$$

$$\dot{l}_i(t) = \beta_i y_i^T(t) y_i(t) \tag{10.10}$$

The $k_i \in R$, $l_i \in R$, and $\delta, \alpha_i, \beta_i$ are design positive constants. The filter $G_f(s)$ and scalar δ are designed such that $G(s)G_f(s)+\delta I$ is strictly positive real. It was shown in chapter 7, these control laws stabilize the closed loop system and bring the system states to zero asymptotically.

10.3.2 Decentralized sensor fault detection and isolation (DSFDI)

The objective of the $DSFDI$ is to detect the sensor fault (fault detection) and to identify the location of the faulty sensor (fault isolation). In this section, the design of $DSFDI$ based on the parity equations method is presented. The $DSFDI$ scheme consists of N local units where each local unit is responsible for sensor fault detection and isolation in the corresponding subsystem. Each of the N local units consists of n_{y_i} banks of residual generators where each bank is driven by all local inputs and one local output. Fig 10.3 shows the $i-th$ local unit of the $DSFDI$.

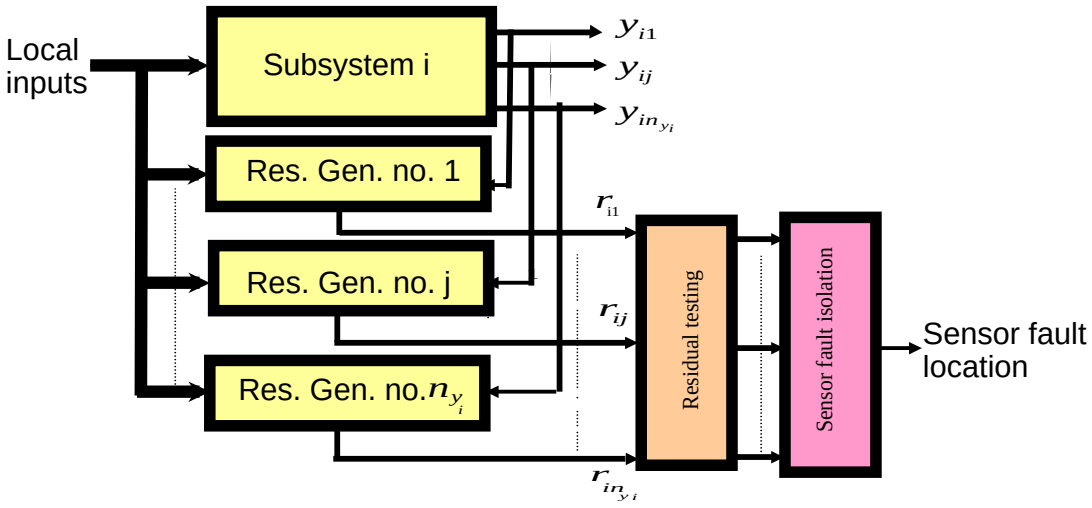

Figure 10.3: The i-th local unit of sensor fault detection and isolation

The design steps of $DSFDI$ are:

- ***Sensor fault modeling:*** Many types of sensor faults can be occurred and they are usually described based on the fault time behavior and magnitude. For example: Sudden, slowly developing, intermittent, hard, or soft faults. Generally speaking, the sudden and hard faults must be detected early to prevent controlled system damages. While for slowly developing faults like drift faults, the detection time is longer because it is difficult to detect these types of faults early. On another hand, for the soft faults like small changing in a sensor gain the fault detection may be not necessary since in general the nominal control system can tolerate it. The effects of these different types of sensor faults on a system can be modeled as unknown vector (function of time) adding to the system output vector. In this case the state space equations (10.6) is written as

$$\begin{aligned} \dot{x}_i(t) &= A_i\, x_i(t) + B_i\, u_i(t) + d_i(t) \\ y_i(t) &= C_i\, x_i(t) + f_i(t) \qquad\qquad i = 1,\, 2,\, ...,\, N \end{aligned} \tag{10.11}$$

  Where $f_i(t) \in R^{n_{y_i}}$ is unknown sensor fault vector affecting the local sensor readings of the subsystem i. By modeling sensor faults as additive faults, many types of sensor faults can be expressed mathematically and also designing a fault detection scheme will be easier than the case of modeling sensor faults as multiplicative faults.

- ***Residuals generation:*** For each subsystem, n_{y_i} banks of residual generators where each one is driven by all local inputs and one local output are used to generate n_{y_i} sensor failure indication signals called residuals. These residuals are used to indicate any possible sensor failure and therefore the residuals should be close to zero when there is no sensor failure and different than zero in the presence of sensor failure. Each bank of residual generators is designed by using parity equations method and to design one bank of residual generator, consider the discrete version of the state space equations (10.11):

$$\begin{aligned} x_i(k+1) &= \tilde{A}_i\, x_i(k) + \tilde{B}_i\, u_i(k) + \tilde{d}_i(k) \\ y_i(k) &= \tilde{C}_i\, x_i(k) + \tilde{f}_i(k) \qquad\qquad i = 1,\, 2,\, ...,\, N \end{aligned} \tag{10.12}$$

  Also consider the $j-th$ sensor output of the subsystem i as:

$$y_{ij}(k) = \tilde{C}_{ij}\, x_i(k) + \tilde{f}_{ij}(k) \qquad i = 1,\, 2,\, ...,\, N \quad and \quad j = 1,\, 2,\, ...,\, n_{y_i} \tag{10.13}$$

  where $\tilde{C}_{ij}$ is the $j-th$ row of the matrix $\tilde{C}_i$, and $\tilde{f}_{ij}$ is the $j-th$ row of the sensor fault vector $\tilde{f}_i$. $\tilde{f}_i$. Now the $m+1$samples of the output y_{ij} can be written as:

$$Y_{ij} = \; L_{ij}\; x_i(k-m) \; + \; M_{ij}\; U_i + \; N_{ij}\; D_i + \; F_{ij} \tag{10.14}$$

where

$$Y_{ij} = \begin{bmatrix} y_{ij}(k-m) \\ y_{ij}(k-m+1) \\ \vdots \\ y_{ij}(k) \end{bmatrix}, \quad L_{ij} = \begin{bmatrix} \tilde{C}_{ij} \\ \tilde{C}_{ij}\tilde{A}_i \\ \vdots \\ \tilde{C}_{ij}\tilde{A}_i^m \end{bmatrix},$$

$$M_{ij} = \begin{bmatrix} 0 & 0 & \cdots & 0 \\ \tilde{C}_{ij}\tilde{B}_i & 0 & \cdots & 0 \\ \vdots & \vdots & \vdots & \vdots \\ \tilde{C}_{ij}\tilde{A}_i^{m-1}\tilde{B}_i & \tilde{C}_{ij}\tilde{A}_i^{m-2}\tilde{B}_i & \cdots \; \tilde{C}_{ij}\tilde{B}_i & 0 \end{bmatrix}, \; U_i = \begin{bmatrix} u_i(k-m) \\ u_i(k-m+1) \\ \vdots \\ u_i(k) \end{bmatrix},$$

$$N_{ij} = \begin{bmatrix} 0 & 0 & \cdots & 0 \\ \tilde{C}_{ij} & 0 & \cdots & 0 \\ \vdots & \vdots & \vdots & \vdots \\ \tilde{C}_{ij}\tilde{A}_i^{m-1} & \tilde{C}_{ij}\tilde{A}_i^{m-2} & \cdots \; \tilde{C}_{ij} & 0 \end{bmatrix}, \; D_i = \begin{bmatrix} \tilde{d}_i(k-m) \\ \tilde{d}_i(k-m+1) \\ \vdots \\ \tilde{d}_i(k) \end{bmatrix},$$

$$and \;\; F_{ij} = \begin{bmatrix} \tilde{f}_{ij}(k-m) \\ \tilde{f}_{ij}(k-m+1) \\ \vdots \\ \tilde{f}_{ij}(k) \end{bmatrix}$$

The $j-th$ residual of subsystem i is generated as:

$$r_{ij}(k) \; = \; V_{ij}^T \left[Y_{ij} - M_{ij} U_i \right] \tag{10.15}$$

where $V_{ij} \; \in \; R^{m+1}$ is the designed vector and m is the parity equations order to be selected. The vector V_{ij} is to be found such that the influences of the state vector and subsystem interactions on the residual r_{ij} are minimized at the same time the influence of sensor failure on the residual r_{ij} is maximized. To find such vector, the internal structure of the equation (10.15) is found by substituting equation (10.14) into (10.15) to get

$$r_{ij}(k) \;=\; V_{ij}^{T}\left[L_{ij}x(k-m) + N_{ij}D_i + F_{ij}\right] \tag{10.16}$$

It is clearly that the residual depends on the system state vector, the subsystem interactions, and sensor fault. To minimize the effects of state vector and subsystem interactions and to maximize the effect of sensor failure on the residual, the following performance index is minimized for V_{ij}

$$J_{ij} = \frac{\left\| V_{ij}^{T}\left[L_{ij}\vdots N_{ij}\right]\right\|_2^2}{\left\| V_{ij}^{T}\right\|_2^2} \tag{10.17}$$

where the optimal vector V_{ij} is found by using singular value decomposition.

- ***Residuals testing:*** Each residual is tested for the likelihood of sensor fault. A decision about existing a sensor failure is made by comparing the absolute value of the residual to a pre-selected threshold value. If the residual absolute value exceeds the threshold value, a sensor failure will be considered in the system. The threshold values can be selected from experiments to reduce false alarms coming from noise, modeling errors, subsystem interactions, and disturbances.

- ***Sensor fault isolation:*** The location of sensor failure location is the most important information required by the supervision system. For this reason, n_{y_i} banks of residual generators are used in each of the N local units of $DSFDI$ scheme. In this case, the n_{y_i} residuals will react differently to any number of sensors failed simultaneously. These different reactions (sensor failure codes) of the n_{y_i}residuals are used to find the location of faulty sensor(s).

10.3.3 Supervision system

The supervision system is used to integrate diagnostic information with switching controllers. In the subsystem i, each local controller is driven by n_{y_i} local sensor outputs and therefore n_{y_i} switching controllers are off-line designed for the n_{y_i} cases of faulty sensors. If one of the sensors is failed, one of the switching controllers will be activated based on the information provided by a local unit of $DSFDI$. In general, there are N local units of sensor fault detection and isolation and N local controllers with n_{y_i} switching controllers for each subsystem and they are integrated together through N supervision units. Each supervision

unit is locally responsible for:

- *Removing a failed sensor from the closed loop system*: The location of a faulty sensor, that is provided by a local unit of $DSFDI$, is supplied to the corresponding supervision unit for isolating the faulty sensor from the local closed loop system
- *Selecting a new set of sensors*: After the faulty sensor is removed from the closed loop system, the remaining healthy sensors (original plus redundant sensors) are used for controlling the subsystem.
- *Switching to a pre-designed controller*: Once the faulty sensor is removed from the feedback path and a new set of sensors is selected, a switching logic replaces the current local controller driven by a sensor fault with a pre-computed controller designed for that case of the failed sensor. The pre-computed controller is off-line designed for a new set of sensors assuming one sensor is failed at a time.
- *Restructuring a local-unit of* $DSFDI$: To continue monitoring the system after accommodating a sensor failure, the input signals (sensor measurement signals) to a local unit of $DSFDI$ are replaced with a new set of sensor output signals.

10.4 Real time implementation and experimental results

10.4.1 Real time implementation

Three digital signal processors are used to implement the proposed DRC algorithm. The three processors are running in parallel to handle the computational operations required for the DRC algorithm. The algorithm is written in $C++$ language and its flowchart is shown in Fig 10.4.

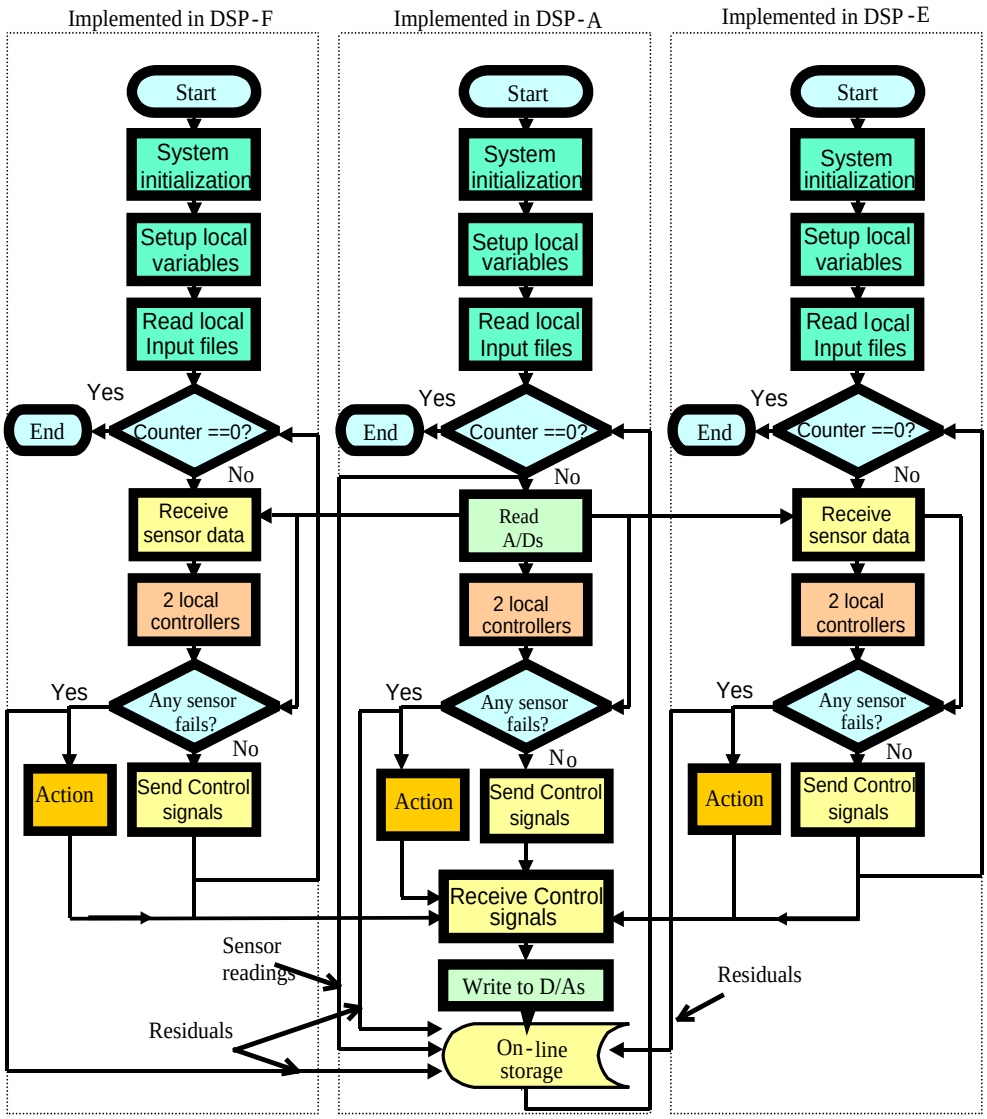

Figure 10.4: The flowchart of DSFTC algorithm

Each of the three digital signal processors is used to implement a part of *DRC* algorithm. The *DSP-A* is responsible for panels no. 5 and 6, the *DSP-E* is responsible for panels no. 1 and 2, and the *DSP-F* is responsible for panels no. 3 and 4. The data of controllers, sensor fault detection and isolation, and switching controllers are saved in the corresponding local memory spaces of the three digital signal processors. The *DSP-A* is the master processor, because it is used to send sensor readings to *DSP-E* and *DSP-F* and also receive command signals from *DSP-E* and *DSP-F*. Furthermore, the *DSP-A* is used to save data of sensor outputs, command signals, and residuals in the external memory disk (*SCSI*).

10.4.2 Experimental results

10.4.2.1 Decentralized direct adaptive control results

In the future mission of a real segmented space telescope system the information from the far region in the space will be collected by the light that is hitting its primary mirror and then reflecting by its secondary mirror to a focal plane in a central panel for information collection. Therefore it is important for the primary mirror to behave as a desired single surface. The deviation of the primary mirror shape from the desired shape is characterized by the edge sensor readings. In the test-bed, 6 shape error Se_i values for the 6 active panels are used to indicate how far the primary mirror is from its desired shape and are defined as:

$$Se_i = \sqrt{\frac{\tilde{y}_i^T \tilde{y}_i}{3}} \qquad i = 1, 2, ..., 6 \tag{10.18}$$

where $\tilde{y}_i$ is the $i-th$ local output vector of the subsystem i after filtering measurement noise. The objective of a control system is to reduce the effect of disturbances on the Se_i values by 100:1 at steady state. To achieve the control objective, 6 local controllers ($DDAOF$ controller) are designed to control the position of the 6-active panels. Fig 10.5 shows the: sensor outputs, control commands, and shape errors for the closed loop system with $DDAOF$ control.

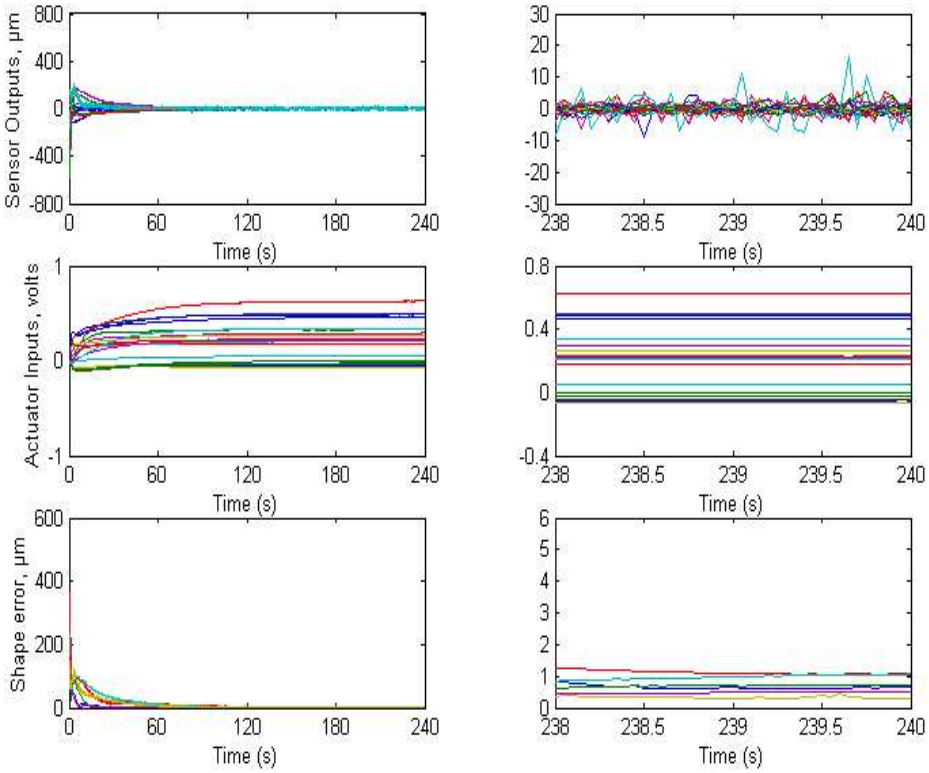

Figure 10.5: Results of the primary mirror system with DDAOF control

The results show that the $DDAOF$ controller can reduce the shape errors by ratio of 100:1. Table 10.1 also demonstrates that by showing the initial shape error values and shape error values at 240 s.

Subsystem no.	Shape error value in μm at 0 s	Shape error value in μm at 240 s
1	107.979	0.66
2	251.199	0.72
3	363.237	1.05
4	233.563	1.07
5	159.361	0.5
6	124.334	0.3

Table 10.1: The shape error values.

10.4.2.2 Decentralized sensor fault detection and isolation(DSFDI) results

An inductive sensor is used to measure a target displacement with respect to a sensor reference plane. Fig 10.6 shows the structure of an inductive sensor (*KDM-8200*).

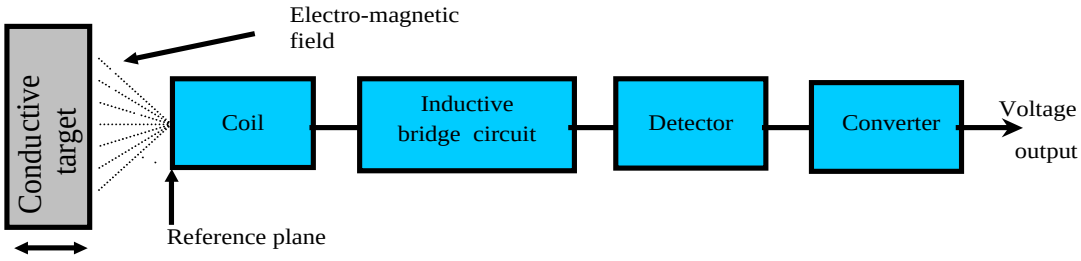

Figure 10.6: The inductive sensor (KDM-8200) structure

The sensor operates as follows: An electromagnetic field propagates out from a sensor coil due to Ac current in the sensor coil. This electromagnetic field will generate an induced current in a conductive target, which will generate another electromagnetic field opposite to the original one. When the target is moving, the intensity of the electromagnetic filed in the coil will change and the result of this changing is a new sensor impedance. A detector senses this new impedance and a converter is used to provide a voltage directly proportional to the target displacement. For the common types of sensor faults that could happen for the inductive sensor *KDM-8200*, Table 10.2 shows the causes and symptoms of commonly inductive sensor faults.

Cause	Symptom
Power supply off	Outage
Incorrect calibration	Drift, degradation, or amplifying actual reading
Open sensor coil	Saturated output at 10 volts
Short circuit	Unchanging output voltage at low voltage
Intermitted cable	Random output signal

Table 10.2: Commonly inductive sensor faults.

To detect and isolate these faults, 3 banks of residual generators are designed based on parity equations method for each of the 6 subsystems. For the best selecting value of the parity equations order m, Fig 10.7 shows the performance index values for the different values of m and for two cases: one for optimal V_{ij} and another for average V_{ij} ,i.e., $V_{ij}^T = \frac{1}{m+1}\begin{bmatrix} 1 & 1 & \cdots & 1 \end{bmatrix}^T$.

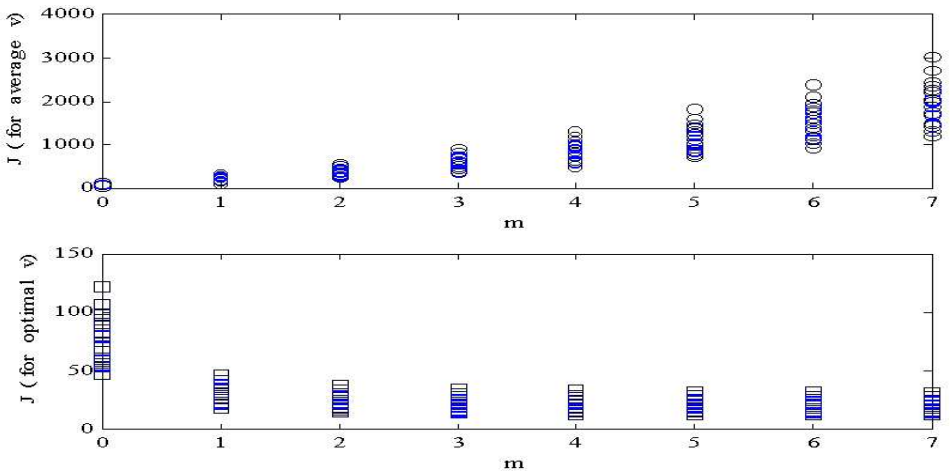

Figure 10.7: The performance index values for different values of m

It is clear from the Fig 10.7 the optimal vector V_{ij} can decrease the performance index value for increasing value of m however, the average V_{ij} will increase the performance index value for increasing value of m. Also, the best value of m is 3 since for $m \geq 3$ the performance index value is little changing. Once the 3 residual signals are generated for each of the 6

subsystems. The different reactions (sensor failure codes) of these residuals are used to find the location of faulty sensor(s) on each subsystem according to the Table 10.3.

Faulty sensor no. / Residuals	No fault	S_{i1}	S_{i2}	S_{i3}	S_{i1}&S_{i2}	S_{i1}&S_{i3}	S_{i2}&S_{i3}	S_{i1}&S_{i2}&S_{i3}
r_{i1}	0	1	0	0	1	1	0	1
r_{i2}	0	0	1	0	1	0	1	1
r_{i3}	0	0	0	1	0	1	1	1
S_{ij}: sensor no. j of subsystem i. 1: the absolute value of the corresponding residual exceeds the threshold value. 0: the absolute value of the corresponding residual dose not exceed the threshold value.								

Table 10.3: Sensor failure codes for subsystem i.

To examine the effectiveness of the $DSFDI$ scheme, the following 6 cases are considered as examples to show how the residuals will behave against:

1. *Sensor fault free*: In this case, all 18 sensors are normally operated.

2. *Sensor fault free with external disturbances*: External disturbances are applied on the primary mirror to see how the 18 residuals will react with existing disturbances.

3. *One sensor is saturated*: We create a saturated fault on one sensor by programming a c^{++}-code to include this type of fault on one selected sensor. The fault takes place at 5 s with a stack value of 10 volts to simulate a real situation when a sensor coil is opened.

4. *One sensor is randomly failed*: The fault takes place at 2 s with different values of sensor output and then stack at 2 volts. With this fault, we tried to emulate a situation when a sensor cable is connected and disconnected in a random way.

5. *The output of one sensor is unchanged with a low voltage*: The fault represents a sensor short circuit. In this case, we consider a fault takes place at 30 s with unchanged sensor output of 2 volts.

6. *With external disturbances, two sensors are failed with a random fault and a low voltage fault*: We add external disturbances on the primary mirror then one sensor is randomly failed at 2 s and another one is failed with unchanged low voltage at 20 s.

Fig 10.8 shows the 18 residual signals for all 6 cases. In these results, all residuals generated by non-faulty sensors have small values comparing to other residuals generated by faulty sensors. Also notice that, all faulty residuals stack (not drift) because we imposed magnitude limits on all actuators inputs to prevent system breakdown when we apply these created faults. Furthermore, these residuals are evaluated to find best threshold values that will prevent false alarms coming from system noise, external disturbances, subsystem interactions, and modeling errors. The same results have been conducted on other sensors, but because of space limitation they are not present here.

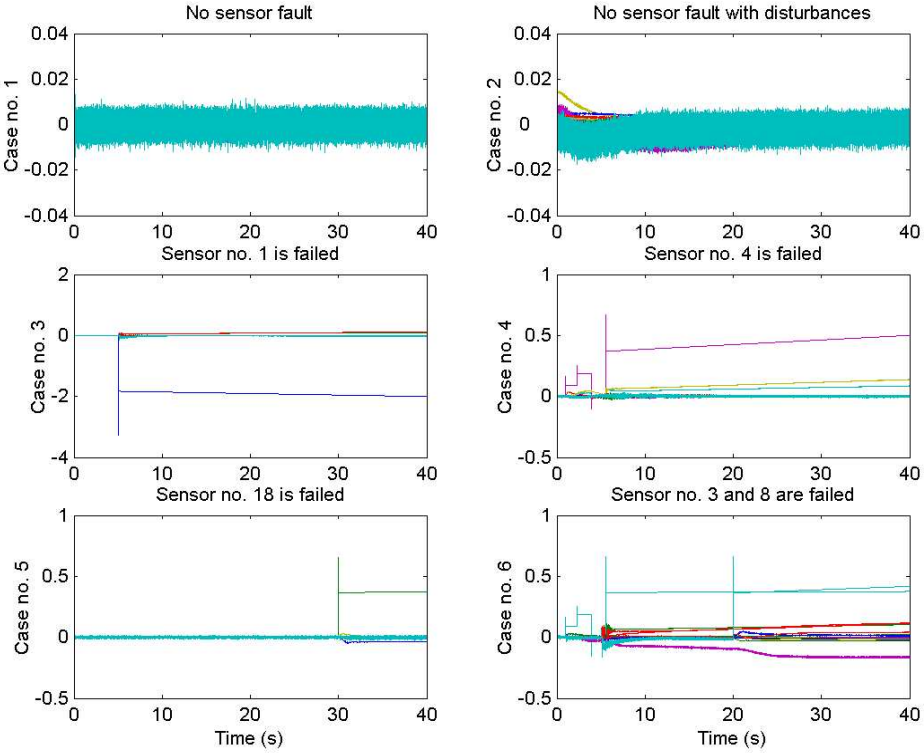

Figure 10.8: The Residual signals for all 6 cases

Table 10.4 shows the fault occurrence time and isolation time for the last 4 cases with thresholds values selected to be 0.3 volt for all 18 residuals.

Case no.	Fault(s) occurrence time (s)	Fault(s) isolation time (s)
3	5	5.001
4	2	5.502
5	30	30.001
6	2 20	5.502 20.001

Table 10.4: Fault occurrence and isolation time.

10.4.2.3 Decentralized reconfiguration control results

Once the sensor fault is detected and isolated by the decentralized sensor fault detection and isolation scheme and the location of the faulty sensor is provided to the supervision system. The local controller effecting by the sensor fault is removed from the service and a switching controller design for that case of faulty sensor is adapted to the service. Four cases are presented here to show the ability of the decentralized reconfiguration control system to tolerate sensor failures, these cases are the last four cases considered for testing the decentralized sensor fault detection and isolation scheme. In Fig 10.9, the sensor no. 1 is failed at 5 s by fixing the sensor output at 10 volts. The results show that with the nominal decentralized control only, a number of actuator inputs are saturated and the shape error for subsystem no. 1 is far away (14400 μ m) from the desired shape error ($\leq 1\mu$ m). However, with the decentralized reconfiguration control system the corresponding local unit of DSFDI quickly detects and isolates this fault and a corresponding switching controller is immediately adapted to the service. All 18 actuator inputs are within the limits and the 6 shape errors are less than 1 μ m at 120 s.

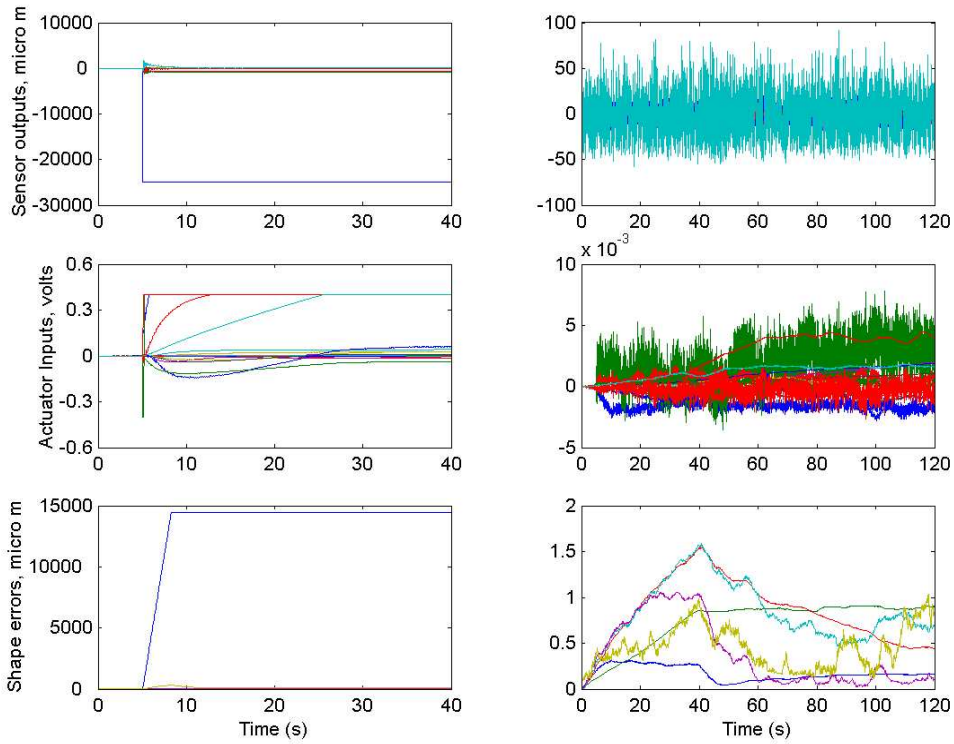

Figure 10.9: Sensor no. 1 is failed (case no. 3): Without DRC (left column); With DRC (right column)

The same conclusions can be made when the sensor no. 18 is failed at 30 s with unchanging output voltage of 2 volts (Fig 10.11). In Fig 10.10, the sensor no. 4 is failed with the random fault at 2 s and the results are: Two actuators inputs belong to the subsystem no. 2 are saturated and all 6 shape errors are larger than 1 μ m (these results are clearly shown in Table 10.5). But with the decentralized reconfiguration control system, the closed loop system performance is much better with expensive of transient at switching time. The same conclusions can be made for the last case (Fig 10.12) where in this case the sensor no. 3 and 8 are failed in the presence of external disturbances at 2 s and 20 s with the random fault and unchanging low voltage volt fault, respectively.

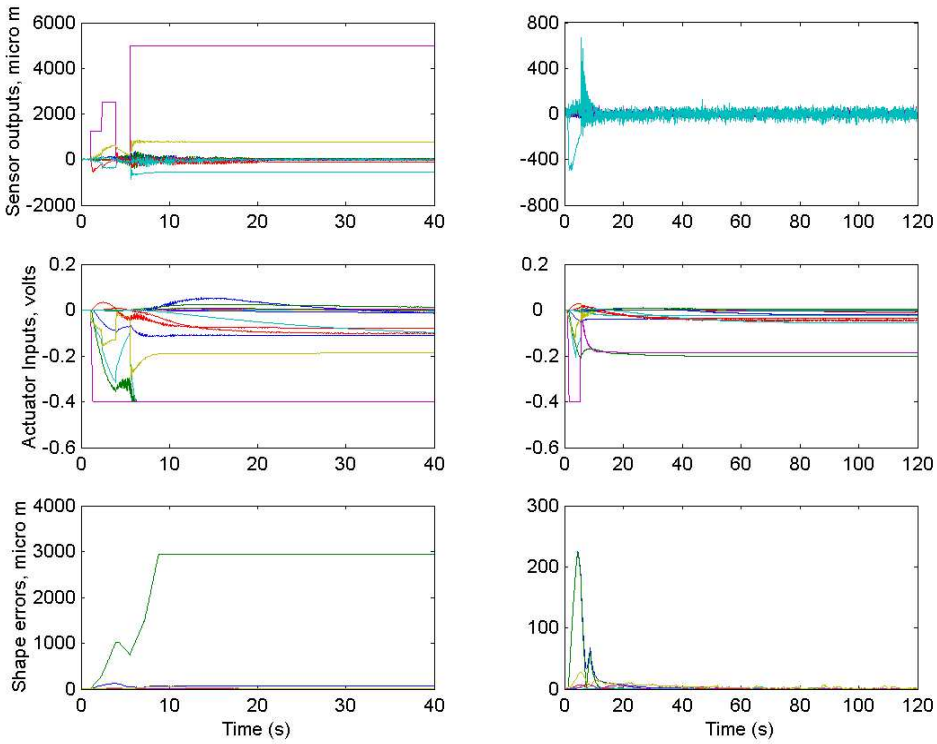

Figure 10.10: Sensor no. 4 is failed (case no. 4): without DRC (left column); with DRC (right column)

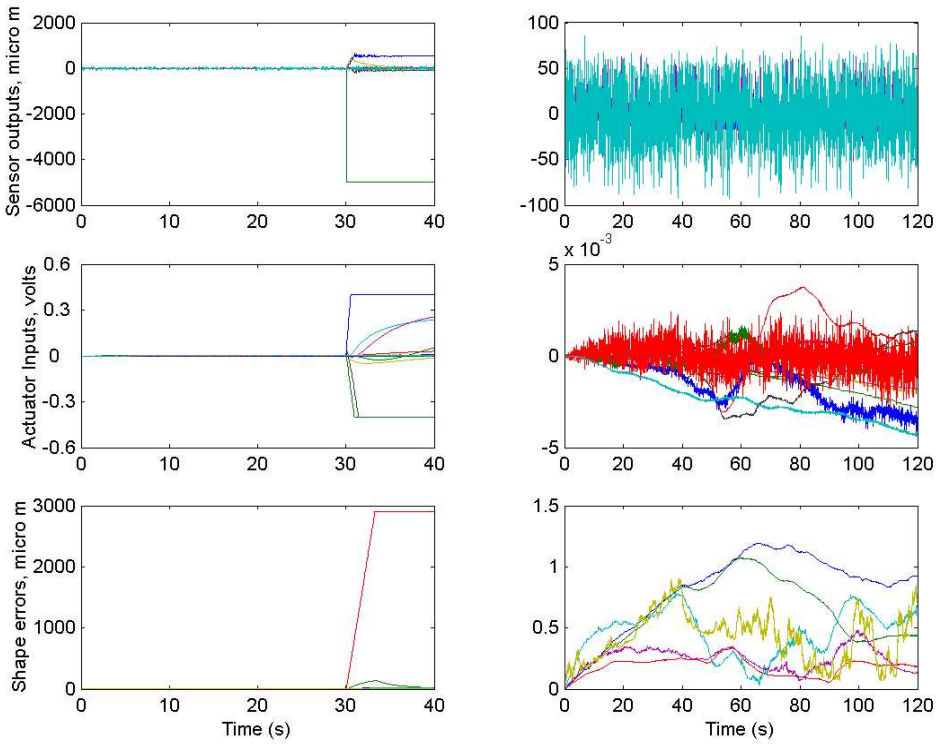

Figure 10.11: Sensor no. 18 is failed (case no. 5): without DRC (left column); with DRC (right column)

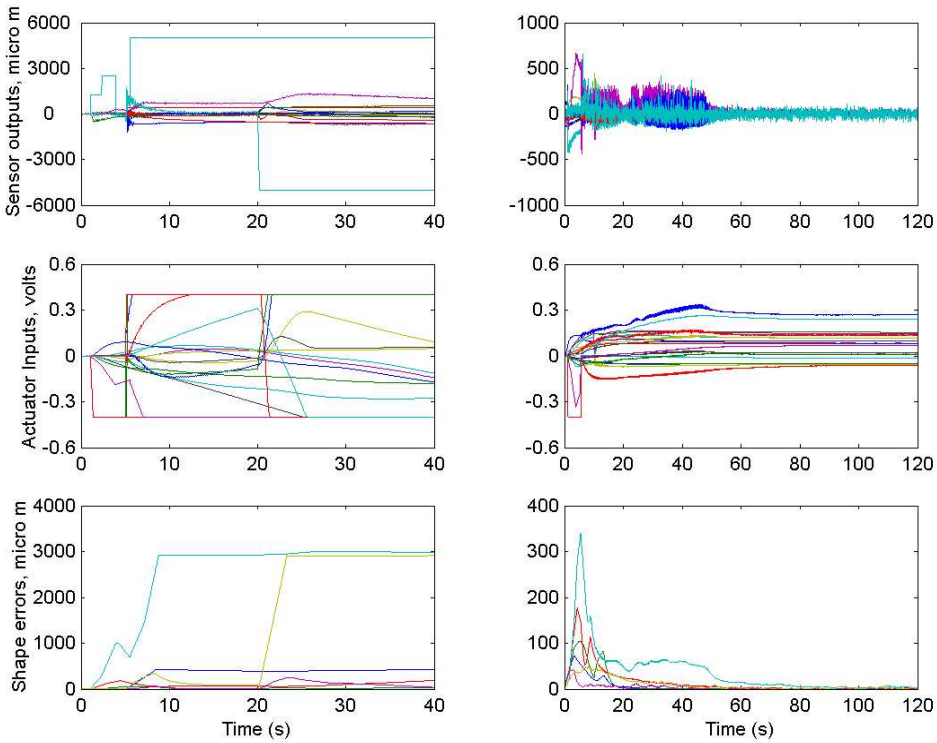

Figure 10.12: Sensor no. 3 and 8 are failed in the presence of external disturbances (case no. 6): without DRC (left column); with DRC (right column)

Table 10.5 shows the steady state shape errors with and without decentralized reconfiguration control system for all 6 subsystems.

Case no.	3		4		5		6	
Subsystem no.	Without DSFTC	With DSFTC	Without DSFTC	With DSFTC	Without DSFTC	With DSFTC	Without DSFTC	With DSFTC
1	14400	0.61	69.12	0.58	26.48	0.88	428.13	0.53
2	0.89	0.89	2930	0.29	20.73	0.41	32.60	0.41
3	2.83	0.44	4.34	0.77	2900	0.04	187.78	0.69
4	12.83	0.78	2.93	1.10	14.68	0.49	2970	0.97
5	0.41	0.06	1.81	0.30	2.84	0.15	37.69	1.10
6	103.57	0.61	8.26	0.40	3.71	0.40	2910	1.40

Table 10.5: The steady state shape errors (μ m).

Reference List

[1] B. D. O. Anderson. An algebraic solution to the spectral factorization problem. *IEEE Transaction on Automatic Control*, pages 410–414, 1967.

[2] B. D. O. Anderson and J. B. Moore. Algebraic structure of generalized positive real matrices. *SIAM J. Contr. Optim.*, (4):615–624, 1968.

[3] M. J. Balas. Modal control of certain flexible dynamic systems. *SIAM J. Contr. Optimiz.*, 16:450–462, 1978.

[4] M. J. Balas. Direct output feedback control of large space structures. *J. Astronautical Sci.*, 27(2):157–180, 1979.

[5] D. S. Bayard. Multivariable frequency domain identification via 2-norm minimization. In *Proc. American Control Conference*, pages 1253–1257, 1992.

[6] D. S. Bayard. An algorithm for state-space frequency domain identification without windowing distortions. *IEEE Trans. on Automatic Control*, (9):1880–1885, 1994.

[7] D. S. Bayard. High order multivariable transfer function curve fitting: algorithms, sparse matrix methods and experimental results. *Automatica*, pages 1439–1444, 1994.

[8] D. S. Bayard and R. Y. Chiang. A frequency domain approach to identification, uncertainty characterization and robust control design. In *Proc. 32nd Conference on Decision and Control*, pages 2266–2271, San Antonio, Texas, 1993.

[9] R. J. Benhabib, R. P. Iwens, and R. L. Jackson. Stability of distributed control for large flexible structures using positivity concepts. *J. Guidance Contr.*, (5):487–494, 1981.

[10] R. J. Benhabib and F. C. Tung. Large space structures control system identification versus direct adaptive control. In *Proc. Joint Automatic Control Conf.*, page 742, San Francisco, CA, 1980.

[11] A. C. Carrier. *Modeling and shape control of a segmented-mirror telescope*. PhD thesis, Stanford University, 1990.

[12] A. C. Carrier and J. N. Aubrun. Modal characterization of the ascie segmented optics test bed: New algorithms and experimental results. In *Proc. 12th IFAC Symp. Automatic Control in Aerospace*, pages xiii+553, 409–415, Germany, 1992.

[13] C. Chen, J. Juang, and G. Lee. Stable state-space system identification from frequency domain data. In *Proc. American Control Conference*, pages 107–111, Baltimore, Maryland, 1994.

[14] R. Y. Chiang and M. G. Safonov. *Robust-Control Toolbox*. Mathworks, South Natick, MA, 1988.

[15] R. A. de Callafon, D. de Roover, and P. M. J. Van Den Hof. Multivariable least squares frequency domain identification using polynomial matrix fraction descriptions. In *Proc. 35th CDC*, pages 2030–2035, Kobe, Japan, 1996.

[16] J. C. Doyle, K. Glover, P. P. Khargonekar, and B. A. Francis. State-space solutions to standard h_2 and h_∞ control problems. *IEEE. Transaction on Automatic Control*, (8):831–847, 1989.

[17] D. Fisher, D. Jue, A. Packard, and K. Poolla. On the identification of high-order lightly-damped multi-variable systems. In *Proc. American Control Conference*, pages 848–853, San Diego, California, 1999.

[18] G. Gu and P. P. Khargonekar. A class of algorithms for identification in h_∞. *Automatica*, pages 299–312, 1992.

[19] N. Gupta. Frequency-shaped cost functionals: extension of linear-quadratic-gaussian design. *J. Guidance Contr.*, (6):529–535, 1980.

[20] C. Harris and J. Miles. Adaptive control of nonlinear flexible spacecraft. In *Proc. IFAC 6th World Conf.*, pages xliv + 692, Boston, MA, 1975.

[21] C. H. Huang, P. A. Ioannou, J. Maroulas, and M. G. Safonov. Design of strictly positive real systems using constant output feedback. *IEEE Transaction on Automatic Control*, pages 569–573, 1999.

[22] P. C. Hughes and R. E. Skelton. Modal truncation for flexible spacecraft. *J. Guidance Contr.*, 4(3):291–297, 1981.

[23] M. Ikeda and D. D. Siljak. Overlapping decentralized control with input, state, and output inclusion. *Control-Theory and advanced technology*, (2):155–172, 1986.

[24] M. Ikeda, D. D. Siljak, and D. E. White. An inclusion principle for dynamic systems. *IEEE. Transaction on Automatic Control*, 29(3):244–249, 1984.

[25] P. A. Ioannou and J. Sun. *Robust Adaptive Control*. Prentice Hall, Inc.

[26] P. A. Ioannou and G. Tao. Frequency domain conditions for strictly positive real functions. *IEEE Transaction on Automatic Control*, pages 53–54, 1987.

[27] W. likins J. R. Sesak and T. Goradetti. Flexible spacecraft control by model error sensitivity suppression. *J. Astronautical Sci.*, (2):131–156, 1979.

[28] M. Jamshidi. *Large-Scale Systems: Modeling and Control*. North-Holland series in system science and engineering, New York, 1973.

[29] T. L. Johnson and J. G. Lin. An aggregation method for active control of large space structures. In *Proc. 18th IEEE Conf. Decision Contr.*, pages 1–3, Fort Lauderdale, FL, 1979.

[30] Ed. L. Meirovitch. In *Proc. AIAA Symp. Dynamics and Contr. of Large Flexible Space Structures*, Blacksburg, VA, 1977.

[31] S. Lefschetz. *Stability of Nonlinear Control Systems.* Academic, 1963.

[32] E. C. Levy. Complex curve fitting. *IRE Trans. on Automatic Control*, pages 37–44, 1959.

[33] K. LI, E. B. Kosmatopoulos, P. Ioannou, and H. R. Boussalis. Large segmented telescopes: centralized, decentralized, and overlapping control design. *IEEE Control System Magzine*, pages 59–72, 2000.

[34] P. L. Lin and Y. C. Wu. Identification of multi-input multi-output linear systems from frequency response data. *Journal of Dynamics Systems, Measurements and Control*, pages 58–64, 1982.

[35] K. Liu, R. N. Jacques, and D. W. Miller. Frequency domain structural identification by observability range space extraction. In *Proc. American Control Conference*, pages 107–111, Baltimore, Maryland, 1994.

[36] L. Ljung. *System identification: theory for the user.* Prentice-Hall, Inc., New Jersey, 1987.

[37] L. Meirovitch and H. Baruch. Control of self-adjoint distributed parameters system. *J. Guidance Contr.*, (1):60–66, 1982.

[38] L. Meirovitch and H. Oz. Modal-space control of large flexible spacecraft possessing ignorable coordinates. *J. Guidance Contr.*, 4(6):569–577, 1980.

[39] R. C. Montgomery and E. G. Abu-Saba. Adaptive and learning control during assembly for large space systems. In *Proc. 18th Conf. Decision and Contr.*, pages 218–219, Fort Lauserdale, FL, 1979.

[40] P. Pintelon, P. Guillaume, Y. Rolain, J. Schoukens, and H. Van hamme. Parametric identification of transfer functions in the frequency domain - a survey. *IEEE Trans. on Automatic Control*, (11):2245–2260, 1994.

[41] M. G. Safonov, R. Y. Chiang, and H. Flashner. h_∞ robust control for a large space. *J. Guidance Contr.*, (3):513–520, 1991.

[42] C. K. Sanathanan and J. Koerner. Transfer function synthesis as a ratio of two complex polynomials. *IEEE Trans. on Automatic Control*, pages 56–58, 1963.

[43] D. D. Siljak. *Decentralized Control of Complex Systems.* Academic Press, New York, 1991.

[44] S. Skogestad and I. Postlethwaite. *Multivariable Feedback Control: Analysis and Design.* John Wiley & Sons, New York, NY, 1996.

[45] S. H. Wang and E. J. Davison. On the stabilization of decentralized control systems. *IEEE. Transaction on Automatic Control*, (5):473–478, 1973.

[46] I. Bar-Kana. Parallel Feed-forward and Simplified Adaptive Control. *Int. J. of Adap. Contr. and Sign. Proc.*, (1):95–109, 1987.

[47] B. Anderson, and J. Moore. *Optimal Control*. Prentice-Hall, New Jersey, 1990.

[48] G. Tao and P. A. Ioannou. Strictly Positive Real Matrices and the Lefscheltz-Kalman-Yakubovich Lemma. *IEEE. Transaction on Automatic Control*, (33):1183–1185, 1988.

[49] P. Gahinet, A. Nemirovski, A. Laub, M. Chilali. *LMI Control Toolbox*. MathWorks, Inc., Mass., 1995.

[50] W. Sun, P. Khargonekar, and D. Shim. Solution to the Positive Real Control Problem for Linear Time-Invariant Systems. *IEEE. Transaction on Automatic Control*, (39), 1994.

[51] H. K. Khalil. *Nonlinear Systems*. Prentice-Hall, Upper Saddle River, NJ, 1996.

[52] G.H. Yang, J.L. Wang, and Y.C. Soh. Reliable LQC control with sensor failures. *IEE Proc. Contr. Theory Appl.*, (147), 2000.

[53] M.H. Shor, W.R. Perkins, and J.V. Medanic. Design of reliable decentralized controllers: A unified continuous/discrete formulation. *Int. J. Control*, (56), 1992.

[54] R.J. Veillette, J.V. Medanic, and W.R. Perkins. Design of reliable control systems. *IEEE. Transaction on Automatic Control*, (37), 1992.

[55] G.H. Yang, J.L. Wang, and Y.C. Soh. Reliable controller design for linear systems with sensor failures. *in Proc. IEEE Conf. Decision and Control*, 1998.

[56] R. Isermann, R. Schwarz, and S. Stolzl. Fault-tolerant drive-by-wire systems. *IEEE control Syst. Mag.*, (22), 2002.

[57] R.F. Stengel. Intelligent failure-tolerant control systems. *IEEE control Syst. Mag.*, (11), 1991.

[58] R.F. Stengel. Toward intelligent flight control. *IEEE Tr. Sys. Man. Cybernetics*, (23), 1993.

[59] H.E. Rauch. Intelligent fault diagnosis and control reconfiguration. *IEEE control Syst. Mag.*, (14), 1994.

[60] H.E. Rauch. Autonomous control reconfiguration. *IEEE control Syst. Mag.*, (15), 1995.

[61] E. Eryurek and B.R. Upadhyaya. Fault-tolerant control and diagnostics for large-scale systems. *IEEE control Syst. Mag.*, (15), 1995.

[62] M. Bodson. Emerging technologies in control engineering. *IEEE control Syst. Mag.*, (15), 1995.

[63] R.J. Patton. Fault-tolerant control systems: The 1997 situation. *in Proc. IFAC Symp. Fault Detection, Supervision and Safety for Technical Processes (SAFEROCESS)*, (2), 1997.

[64] M. Blanke, M. Staroswiecki, and N.E. Wu. Concepts and methods in fault-tolerant control. *in Proc. Amer. Cont. Conf.*, 2001.

[65] R.N. Clark, D.C. Fosth, V.M. Walton. Detection instrument malfunctions in control systems. *IEEE Tr. Aero. Elect. Syst.*, (ASE-11), 1975.

[66] K. Suyama. Reliable observer-based control using vector-valued decision by majority. *in Proc. IEEE Conf. Decision and Control*, 1999.

[67] G. Bajpai, B.C. Chang, and A. Lau. Control laws with hierarchical switch logic to accommodate eme-induced sensor failures. *in Proc. Digita. Avionics Syst. Confr.*, 1999.

[68] M.R. Napolitano, D.A. Windon, II, J.L. Casanova, M. Innocenti, and G. Silvestri. Kalman filters and neural-network schemes for sensor validation in flight control systems. *IEEE Tr. Contr. Sys. Tech.*, (6), 1998.

[69] D. Capriglinoe, C. Liguori, C. Pianese, and A. Pietrosanto. On-line sensor fault detection, isolation, and accommodation in automotive engines. *IEEE Instr. Measur. Tech. Conf.*, 2002.

[70] S. Wang, Y. Chen. Fault-tolerant control for outdoor ventilation air flow rate in building based on neural network. *Building and Environment*, (37), 2002.

[71] H. Noura, D. Sauter, F. Hamelin, and D. Theilliol. Fault-tolerant control in dynamic systems: application to a winding machine. *IEEE control Syst. Mag.*,(20), 2000.

[72] A.S. Willsky. A survey of design methods for failure detection in dynamics systems. *Automatica*,(12), 1976.

[73] R.N. Clark. Instrument fault detection. *IEEE Trans. Aero. Electron. Syst.*, (14), 1978.

[74] P. M. Frank. Advanced fault detection and isolation schemes using nonlinear and robust observers. *10th IFAC Congress*,(3), 1987.

[75] J. Gertler. Analytical redundancy methods in fault detection and isolation. *IFACSAFE-PROCESS Symposium*, (1), 1991.

[76] M.A. Massoumnia and W.E. Velde. Generating parity relations for detecting and identifying control system component failures. *J. Guidance*,(11), 1988.

[77] J. Gertler. Generating directional residuals with dynamic parity equations. *Automatica*,(31), 1995.

[78] R. Isermann. Process fault detection based on modeling and estimation methods- a survey. *Automatica*, (20), 1984.

[79] T. Sorsa, H. N. Koivo, and H. Koivisto. Neural network in process fault diagnosis. *IEEE Tr. Sys. Man. Cybernetics*,(21), 1991.

[80] A. Bernieri, M. DApuzzo, L. Sansone, and M. Savastano. A neural network approach for identification and fault diagnosis on dynamic systems. *IEEE Trans. Instrum. Measur.*, (43), 1994.

[81] B.K. Seliger and P.M. Frank. Fault detection and isolation in technical processes with neural networks. *in Proc. IEEE Conf. Decision and Control*, 1995.

[82] R.J. Patton, J. Chen, and T.M. Siew. Fault diagnosis in nonlinear dynamic systems via neural networks. *in Proc. Inter. Nation. Confer. on Contr.*,1994.

[83] R. Isermann. Supervision, fault-detection and fault-diagnosis methods C an introduction. *Contr. Eng. Practice*, (5), 1997.

[84] G. Betta and A. Pietrosanto. Instrument fault detection and isolation: state of the art and new research trends. *IEEE Trans. Instrum. Measur.*,(49), 2000.

[85] M. Sadrnia, J. Chen and R. Patton. Robust observer-based residual generation for fault diagnosis. *Proc. IFACSAFEPROCESS97*, 1997.

[86] R.J. Patton and J. Chen. Robust fault detection using eigenstructure assignment: A tutorial consideration and some new results. *in Proc. IEEE Conf. Decision and Control*, 1991.

[87] G.R. Duan, R.J. Patton. Robust fault detection in linear systems using luenberger observers. *in Proc. Inter. Nation. Confer. on Contr.*,1998.

[88] E.Y. Chow and A.S. Willsky. Analytical redundancy and the design of robust failure detection systems. *IEEE Trans. Automat. Cont.*, (AC-29), 1984.

[89] X. Lou, A. Willsky, G. Verghese. Optimal robust redundancy relations for failure detection in uncertain system. *Automatica*,(22), 1986.

[90] X. Ding, L. Guo and T. Jeinsch. A characterization of parity space and its application to robust fault detection. *IEEE Trans. Automat. Cont.*,(44), 1999.

[91] X. Ding, L. Guo, and P.M. Frank. A frequency domain approach to fault detection of uncertain dynamic systems. *in Proc. IEEE Conf. Decision and Control*, 1993.

[92] P.M. Frank and X. Ding. Frequency domain approach to optimally robust residual generation and evaluation for model-based fault diagnosis. *Automatica*, (30), 1994.

[93] Z. Qiu and J. Gertler. Robust FDI systems and optimization. Disturbances ant tall fault case. *in Proc. IEEE Conf. Decision and Control*,1993.

[94] P.M. Frank. Fault diagnosis in dynamic systems using analytical and knowledge-based redundancy- A survey and some new results *Automatica*,(26), 1990.

[95] J. Chen and R.J. Patton. *Robust Model-Based Fault Diagnosis for Dynamic Systems*. Prentice-Hall, Kluwer, Bosten, MA, 1999.